

Density Functional Theory Study of Complex Metal Oxide Surface Reconstructions

DISSERTATION

zur Erlangung des akademischen Grades

Doktor der Naturwissenschaften

eingereicht von

Eamon John Gordon McDermott, M.Sc., B.A.Sc.

Matrikelnummer 1228575

Anschrift Kleine Stadtgutgasse 4 / Top 4, 1020 Wien

an der Fakultät für Technische Chemie der Technischen Universität Wien

Betreuung: Ao.Univ.Prof. Dipl.-Ing. Dr.techn. Peter Blaha, E165 - Institut für Materialchemie

Diese Dissertation haben begutachtet:

Peter Blaha

Josef Redinger

Wien, 20. Mai 2016

Eamon John Gordon
McDermott



TECHNISCHE
UNIVERSITÄT
WIEN

Density Functional Theory Study of Complex Metal Oxide Surface Reconstructions

DISSERTATION

submitted in partial fulfillment of the requirements for the degree of

Doktor der Naturwissenschaften

by

Eamon John Gordon McDermott, M.Sc., B.A.Sc.

Registration Number 1228575

Address Kleine Stadtgutgasse 4 / Top 4, 1020 Wien

to the Faculty of Technical Chemistry at the Vienna University of Technology

Advisor: Ao.Univ.Prof. Dipl.-Ing. Dr.techn. Peter Blaha, E165 - Institut für Materialchemie

The dissertation has been reviewed by:

Peter Blaha

Josef Redinger

Vienna, 20th May, 2016

Eamon John Gordon
McDermott

Erklärung zur Verfassung der Arbeit

Eamon John Gordon McDermott, M.Sc., B.A.Sc.
Kleine Stadtgutgasse 4 / Top 4, 1020 Wien

Hiermit erkläre ich, dass ich diese Arbeit selbständig verfasst habe, dass ich die verwendeten Quellen und Hilfsmittel vollständig angegeben habe und dass ich die Stellen der Arbeit – einschließlich Tabellen, Karten und Abbildungen –, die anderen Werken oder dem Internet im Wortlaut oder dem Sinn nach entnommen sind, auf jeden Fall unter Angabe der Quelle als Entlehnung kenntlich gemacht habe.

Wien, 20. Mai 2016

Eamon John Gordon
McDermott

Kurzfassung

Jedes Material ist durch seine Oberfläche nach außen hin begrenzt und mittels dieser Oberfläche kann das Material mit der Umgebung physikalisch und chemisch wechselwirken. Viele interessante Eigenschaften eines funktionellen Materials sind durch seine Oberfläche bestimmt und daher muss die Oberfläche genau verstanden werden um deren spezifischen Eigenschaften verstehen und verwenden zu können. Metalloxide werden immer wichtige Materialien im Einsatz als Katalysatoren oder in der Elektronikindustrie. In dieser Dissertation werden die Oberflächenrekonstruktionen von zwei komplexen Metalloxiden mittels einer Kombination von experimentellen und theoretischen Methoden untersucht, wobei die theoretischen Untersuchungen auf Dichtefunktionaltheorie basieren und mit dem Wien2k Programm durchgeführt wurden.

Beim ersten System handelt es sich um die (001) Oberfläche von Magnetit, die eine $(\sqrt{2} \times \sqrt{2})R45^\circ$ Rekonstruktion aufweist. Diese Oberfläche kann einzelne adsorbierte Metallatome stabilisieren, was sie für zu einem interessanten Modellkatalysator macht. Der Mechanismus, wie und warum die adsorbierten Atome gerade selektive auf bestimmten Positionen landen, war bisher nicht verstanden. Eine Kombination von STM und LEED IV Messungen und deren Interpretation mittels DFT Rechnungen, führte zu einem neuen Strukturmodell dieser Oberfläche, das durch eine geordnete Anordnung von Kation-Lehrstellen in einer Schicht unterhalb der Oberfläche (subsurface cation vacancies, SCV) stabilisiert wird. Die theoretisch optimierte SCV Struktur stimmt ausgezeichnet mit der experimentell ermittelten Struktur überein.

Beim zweiten System handelt es sich um zwei verschiedene Rekonstruktionen der Strontiumtitanat (110) Oberfläche. Diese Oberfläche zeigt verschiedenste Rekonstruktionen, die von den Herstellungsbedingungen abhängen. Die zwei Rekonstruktionen wurden mittels XANES experimentell untersucht und die Spektren konnten durch Kristallfeld-Multiplett und DFT Berechnungen interpretiert werden. Das besondere Augenmerk lag dabei auf der ungewöhnlichen tetraedrischen Koordination von Ti, die bei der (4×1) Oberflächenrekonstruktion auftritt.

Abstract

The surface of a material is its connection to the outside world, and it is through the surface that a material can interact physically and chemically with its environment. Many of the interesting properties of functional materials are controlled by their surface structure and chemistry, requiring a careful understanding of the surface to understand and apply them. In particular, metal oxides are becoming increasingly important in applications such as catalysis and novel electronics. In this dissertation, the surface reconstruction of two complex metal oxide surfaces are investigated using a combination of experimental and theoretical methods, in particular density functional theory calculations performed with the WIEN2k code.

The first system studied is the magnetite (001) surface, which undergoes a $(\sqrt{2}\times\sqrt{2})R45^\circ$ surface reconstruction that is capable of stabilizing single metal adatoms, making it an interesting model catalytic support. The mechanism by which adatoms selectively adsorb on this surface was not previously understood. Using a combination of STM and LEED IV experiments interpreted with DFT calculations, we have proposed a new structural model of this surface, which is stabilized by an ordered array of subsurface cation vacancies (SCV). This SCV structure achieves an excellent agreement with experiment, on par with well-understood metal reconstructions.

The second system involved the study of two reconstructions of the strontium titanate (110) surface. This surface undergoes a wide variety of reconstructions depending on preparation conditions. Two reconstructions were investigated using XANES, crystal field multiplet and DFT calculations, with emphasis on the unusual tetrahedral coordination of Ti on the 4×1 surface reconstruction.

Acknowledgements

The time spent preparing this dissertation has been a particularly challenging time in my life, and has only been possible with support from many people around me. Foremost I would like to graciously acknowledge the support, guidance and good nature of my supervisor, Prof. Dr. Peter Blaha, for taking me on as a student, helping me bridge the gap between theorist and experimentalist, and for providing support far outside the scope of academics. I also acknowledge Prof. Dr. Ulrike Diebold for giving me access to her world of exciting projects as my co-supervisor. I enjoyed many productive discussions with the members of the Computational Quantum Chemistry research group, my colleagues in the Solids4Fun doctoral school and my many collaborators, particularly Roland Bliem and Dr. Gareth Parkinson, who both work much harder than I.

Secondly, I owe a great debt of gratitude to the many doctors, nurses and other staff of the Klinische Abteilung für Hämatologie und Hämostaseologie at the Allgemeines Krankenhaus der Stadt Wien, without whose excellent treatment and care the completion of this work would not have been possible. The cool, calm demeanour of Univ.-Prof. Dr. Ulrich Jäger and Univ.-Prof. Dr. Wolfgang R. Sperr, along with the follow-up care of Dr. Cathrin Skrabs allowed me to always maintain my composure and to look forward to the time when working on this dissertation could once again be my main concern in life.

I humbly acknowledge the support of the state of Austria for allowing me to live and work within its borders, and the financial support of the Austrian Science Fund (FWF) under project W1243 (Solids4Fun). I additionally acknowledge compute facilities provided by the Vienna Scientific Cluster as well as the MAX-lab synchrotron facility in Lund, Sweden. I have been very lucky to have had this opportunity to pursue my education without being restricted by borders, nationality or my mother tongue.

I have also relied a great deal on support from the many friends I have made since moving to Austria for my studies. Without their willingness to welcome a crazy Canadian into their lives my experience living here would have been greatly diminished, which would have without doubt impacted the quality of this work.

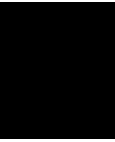
Finally I acknowledge the support and understanding of my family, who accepted and celebrated my decision to move even further from rural Muskoka in pursuing my academic goals. I was happy to be able to share some small part of this adventure with my parents, and am grateful for the sacrifices they both made so that my mother could stay with me during my health challenges.

Contents

Kurzfassung	vii
Abstract	ix
Contents	xiii
1 Introduction	1
1.1 Organization	2
2 Density Functional Theory	3
2.1 Ab-initio basis of DFT	3
2.2 Kohn-Sham theory	4
2.3 Exchange-Correlation Functionals	5
2.4 WIEN2k	10
3 Surfaces and Surface Reconstruction	17
3.1 Surface Phase Diagrams	20
4 Experimental Methods of Studying Surfaces	23
4.1 Scanning Tunneling Microscopy	23
4.2 X-ray Spectroscopy	26
4.3 Low Energy Electron Diffraction (LEED)	34
5 The Subsurface Cation Vacancy Surface Reconstruction of Magnetite	39
5.1 Introduction	39
5.2 Previous Understanding of the (001) Surface	40
5.3 Adatoms on the (100) surface	43
5.4 SCV termination	45
5.5 Theoretical Techniques	46
5.6 Experimental Techniques	52
5.7 Consequences of the SCV Surface Reconstruction	54
5.8 Conductivity of the SCV Surface	58
6 Surface Reconstructions of Strontium Titanate (110)	61

xiii

6.1	Introduction	61
6.2	Experimental Considerations	63
6.3	Calculated Ti $L_{2,3}$ XANES	64
6.4	Calculated O K XANES	67
6.5	Experimental Results and Discussion	69
6.6	Calculated DOS	72
6.7	Stoichiometry Change at the STO (110) Surface	73
7	Conclusions	79
7.1	Magnetite (001)	79
7.2	Strontium Titanate (110)	80
7.3	Contributions to Publications	82
A	STO 2×4 Surface Reconstruction	83
B	Core Hole Sites for STO Calculations	85
	List of Figures	87
	List of Tables	92
	List of Algorithms	92
	Bibliography	93



Introduction

It has become increasingly important in the world today to acquire a good understanding of the surfaces of materials. Many physical processes of contemporary interest occur at the surfaces of materials or interfaces between them, such as novel interface superconductivity, catalytic and chemical reactions, the adsorption of solar energy and many more. As the application of material surfaces has become more relevant, it has become important to develop new techniques to better understand the outer extent of bulk materials.

With the explosion in experimental techniques available to study material surfaces, such as STM, AFM, LEED, SXRD and more, it is important for theoreticians to support and interpret the data collected by experimentalists. While experimentalists are often able to work quickly to study many materials under a wide variety of conditions and preparations, gaining an empirical understanding of a material of inquiry, it is sometimes only through a return to our theoretical understanding of a material that we can resolve science's most complex and unintuitive questions. It therefore often falls to the theorist, who's techniques are typically slower, to elucidate the origin of a material's most interesting properties.

This work examines the intersection of various experimental methods with one of the most widely used theoretical techniques in materials science: the Density Functional Theory (DFT) as implemented in the WIEN2k code. DFT has become a workhorse in the scientific community, having been implemented in dozens of codes that reliably produce repeatable results, leading to over 15,000 publications each year[1, 2]. With ever increasing computer power and code sophistication, it becomes possible for researchers to expand their field of study into increasingly complex situations. The great hope is that such understanding gained from theoretical methods can find applicability to our knowledge of the real, physical world.

1.1 Organization

This dissertation can be separated generally into three parts. First, a background of the theoretical and experimental techniques used in this work are developed, including the essentials of Density Functional Theory (Chapter 2), some basic theory of crystalline surfaces and their reconstruction (Chapter 3) as well as an overview of the experimental techniques used to study them in this work (Chapter 4). These chapters rely primarily on the literature, with a small amount of experience from using X-ray spectroscopy techniques.

The remainder of the work uses the developed background to introduce and investigate two complex metal oxide surfaces. The second part (Chapter 5) introduces magnetite (Fe_3O_4), its (001) surface and a novel reconstruction that is stabilized by subsurface cation vacancies (SCV). The SCV surface is studied using STM and LEED IV measurements and simulated using the WIEN2k code.

The third part (Chapter 6) introduces strontium titanate (SrTiO_3), its (110) surface and several of its surface reconstructions, which are investigated using XPS and XANES.

Density Functional Theory

2.1 Ab-initio basis of DFT

We can describe a material quantum mechanically by capturing the dynamics of its constituent components. For condensed matter under typical conditions this can be achieved using a time-independent Schrödinger equation[3] to describe electrons interacting with a fixed potential $V(\vec{R})$:

$$\left(-\frac{1}{2} \sum_{i=1}^N \nabla^2_{\vec{r}_i} + \frac{1}{2} \sum_{i \neq j} \frac{1}{|\vec{r}_i - \vec{r}_j|} - \sum_i V(\vec{r}_i) \right) \Psi_{total} = E \Psi_{total} \quad (2.1)$$

where \vec{r}_i represents the position and spin coordinates of electron i , and Ψ_{total} the wave function of the entire system, which has an energy E . The Hamiltonian of this system contains each electron's kinetic energy, the Coulomb repulsion between electrons (Hartree term) and the interaction of each electron with a fixed potential $V(\vec{r})$, which is applied to each electron by the set of atomic nuclei:

$$V(\vec{r}) = \sum_i \frac{Z_a}{|\vec{R}_i - \vec{r}|} \quad (2.2)$$

where Z_a is the charge of nucleus a .

The implicit assumption in using this expression is that nuclei are fixed in their equilibrium positions; this is known as the *Born-Oppenheimer* approximation[4]. This approximation is reasonable when studying only the *electronic* properties of a system. Since the electron mass is so much less than any nuclear mass (m_e is approximately 1/2000th the mass of a proton) the electron dynamics can be effectively separated from the nuclear dynamic, such that:

$$\Psi_{total} = \Psi_{electronic} \times \Psi_{nuclear} \quad (2.3)$$

Utilizing Born-Oppenheimer to separate out the electronic wave-function restricts the Hilbert space of the problem, greatly reducing the computational effort required to find solutions. While not exact, the solutions remain relevant for material problems that do not strongly depend on nuclear movement (e.g. low-temperature simulation of stable solids) and in which a steady state electronic solution is desired (e.g. when searching for a material's ground state).

Unfortunately even Equation 2.1 is impossible to solve exactly in all but the simplest systems, such as the hydrogenic ions with only a single electron. Since each electron has 3 spatial coordinates and a spin degree of freedom, this approach creates a problem with $4N$ coupled coordinates of the form of Equation 2.4 and quickly becomes intractable with increasing particle count. Further simplifications are necessary to approach the problem in a practical way.

$$\Psi_{total} = f(\vec{r}_1, \vec{r}_2, \dots, \vec{r}_N, s_1, s_2, \dots, s_N) \quad (2.4)$$

2.2 Kohn-Sham theory

To make solutions to the Schrödinger equation tractable, one strategy is to further separate $\Psi_{electronic}$ into wave functions representing individual, non-interacting pseudo-particles that otherwise behave like electrons. One schema proposed by Hohenberg and Kohn was to instead consider a mean-field problem in which pseudo-electrons interact with the density of all electrons in the system; modelling the electrons as an inhomogeneous electron gas[5]. The Schrödinger equation is therefore replaced with an equation of state of the form:

$$\left(-\nabla_i^2 + V_{\text{eff}}(\vec{r})\right) \phi_i(\vec{r}) = \epsilon_i \phi_i(\vec{r}) \quad (2.5)$$

$$\rho(\vec{r}) = \sum_i^N |\phi_i(\vec{r})|^2 \quad (2.6)$$

where V_{eff} is now an effective Kohn-Sham potential[6] and the set of ϕ_i are now pseudo-particle wave functions with energy ϵ_i . The total wave function of the system is now a Slater determinant of the "single electron" wave functions ϕ_i , in order that they remain fermions and obey antisymmetry under exchange.

This formulation is useful as Kohn and Sham demonstrated the existence of a *unique* ground state density $\rho(\vec{r})$ for each V_{eff} . This implies that is possible to use the variational principle to arrive at a single set of ϕ_i that satisfy Equation 2.5, effectively reducing the

many-body problem in $3N$ coordinates to a optimization in 3 spatial coordinates ($4N$ reducing to 4 if spin is included). This density then contains all information about the model system's state.

This scheme of reducing a many body system to a single-electron picture results in the total energy of the system being expressed as a *functional* of its charge density (hence Density Functional theory) with the form:

$$E(\rho) = T_s(\rho) + \int d\vec{r} V_{\text{eff}}(\vec{r})\rho(\vec{r}) + E_{xc}(\rho) \quad (2.7)$$

where T_s is the kinetic energy of the non-interacting e^- , E_c is the Coulomb energy between the single electrons and E_{xc} is an exchange-correlation energy, which contains the many-body effects that are separable in the Kohn-Sham picture. Therefore, in principle DFT allows for the calculation of total energy from exact kinetic and potential energies of pseudoparticles in a material, which must then be corrected by an exchange-correlation energy of unknown form.

2.3 Exchange-Correlation Functionals

2.3.1 Local (Spin) Density Approximation

In order for the Kohn-Sham method above to be useful, we require an approximation for the exchange-correlation (XC) energy. Ideally we want this quantity to be inexpensive to compute, despite the fact that it contains the most intractable interactions within the solid. As an initial guess, it can be assumed that the XC energy for a given volume of space is a function of the electron density held within it; the so-called *Local Density Approximation* (LDA). In the infinitesimal limit, this is equivalent to dividing space into small homogeneous pieces and summing the contribution of each, giving an E_{xc} of the form:

$$E_{xc}^{LDA} = \int \rho(\vec{r})\epsilon_{xc}(\rho)d\vec{r} \quad (2.8)$$

This formulation will hold true in the case of a spatially homogeneous electron gas, but also turns out to work reasonably well in the case of realistic materials with slowly-varying charge distributions, where most electrons occupy reasonably smooth s and p-type orbitals. In orbitals with higher quantum numbers ℓ this approximation breaks down, as will be discussed below.

In LDA, the XC energy is simply a sum of non-interacting exchange and correlation energies (i.e. $E_{xc}^{LDA} = E_x^{LDA} + E_c^{LDA}$). In the case of a homogeneous electron gas, this exchange energy is known as derived from Hartree-Fock theory[7]:

$$E_x^{LDA}[\rho] = -\frac{3}{4} \left(\frac{3}{\pi}\right)^{1/3} \int \rho(\vec{r})^{4/3} d\vec{r} \quad (2.9)$$

However, the correlation energy of the homogeneous electron gas E_c^{LDA} cannot be expressed analytically. Instead it is necessary to use quantum Monte-Carlo methods at various densities, then interpolate the results[8]. Regardless, results for the homogeneous electron gas are well understood and can be reproduced within higher order methods such as the random-phase approximation (RPA), so this method remains ab-initio[9].

In the case of spin-polarized systems, it is necessary to consider the contribution of the two spin channels ρ_\downarrow and ρ_\uparrow to the XC energy, as they will not necessarily have the same occupation due to spin splitting. In the *Local Spin-Density Approximation* (LSDA), the exchange energy is still known exactly[10][11]:

$$E_x^{LDA}(\rho_\downarrow, \rho_\uparrow) = \frac{1}{2} \left(E_x^{LDA}(2\rho_\downarrow) + E_x^{LDA}(2\rho_\uparrow) \right) \quad (2.10)$$

while the correlation energy becomes a function of the relative polarization at each point, and must similarly be solved numerically.

While the LDA is a simple approximation of the complexities of many-body physics, it produces many reasonable results. For example, in a test of 60 solids, LDA was found to reproduce their experimental lattice constants with a mean relative error of -1.37%[12]. LDA tends to over-bind atoms, leading to generally lower lattice constants and overestimating binding energies. While electronic structure calculated with LDA can be compared to experimental measurements, the spacing between bands is not accurate with the band gap in particular being underestimated.

2.3.2 Generalized Gradient Approximation

Up until this point, DFT can still be considered a fully *ab initio* method, as the approximations involved in LDA still yield reasonable results without resorting to fits to experimental results. Of course, real materials do not consist of homogeneous electron gases, and it therefore makes sense that the exchange-correlation energy should consider more complex densities. The simplest way to expand the density functional to consider spatial inhomogeneities is to use a Taylor expansion spatially about the local point, i.e. to include gradient terms, as is the case in the *Generalized Gradient Approximation* (GGA):

$$E_{xc}^{GGA}(\rho_\uparrow, \rho_\downarrow) = \int d\vec{r} f(\rho_\uparrow, \rho_\downarrow, \nabla\rho_\uparrow, \nabla\rho_\downarrow) \quad (2.11)$$

At this point the form of the functional has become too complex, and there is no longer a single method for parametrizing this functional. It therefore becomes necessary to choose GGAs that allow one to reproduce a desired experimental result (e.g. atomization energies of molecules or unit cell parameters of solids), or that include empirical coefficients in their analytical forms. Using GGA it becomes more complicated as to whether DFT is still an *ab initio* method. The method of constructing a GGA can be performed in such a way as to reproduce behaviour as postulated in the axioms of DFT, such as the

ability of a functional to correctly treat homogeneous electron gasses. A GGA can also be parametrized, and parameters chosen to describe certain systems of interest in a clearly empirical fashion. Regardless, extending functionals beyond the strictly local makes them more accurate and more applicable to a wide variety of systems and problems.

The most popular GGA is the one proposed by Perdew, Burke and Ernzerhof (PBE)[13]. PBE has enjoyed considerable success in materials calculations, in part due to its parametrization focusing on reproducing expected universal behaviour in the limiting cases of infinite charge density and the homogeneous electron gas. The performance of the PBE functional compares well across a large variety of materials, producing low errors when optimizing lattice constants of $3d$ elements and when calculating atomization energy[12], and improves the over-binding of atom as compared to LDA.

In this work the PBE functional is primarily used. However, choices made in PBE's parametrization that improve free-atom-like properties (e.g. total atomization energies) simultaneously degrade its accuracy when modelling slowly varying densities found in solids. Another functional, PBEsol, slightly modifies PBE by instead choosing two expansion coefficients (μ and β) in order to improve exchange and correlation energies within solids, improving lattice constants[14]. PBEsol is used in Section 6 for reasons explained within. A comparison of the behaviour of PBE and PBEsol is shown in Figure 2.1, which plots their exchange correlation enhancement factors $F_{XC}(r_s, s)$ versus reduced density gradient $s = |\nabla\rho|[2(3\pi^2)^{1/3}\rho^{4/3}]^{-1}$ for typical atomic distances. The enhancement factor is then related to the exchange correlation energy by[13]:

$$E_{xc}^{GGA}(\rho_{\uparrow}, \rho_{\downarrow}) = \int d\vec{r} n(\vec{r}) \epsilon_X^{unif}(n(\vec{r})) F_{XC}(r_s, \zeta, s) \quad (2.12)$$

where n is the number of electrons ($n_{\uparrow} + n_{\downarrow}$), $\epsilon_X^{unif}(n)$ is the correlation energy per particle of the homogeneous electron gas (i.e. $\rho(\vec{r})^{4/3}$ from LDA), r_s is the local Seitz radius ($n = \frac{3}{4}\pi r_s^3$) and ζ is the relative spin polarization $(n_{\uparrow} - n_{\downarrow})/n$.

2.3.3 Hubbard correction for correlated materials (LDA+U)

While LSDA performs reasonably well for smoothly varying orbitals (such as for s and p orbitals), it runs into problems correctly describing the ground state of systems with open $3d$ or $4f$ shells, such as magnetic insulators. Failures include low calculated moments and predictions of metallic conduction in Mott insulators. In general, the poor description of strong correlation effects in these sharply varying orbitals cause an underestimation of the spin splitting in these systems.

The conductivity of these correlated materials can be understood in terms of the Hubbard model. In this model, the behaviour of particles on a lattice is modelled through two interactions: a kinetic energy term allowing particles to hop between lattice sites (traditionally called t), and a potential term describing the energy of doubly occupying a site (called U). The Hubbard Hamiltonian for fermions thus takes the form:

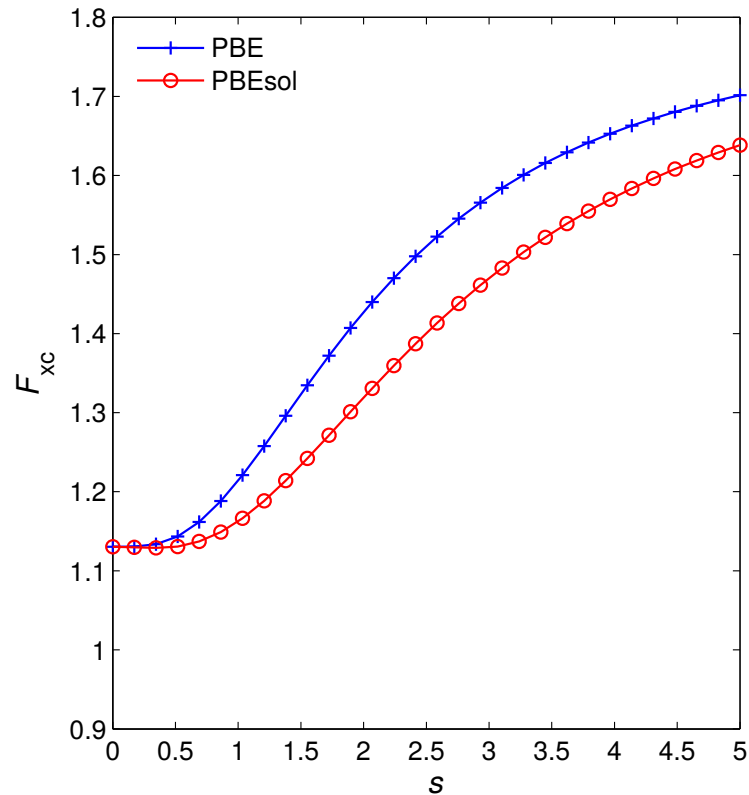


Figure 2.1: Exchange correlation enhancement factor $F_{xc}(r_s, s)$ versus reduced density gradient of the PBE and PBEsol functionals. The above plot is made for Wigner-Seitz radius $r_s = 1$ bohr. Courtesy of Dr. Fabien Tran

$$H = -t \sum_{\langle i,j \rangle} (c_i^\dagger c_j + c_j^\dagger c_i) + U \sum_{i=1}^N n_{i\uparrow} n_{i\downarrow} \quad (2.13)$$

where $\langle i, j \rangle$ sums over nearest neighbouring lattice sites (in the simplest form of the model), c_i and c_i^\dagger are creation and annihilation operators for site i , respectively, and $n_{i,\alpha}$ is the occupation operator for particles on site i with spin α . For the purposes of LSDA, the interesting physics is that there is an energy cost U associated with placing two particles on a single site. For example, the effect of a Hubbard U on a Mott insulator is depicted in Figure 2.2.

It was therefore proposed to improve the LSDA by applying an orbital potential U (LDA+ U) to simulate the effects of a multiband Hubbard model[15], the results of which has been shown to work well in describing the physics of half d -band filling. Practically speaking, a potential U is applied to a single set of highly correlated states, such as valence $3d$ or $4f$. While the magnitude of U can be estimated from first principles[16][17],

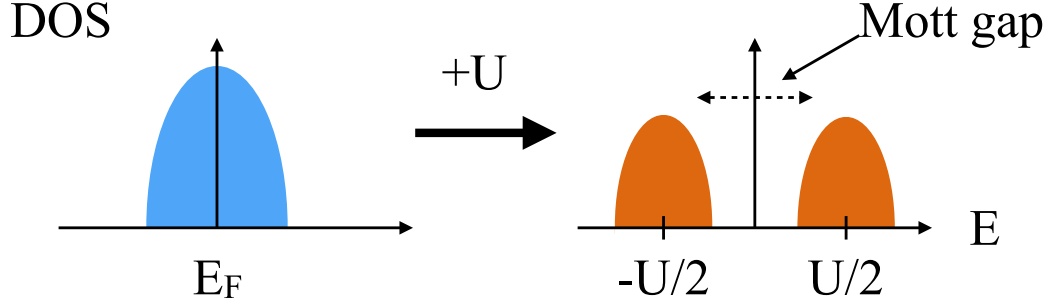


Figure 2.2: In a Mott insulator, strong electron correlation is underestimated and LDA will place a $3d$ band at the Fermi level, giving an un-physical metallic solution. By adding a Hubbard U , electrons tend to localize on lattice sites and the metallic band splits into upper and lower Hubbard bands, producing the correct insulating behaviour. In the same way, the population of up vs down electrons can be tuned, correcting erroneous moments.

it is often used as an empirical parameter to tune properties (e.g. magnetic moment or the band gap) until they are reasonable.

Several variations of the LDA+ U method has been implemented in WIEN2k[18] via the **orb** program. For the purposes of this dissertation (to deal with metal oxide systems), LDA+ U (SIC) is used for an approximate correction to orbital energies due to electron self-interaction effects in the spin-polarized case[19]. The full LDA energy functional including U therefore becomes:

$$\begin{aligned}
 E = E_{LDA} &- \left[U \frac{N(N-1)}{2} - J \frac{N(N-2)}{4} \right] \\
 &+ \frac{1}{2} \sum_{m,m',\sigma} U_{mm'} n_{m\sigma} n_{m'-\sigma} \\
 &+ \frac{1}{2} \sum_{m \neq m', m', \sigma} (U_{mm'} - J_{mm'}) n_{m\sigma} n_{m'\sigma}
 \end{aligned} \tag{2.14}$$

where N is the total number of electrons, n_{ab} are electron occupancies, U and J are spherical Coulomb and exchange parameters, and $U_{mm'}$ and $J_{mm'}$ are matrix representations of the non-spherical Coulomb and exchange parameters, respectively. It is usual in WIEN2k to use an effective $U_{eff} = U - J$ rather than separate Coulomb and exchange parameters, and using $J = 0$ for strong correlations of independent spin-bands. This allows for a much simpler form of Equation 2.14:

$$E = E_{LDA} + \frac{1}{2}U \sum_{m \neq m'} n_m n_{m'} - \frac{1}{2}UN(N-1) \quad (2.15)$$

where now the second term is equivalent to the on-site Hubbard term in Equation 2.13, and the final part is a double-counting correction. The combination of a Hubbard U correction with the full-potential LAPW method as implemented in WIEN2k allows for accurate descriptions of complex magnetic materials, such as $Y_{2-x}M_x\text{BaNiO}_5$ ($M=\text{Ca},\text{Sr}$)[18].

2.4 WIEN2k

The majority of calculations performed in this work were performed using the WIEN2k software package[20]. WIEN2k implements the linearised augmented plane wave (LAPW) method of solving the Kohn-Sham equations, and is one of the more popular DFT packages available at the time of writing this manuscript, with over 2600 licenses worldwide. WIEN2k is a set of modular fortran programs that enable a large variety of materials systems to be modelled. A model is created by following these general steps:

- A crystal structure is defined.
- An initial electron density is created using a sum of atomic densities.
- A *self-consistent field* cycle (SCF cycle) is started. In this cycle, the input electron density is used to calculate a potential. The Kohn-Sham equations are solved for this potential, giving a set of single-electron eigenvalues and eigenvectors (the Kohn-Sham orbitals). These are then used to update the electron density, and the cycle repeats from the beginning.
- The SCF cycle is run until convergence, typically of the total energy of the system.

From these models, a variety of materials properties can be calculated, including:

- ground state energy
- charge density and scanning tunnelling microscopy (STM) plots
- band structure and density of states (DOS)
- spin moments
- optical properties
- core binding energies
- X-ray spectra in the dipole approximation

- atomic forces

The base WIEN2k package can also interface with codes allowing for the calculation of excited states by BSE[21, 22], an all-electron implementation of the GW method[23], with various DMFT codes to better simulate highly correlated materials[24] (for example using Wannier functions as a basis[25]), and various phonon simulation code[26–28].

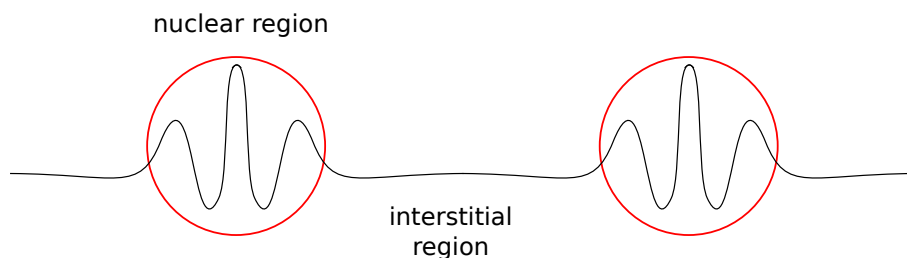


Figure 2.3: Depiction of a wave function between two atomic nuclei. The potential in the nuclear region causes the function to vary quickly rapidly within a certain radius, but slowly in the interstitial.

2.4.1 The all-electron (L)APW method

The key to WIEN2k’s success in its flexible approach to material modelling is that it fully describes all electrons in a system, rather than only a subset of valence electrons. Accurately simulating core electrons allows for a full range of materials properties to be calculated, beyond those that simply depend on the behaviour of the valence electrons (e.g. core spectroscopy). Including a large number of core and semi-core electrons in a calculation necessitates an efficient description of each electron.

The Kohn-Sham equations provide a starting point for solving the ground state of a material, but depend on wave functions that do not have an analytical form. In order to express these functions, it is necessary to project them onto a set of basis functions. Once in this basis, each wave function can be stored in computer memory as a vector of coefficients. The choice of basis functions are a limiting factor in how well this vector can describe the original non-analytical wave function, and should be chosen with an understanding of the physics of the underlying system.

In WIEN2k, solids are treated as periodic systems, therefore the Bloch theorem will apply[29]:

$$\psi_{\vec{k}}(\vec{r} + \vec{R}) = \psi_{\vec{k}}(\vec{r})e^{i\vec{k}\vec{R}} \quad (2.16)$$

where \vec{r} is a position vector, \vec{R} is a lattice vector in real space and \vec{k} is a crystal wave vector in reciprocal lattice space. The exponential term in Equation 2.16 is a *plane wave*, which can generally be used as a basis function to describe free electrons. By

extension, plane waves can be used as a basis set in a slowly-varying potential. To perform computations with a plane wave, it must be sampled and expressed as set of coefficients $c_{\vec{k}}$ up to some cut off K_{\max} :

$$\psi_{\vec{k}}(\vec{r}) = \sum_{\vec{k}}^{K_{\max}} c_{\vec{k}} e^{i(\vec{k}+\vec{k})\vec{r}} \quad (2.17)$$

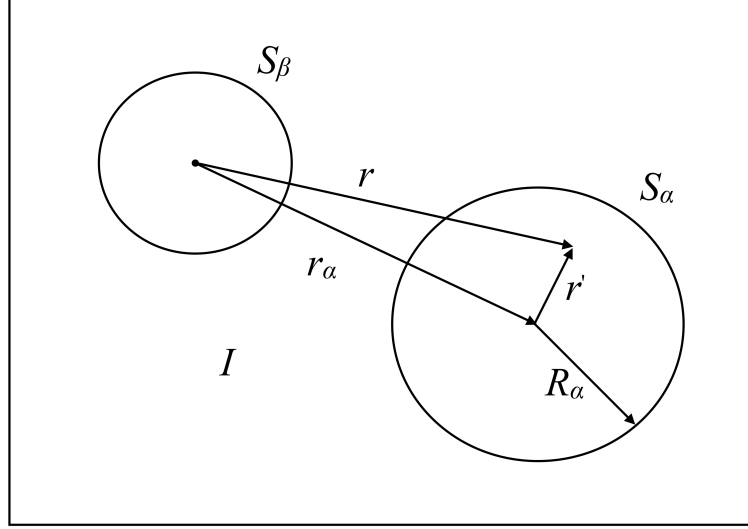


Figure 2.4: Division of space used in the APW method. Two atoms (S_α and S_β) are surrounded by interstitial region I . Within the sphere of radius \bar{R}_α centred at \bar{r}_α , wave functions will use S_α atomic orbitals as a basis. Reproduced from Ref. [30]

Unfortunately, in a solid system the potential varies rapidly in the vicinity of atomic nuclei, and a great deal of plane waves would be necessary to give a good description of a wave function in this region. Therefore it is desirable to *augment* the plane wave basis in the vicinity of the atomic sites, using basis function more akin to the bound atomic-like orbitals. One strategy for doing so (the *Augmented Plane Wave* (APW) method) begins by dividing the crystal up into two regions: spherical "muffin tins" centred on the atomic nuclei, and the interstitial volume between them, depicted in Fig 2.4 as first proposed by Slater[31]. Then, one of the basis vectors for atom S_α used to expand $\psi_{\vec{k}}$ would be:

$$\phi_{\vec{k},\vec{K}}(\vec{r}, E) = \begin{cases} \frac{1}{\sqrt{V}} e^{i(\vec{k}+\vec{K})\cdot\vec{r}} & \vec{r} \in I \\ \sum_{\ell,m} A_{\ell,m}^{\alpha,\vec{k}+\vec{K}} u_\ell^\alpha(r', E) Y_m^\ell(\hat{r}') & \vec{r} \in S_\alpha \end{cases} \quad (2.18)$$

where \vec{K} is sampled up to a K_{\max} on a reciprocal space \vec{k} -mesh and V is the real-space unit cell volume. Within the atomic sphere, solutions u_ℓ^α to the radial Schrödinger equation

of a free atom with spherical potential α are summed over the quantum numbers ℓ, m , weighted by coefficients $A_{\ell,m}^{\alpha,\vec{k}+\vec{K}}$. The atom is centered at \vec{r}' , with $r' = |\vec{r}'|$ being the distance from the centre of the atom, in direction \hat{r}' . $Y_m^\ell(\hat{r}')$ are the spherical harmonics.

In a free atom, the $u_\ell^\alpha(r, E)$ are solved for a boundary condition of vanishing magnitude as $r \rightarrow \infty$, which determine E . However, this boundary condition does not exist in an infinitely repeating solid. Instead, we enforce continuity of the function by choosing the A coefficients such that the plane wave contribution matches the atomic component at the sphere boundary (i.e. $r' = R_\alpha$).

Conceptually the APW basis would be useful for expanding a known set of wave functions. However, each basis vector is dependant on an energy eigenvalue that we wish to solve for. This can be improved by *linearizing* the APW basis set, known as the *Linearized Augmented Plane Wave* (LAPW) method[32]. This is accomplished by taking a one-term Taylor expansion around an atom-dependent energy E_l (which is pre-determined for low, physically relevant l's). The resulting basis functions:

$$\phi_{\vec{k},\vec{K}}(\vec{r}) = \begin{cases} \frac{1}{\sqrt{V}} e^{i(\vec{k}+\vec{K})\cdot\vec{r}} & \vec{r} \in I \\ \sum_{\ell,m} \left(A_{\ell,m}^{\alpha,\vec{k}+\vec{K}} u_\ell^\alpha(r', E_\ell) + B_{\ell,m}^{\alpha,\vec{k}+\vec{K}} \dot{u}_\ell^\alpha(r', E_\ell) \right) Y_m^\ell(\hat{r}') & \vec{r} \in S_\alpha \end{cases} \quad (2.19)$$

now include another coefficient B and the radial derivative $\dot{u}_\ell^{\alpha,\vec{k}+\vec{K}}$. Because another coefficient has been added, it is necessary to include another boundary condition to define these vectors, therefore the A's and B's are chosen such that the function matches in both value and slope (first radial derivative) at the sphere boundary.

The resulting basis set is quite flexible and can better describe the electronic states of a solid than plane waves alone. One challenge in using LAPW is to choose atomic muffin-tin radii (R_{MT}) such that rapidly-varying atomic-like functions are not being used to describe the slowly-varying interstitial potential and that plane waves are not being used too near the atomic nuclei. However, the accuracy of the LAPW basis can be largely controlled by a single parameter, namely the K_{max} cutoff which controls the period of the plane-wave components of the basis vectors. In WIEN2k, the product $R_{MT}^{min} K_{max}$ is used to control accuracy in a simple way. Since larger R_{MT} spheres will move the interstitial space further from the atomic nuclei (where the potential varies most rapidly), a lower K_{max} can be used to fit the potential, and vice versa. A typical value is $R_{MT}^{min} K_{max} = 6 - 9$ for good accuracy.

2.4.2 LAPW with Local Orbitals

While the LAPW basis provides a good description of electron behaviour in general, many of the electrons in a typical system are well bound to a single nucleus and will behave very similarly to an electron in an isolated atom. Such localized behaviour is

normal in core electrons that will not participate in chemical bonding. It is therefore unnecessary to expand core states with the LAPW basis (the plane wave components would be virtually nil), and WIEN2k instead treats them as if they were in isolated atoms, however under the full electron potential.

However, the case can occur that *semi-core* electrons exist in a system that are not completely bound to an atomic sphere, yet have the same l value as a valence electron with a higher principle quantum number n (for example, systems having both $3p$ and $4p$ electrons)[33]. Since the LAPW expansion described above depends on a linearisation energy E_l , it is no longer clear how to choose this energy (in the example, whether it correspond to the $3p$ or $4p$ states). To improve on the description of these more localized semi-core states, WIEN2k also includes basis functions of the form:

$$\phi_{\alpha,LO}^{\ell,m}(\vec{r}) = \begin{cases} 0 & \vec{r} \in I \\ \left(A_{\ell,m}^{\alpha,LO} u_{\ell}^{\alpha}(r', E_{1,\ell}^{\alpha}) + B_{\ell,m}^{\alpha,LO} \dot{u}_{\ell}^{\alpha}(r', E_{1,\ell}^{\alpha}) + C_{\ell,m}^{\alpha,LO} u_{\ell}^{\alpha}(r', E_{2,\ell}^{\alpha}) \right) Y_m^{\ell}(\hat{r}') & \vec{r} \in S_{\alpha} \end{cases} \quad (2.20)$$

where the $E_{1,\ell}$ and $E_{2,\ell}$ are a linearisation energy for the low and high binding energy states with quantum number ℓ , respectively. Because the state with higher binding energy will be more localized, it does not have a radial derivative term. The coefficients are chosen such the function goes to zero (and has zero slope) at the sphere boundary and is normalized within.

2.4.3 APW with Local Orbitals

While APW can be linearised as described above, its plane-wave convergence is slower than in the non-linearised APW method. It turns out to be more efficient to use another scheme for certain states, such as d and f states[34]. Instead, for these states WIEN2k will use an APW basis with a single linearisation energy, plus a local orbital (lo) to make up for the fact that the linearisation energy is not the true eigenenergy of the function[35]. This APW+(lo) basis can also be supplemented by further local orbitals with two linearisation energies when two states with different primary quantum numbers occur in the valence region (APW+lo+LO).

2.4.4 On-site Exact Exchange for Correlated Electrons (EECE)

In addition to providing many DFT functionals, the LAPW basis allows for specific potentials to be applied on a per-orbital basis, in much the same way as the LDA+U correction mentioned above. This can for example be used to apply a different potential to specific bands that are poorly described in DFT, such as correlated d or f electrons as described in Section 2.3.3. One method is to replace the exchange energy term of the DFT functional with a Hartree-Fock term that is exact. This replacement is *Exact Exchange for Correlated Electrons* (EECE)[36], though WIEN2k can also use this method to apply hybrid functionals[37].

The EECE functional uses an exchange correlation energy defined as:

$$E_{xc}^{EECE}[\rho] = E_{xc}^{LDA}[\rho] + \alpha(E_x^{HF}[\Psi_{corr}] - E_x^{LDA}[\rho_{corr}]) \quad (2.21)$$

where *LDA* references the underlying semilocal functional (e.g. LDA, GGA), Ψ_{corr} is the chosen orbital for which a Hartree-Fock exchange energy is calculated, ρ_{corr} the orbital density, and α is a mixing factor. The orbital is selected by projecting the correlated orbitals with angular momentum ℓ onto a given atomic sphere in the LAPW picture. This operation is therefore computational inexpensive, as these orbitals are easily selected in the LAPW basis set.

Surfaces and Surface Reconstruction

Unlike the periodic systems that are simulated in WIEN2k, every real material system has a boundary at some surface. Discontinuity of materials at their surface will give rise to much of their interesting physics and chemistry, as many practical uses of materials occur at or near surfaces. It is therefore important to study the details of material surfaces, their structure and their chemical behaviour in order to apply materials to a desired task.

For the purposes of this dissertation the materials to be considered are crystalline solids. While crystals can have very complex surface terminations depending on how they are prepared, it is most convenient to study simple terminations that can be exposed in large, atomically flat facets. Such facets are formed when a crystal structure is cut along a high-symmetry direction in the unit cell, and typically occur along the basis vectors. These facets are then labelled with Miller indices (hkl) where each index is a low integer (usually 0 or 1) indicating the number of unit cells in a crystal direction before intercept of the surface plane (0 is used in the case the surface runs parallel to an axis).

Because techniques exist to prepare high quality crystal facets that extend for distances substantially longer than the length scale of a local chemical environment, it is possible to simulate a surface using a periodic unit cell. Doing so requires the simulation of a *slab*, a unit cell that incorporates the repeat unit of the 2D surface with a vacuum layer above it and a bulk-like layer beneath it, as depicted in Figure 3.1. A slab should be thick enough that the bulk region behaves similar to a periodic model of the bulk, while the vacuum is large enough to prevent spurious interaction between the surface and its repeated images. In addition, a slab must be thick enough that its calculated properties of interest converge.

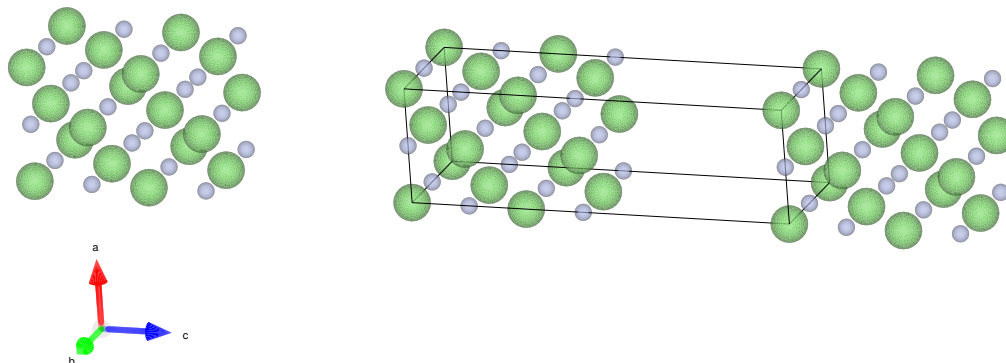


Figure 3.1: A simple slab structure of a rocksalt crystal. The unit cell is indicated by the solid line, and images of the unit cell are separated by a vacuum layer.

3.0.5 Surface Energy

When a surface terminates, there is a discontinuity in the bonding environment for the uppermost atoms which are now exposed to the crystal exterior. The result is a *surface energy*, or penalty for terminating the interior periodic structure. In the steady state the energy cost of creating a surface must be positive; if this were negative, creating a surface would lower the energy of the system in question and surfaces would spontaneously form. In a simulated slab, surface energy γ is typically expressed per unit surface area:

$$\gamma = \frac{E_{slab} - NE_{bulk}}{2A} \quad (3.1)$$

where A is the slab surface area per unit cell, E_{bulk} is the energy per atom of the bulk unit cell and E_{slab} is the total energy of the slab structure. A slab must have two identical surfaces, hence the factor of 2 in the denominator.

3.0.6 Surface Reconstruction

The existence of a surface energy means there is thermodynamic driving force to minimize it. As a result, the atoms in the vicinity of the surface can rearrange to find an equilibrium position different than in the crystal interior. For example, atoms can move to change their coordination number, can undergo a change in oxidation state, or can move into positions with different symmetry. The total number of atoms in a surface layer can change, potentially changing the local material stoichiometry. A surface can also be stabilized by adsorbates, depending on the environment.

In the interest of simulating surfaces with a periodic method, this dissertation is interested in surfaces that are regular and have finite units of repetition. Such surfaces can

be described with respect to the unit cell of the underlying bulk termination as a superstructure using: Wood's notation: $(m \times n)R\phi$, where m and n are multiples of the bulk basis vectors in the surface plane, and ϕ is a rotation. For example, Chapter 5 describes a $(\sqrt{2} \times \sqrt{2})R45^\circ$ reconstruction of the magnetite (001) surface. This naming convention is convenient, as it can be easily determined by LEED (see section 4.3).

3.0.7 Polar Considerations

A material composed of more than one atom can be separated into cations and anions on the basis of valence charge transfer. It can be helpful in understanding such a material's polar properties by modelling it as a collection of point charges. By replacing each atom in the structure with a point charge equivalent to the formal oxidation state of the atom, one can gain a simple understanding of any polar effects occurring within a given structure. While typically a bulk material should not have a permanent electric dipole in its ground state, there can be important polar effects at material interfaces or surfaces[38]. For the purposes of this work it is important to consider the implications of a surface reconstruction with a polar termination.

Given a crystalline material (with a corresponding unit cell) and considering an appropriate crystal direction it is possible to consider a material to be *layered*[39]. In a layered material, there is usually some stacking order in which the layers repeat (e.g. ABAB, ABCABC, ABACA, etc...). Considering again a point charge model, it is useful to sum up the charges on each layer to find its charge per unit cell. This now reduces the task of searching for any dipoles to a 1-dimensional problem.

There are in general three types of layered surfaces that can result, as defined by Tasker[40]:

- Type 1, where each plane contains both anions and cations, but achieves overall neutrality
- Type 2, where the planes are charged, but stack in such a way as to prevent a net dipole moment from accumulating, and
- Type 3, with charged planes and a net dipole moment.

If a material's structure does lead to a bulk dipole moment, as in Type 3, termination at a simple surface will lead to a divergent surface energy. This can be thought of as an uncompensated charge imbalance creating a voltage across the surface layers. This voltage will increase with each subsequent layer, leading to a so-called *polar catastrophe*. In principle such a surface cannot exist in a single facet; instead it must compensate break into multiple terraces or facets to reduce the net dipole. In the simplest geometry (alternating layers of equal charge σ and equal layer spacing) to prevent such a divergent surface energy, it is necessary to apply a surface charge with half the magnitude of the repeating charge. This situation is depicted in Figure 3.3, and results in a finite surface

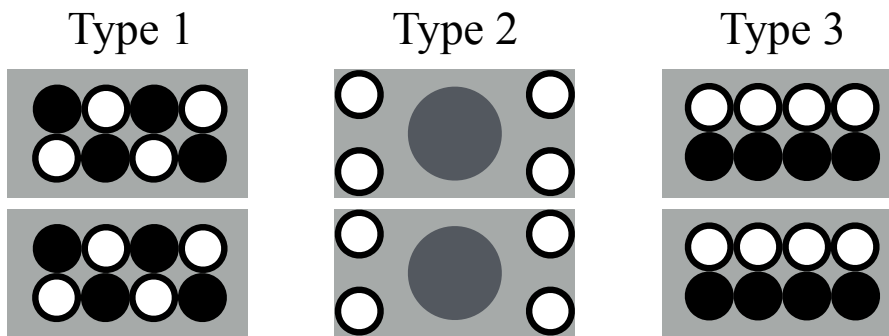


Figure 3.2: Tasker's three surface terminations for non-metallic surfaces. Layers in type 1 surfaces have no net charge. Type 2 surfaces have charged layers, but no macroscopic net dipole. Type 3 surfaces accumulate a net dipole, which must somehow be relieved.

energy that does not depend on slab thickness. For an example of a diverging surface energy, see Figure 5.4.

It has been shown that the polar catastrophe can be prevented in general, for layers spaced by distances R_1 and R_2 by m outer layers with charges σ_j [39]:

$$\sum_{j=1}^m \sigma_j = -\frac{\sigma_{m+1}}{2} \left[(-1)^m - \frac{R_2 - R_1}{R_2 + R_1} \right] \quad (3.2)$$

Such a multi-layer termination will be discussed in Chapter 5.

Of course, real surfaces are not composed of layered point charges, and so other physical effects can occur to stabilize a polar surface. Metallic systems, for example, have mobile valence electrons which can redistribute themselves to counteract a dipole. In non-metallic systems, cations or anions can change oxidation state, leading to a charge transfer between layers. Alternatively, surfaces can be stabilized by adsorbates, such as O, OH^- , etc. Also, layer spacing can change, with surface atoms typically relaxing towards the bulk.

3.1 Surface Phase Diagrams

Determining the structure of a surface requires some metric with which to compare surface energies. For surfaces with variable composition, one method is to compare structures using a *surface phase diagram*. In the case of a material in contact with an atmosphere, the surface behaves like a diaphragm connecting two reservoirs: the material bulk and the atmosphere. When annealing, mass flow can occur in either direction until a chemical equilibrium is reached. Since composition can change in such a system, it is necessary to convert from a simple surface energy to a *surface free energy* that can vary with the number of atoms. A suitable thermodynamic potential to use in constructing this is the Gibbs free energy G [41][42]:

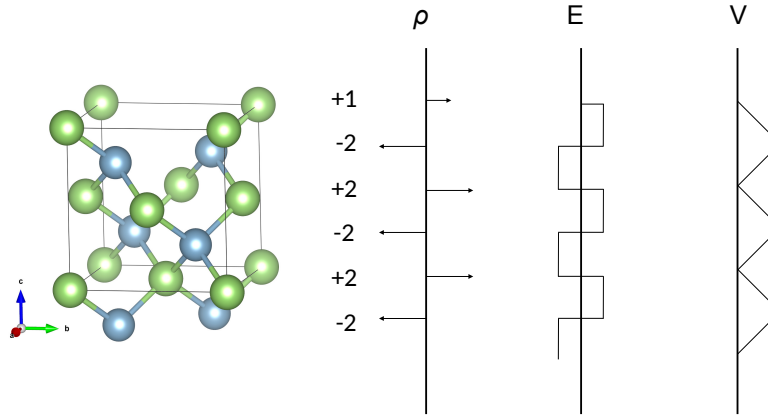


Figure 3.3: A generic FCC structure with a compensating surface termination layer of $\frac{1}{2}\rho$. Such a surface has a converging surface energy.

$$G(p, T) = E + pV - TS \quad (3.3)$$

where E is the internal energy of the system (usually called U in the chemistry context, but here made consistent with DFT terminology), with a pressure p acting on the system's volume V , and with a total entropy S at temperature P . Therefore, at a surface we can express the surface free energy γ as:

$$\gamma(p, T) = \frac{1}{A} \left[G(p, T, N_A, N_B, \dots, N_x) - N_A \mu_A(p, T) - N_B \mu_B(p, T) - \dots - N_x \mu_x(p, T) \right] \quad (3.4)$$

where N_x are the number of chemical species x in the sample, and μ_x are their chemical potentials. As mentioned in Section 3, in a periodic DFT code we can model a surface as slab with two identical surfaces, leading to a factor of $1/2A$ per surface free energy of G^{slab} . In addition, since the surface is in contact with the material bulk as one thermodynamic reservoir, the chemical potential of each surface atom cannot vary independently. Instead, they are related through the stoichiometry and Gibbs free energy of the bulk composition, g^{bulk} . Simplifying Equation 3.4 for a binary compound A_xB_y , we therefore have the relation:

$$X\mu_A(p, T) + Y\mu_B(p, T) = g_{A_xB_y}^{bulk}(p, T) \quad (3.5)$$

where g^{bulk} is the Gibbs free energy per formula unit. Combining Equations 3.4 and 3.5 we therefore have γ in terms of a single chemical potential, which can be controlled

experimentally by varying the pressure and temperature of the atmosphere reservoir, for example. This results in a 2-dimensional surface phase diagram for a binary compound, with higher dimensions necessary as additional elements are added.

To construct a surface phase diagram requires choosing the limits of the experimentally controlled potential. For example, in a binary solid A_xB_y one can consider two endpoints of the energy diagram: the potential that will force spontaneous formation of either component in the bulk, rather than their mixture in the binary solid. For example, in a metal oxide system MO_x , where oxygen in the atmosphere above the surface is the most easily controlled potential, the two endpoints would be:

- low μ_O (high μ_M) such that O is forced from the oxide and bulk M (in the most stable phase at experimental conditions) spontaneously forms: $\mu_M = g_M^{bulk}$
- high μ_O (low μ_M) such that O_2 begins to spontaneously condense onto the sample surface: $\mu_O = \frac{1}{2}E_{O_2}^{total}$

To compute a surface phase, we must relate a DFT total energy E with a desired Gibbs free energy g . DFT simulations can be considered to be a Helmholtz free energy at zero temperature and pressure. In this picture, the TS term of equation 3.3 will be contained by phonon energies, shown to cause a $\pm 10 \text{meV}/\text{\AA}^2$ deviation in γ for $P < 100 \text{ atm}$ and $T < 1000 \text{ K}$ in RuO_2 [42]. Ground-state vibrations that cannot be considered in the time-independent Kohn-Sham picture are neglected. The pV term remains, but is on the order of $10^{-3} \text{ meV}/\text{\AA}^2$ under reasonable experimental conditions. It is therefore possible to use DFT total energies in place of free energies, provided an error of $\approx 10 \text{ meV}/\text{\AA}^2$ can be tolerated.

Therefore, a surface phase diagram can be built using total energies of the surface slabs under study as well as the bulk or molecular forms of each element in the slab. Once constructed, it can be more helpful to convert chemical potentials into a temperature or pressure range, for example, of an O_2 atmosphere above a sample being annealed. This is possible using a combination of thermochemical tables (to provide the entropy and enthalpy of constituents as a function of temperature) and the following relation with respect to a standard pressure p^0 :

$$\mu(p, T) = \mu(p^0, T) + \frac{1}{2}kT \ln\left(\frac{p}{p^0}\right) \quad (3.6)$$

Experimental Methods of Studying Surfaces

There are many experimental techniques that can be used, either specifically or non-specifically, to study the properties of thesis. Sometimes this is accomplished by tuning an experiment to be more "surface sensitive". That is, one somehow modifies an experiment to restrict an otherwise be a bulk measurement to the surface regime. Other experiments are constructed in such a way as to only be applicable to surfaces. In this chapter, some surface techniques used in the remainder of this dissertation are discussed, especially in their relationship to theoretical methods.

4.1 Scanning Tunneling Microscopy

Scanning tunneling microscopy (STM) is a very powerful technique for retrieving real-space information about a material surface with atomic resolution. First pioneered in 1982 by Binnig and Rohrer[43], STM has quickly become one of the most important experimental methods in the field of surface science. STM allows for facile measurement of a wide variety of metallic and semiconducting materials, and has resulted in complex surface reconstructions being solved[44], manipulation of individual atoms on a surface[45] and visualization of quantum mechanical effects at a surface (e.g. the "quantum corral"[46]).

STM operates by bringing an "atomically-sharp" tip (typically of Pt or W) to within a few angstroms of a surface until a tunnelling current (typically measured in nA) can be measured when a bias voltage is applied. A sample surface can then be imaged by rastering in X and Y, while maintaining a constant height in Z (constant height mode) or a constant tunnelling current while changing height in Z (constant current mode). The measured tunnelling current is proportional to the localized density of states (LDOS) beneath the STM tip, and gives information about the location and shape of electronic

states at the surface. Depending on the bias voltage polarity, electrons can either tunnel into unoccupied conduction band states, or out of occupied valence band states. Most importantly, atomic resolution can be achieved, allowing the physical structure of a surface to be directly imaged.

For the purposes of this work, it is necessary to have a basic understanding of the theory of STM operation. In WIEN2k, the Tersoff-Hamann approximation[47] is used to transform the internal representation of the quantum state of a system (charge density) into a simulated STM image. This theory begins with a description of the tunnelling current I across a tip-surface gap as described by Bardeen[48]:

$$I = \frac{2\pi e}{\hbar} \sum_{\mu,\nu} f(E_\mu)[1 - f(E_\nu + eV)]|M_{\mu\nu}|^2\delta(E_\mu - E_\nu) \quad (4.1)$$

where $f(E)$ is the Fermi function, V is an externally applied bias, μ and ν represent the states of the tip and the surface, respectively, and $M_{\mu\nu}$ is the tunnelling matrix element between tip state ψ_μ and surface state ψ_ν . Under low-temperature conditions one ignores reverse tunnelling. Additionally, under a low applied bias with respect to the Fermi energy E_F , Equation 4.1 simplifies to:

$$I = \frac{2\pi}{\hbar} e^2 V \sum_{\mu,\nu} |M_{\mu\nu}|^2 \delta(E_\nu - E_F) \delta(E_\mu - E_F) \quad (4.2)$$

To model further from this point requires information about the tip and surface geometry. Since, by its nature, tunnelling current decays exponentially with distance, it is reasonable to approximate the STM tip as a point source. This can be interpreted as the atom or broken bond nearest to the surface, which will dominate in any tunnelling. In this localized limit, Tersoff and Hamann model the tip as a spherically symmetrical potential well with radius R at position r_0 a distance d above the surface, as depicted in Figure 4.1

In this case the tunnelling matrix elements $M_{\mu\nu}$ are simply proportional to the amplitude of the surface states ψ_ν at the tip point r_0 :

$$I \approx \sum_{\nu} |\psi_\nu(\vec{r}_0)|^2 \delta(E_\nu - E_F) \quad (4.3)$$

Further evaluation of this expression is possible in the interest of better quantifying the current (for example, in trying to determine the lateral resolution Δx of the method). In doing so, the most important approximations are that the work function of surface and tip are equal (which should be roughly correct in the low-bias approximation) and that only spherically symmetric states from the tip contribute to tunnelling (the s -wave approximation). Tersoff and Hamann demonstrate that these approximations affect the coefficient of proportionality between the tunnelling current and the LDOS, but with only small errors. The s -wave approximation is most notable for our purposes in

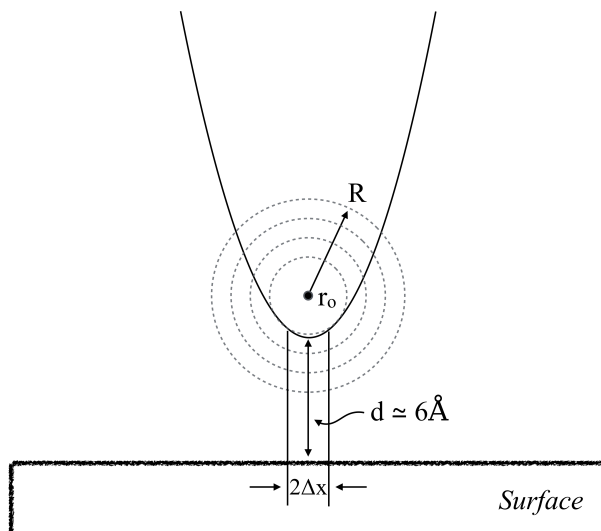


Figure 4.1: Idealized STM tunnelling geometry. The scanning tip is modelled as a spherical emitter at point r_0 with radius R . The nearest distance to the surface d (typically $\sim 6 \text{ \AA}$) gives the greatest contribution to tunnelling current. Tip states are considered to be spherically symmetrical s -waves.

that it underestimates the lateral resolution possible in STM. For example, it has been demonstrated that the s -wave model breaks down in the case of imaging graphite, where the tip electronic states become important[49]. However, since this breakdown of the simple model described above leads to an *improvement* in lateral resolution, it will not be considered in this work.

4.1.1 Simulating STM in WIEN2k

For the purposes of this work, simulated STM images are created to compare with experimental measurements made in one of two modes: *constant current* and *constant height*. During a *constant current* measurement, a feedback mechanism is used to adjust the height of the scanning tip above the surface in order that the tunnelling current remains constant. Thus as the surface beneath the tip changes, the tip height will be adjusted so as to avoid a collision. On an atomically flat surface it is also possible to disable this feedback and conduct a *constant height* measurement.

In WIEN2k, a simulated *constant height* image is trivial to construct using the **lapw5** utility, which produces charge density plots for a specified plane within the unit cell. The plane is sampled at a specified resolution and the sum of the spin-up and spin-down valence density at that point is output. By using a plane parallel to the surface of a model slab, varying its height from the surface and adjusting the contrast of the resulting plot it is possible to make a reasonable approximation of an experimental scan.

To simulate a *constant current* measurement, **lapw5** can be put into an STM mode with

a target density level. In this mode, for each point of the specified plane the code conducts a search above and below the plane for the target density, then outputs the height at which it occurs. This simulation method is more suitable for more complex surfaces, such as those that are not atomically flat, containing steps or open areas, as these areas may lead to large changes in the point charge density. In the WIEN2k implementation it is currently not possible to use the STM mode in such a way as to intersect at RMT sphere around an atom, but this is not typically an issue when simulating realistic tip-surface distances

In both types of simulation, it is important to restrict the charge density used by **lapw5** to a small energy range around the Fermi energy. This corresponds with the summation over surface states ν as described in Equation 4.3, with the Fermi energy as one of the end points, and can be accomplished with **lapw2**. For example, to simulate an STM image of the unoccupied states in the first 0.25 Ry above a Fermi level of 0.5 Ry (i.e. a 3.4V bias voltage), the following command will sum the appropriate states:

```
x lapw2 -all 0.5 3.0 (-up/-dn)
```

Afterwards, **lapw5** will utilize this subset of the total charge density when producing plots.

4.2 X-ray Spectroscopy

X-rays, which are emitted from core-level electron transitions, serve as useful probes of materials for several reasons:

- They provide elemental sensitivity, due to different elements having sharp, uniquely spaced core binding levels.
- They attenuate slowly through matter, allowing for a good penetration of X-rays being used for excitation or as information carriers.
- They can be easily generated under a variety of conditions, for example in monochromatic, collimated beams

For the purposes of this work, soft X-rays (X-rays with energy less than 2000 eV) were used to conduct spectroscopic measurements under a variety of conditions.

4.2.1 X-ray Photoelectron Spectroscopy

When an photon of sufficient energy is adsorbed by an electron, it can be freed from the potential well of the material it is bound to, becoming a photoelectron. When exciting core-level electrons this process is called *X-ray Photoelectron Spectroscopy* (XPS)[50, 51]. XPS serves as a surface-sensitive probe of the elemental composition of a material, and is also sensitive to the local chemical environment about atoms through small shifts

in electron binding energy. Valence band electrons (VB XPS) can also be measured, particularly through the use of a tunable X-ray source to bring the exciting beam closer to resonance. X-ray energy tuning can also affect the adsorption cross-section of different elements, leading to peak intensity shifts that reveal electronic structure that would otherwise be hidden under experimental broadening.

An XPS experiment is typically conducted under high vacuum conditions (to prevent adsorption or inelastic loss of photoelectron energy), and consists of the following general components:

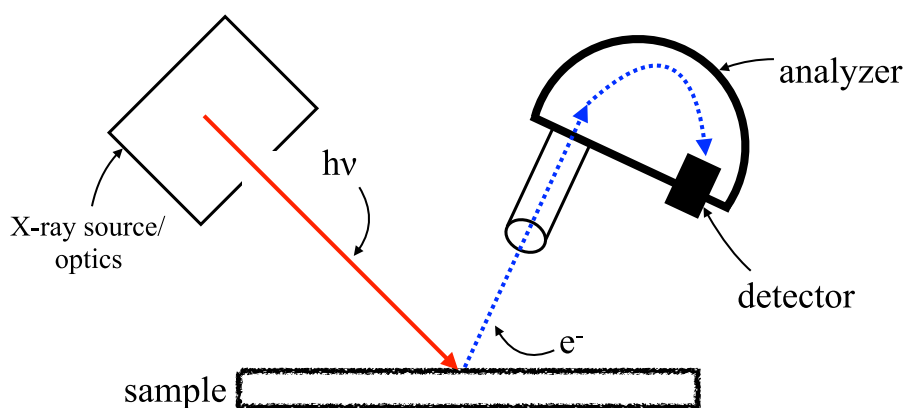


Figure 4.2: Experimental setup of an XPS measurement.

- An X-ray source, usually an X-ray tube where electrons are accelerated into a metal anode (typically Mg or Al) to produce Bremsstrahlung X-rays. These X-rays are then reflected off a crystal (e.g. quartz) to produce a monochromatic beam.
- Focusing optics to produce an X-ray beam with a known spot size.
- The material under study, ideally with a flat surface
- An electron analyser, which separates electrons of different kinetic energy using magnetic fields
- An electron detector, which counts the electrons of a particular kinetic energy

Electron binding energies can be determined from the measured kinetic energy spectrum using the following equation:

$$E_{binding} = E_{photon} - (E_{kinetic} + \phi) \quad (4.4)$$

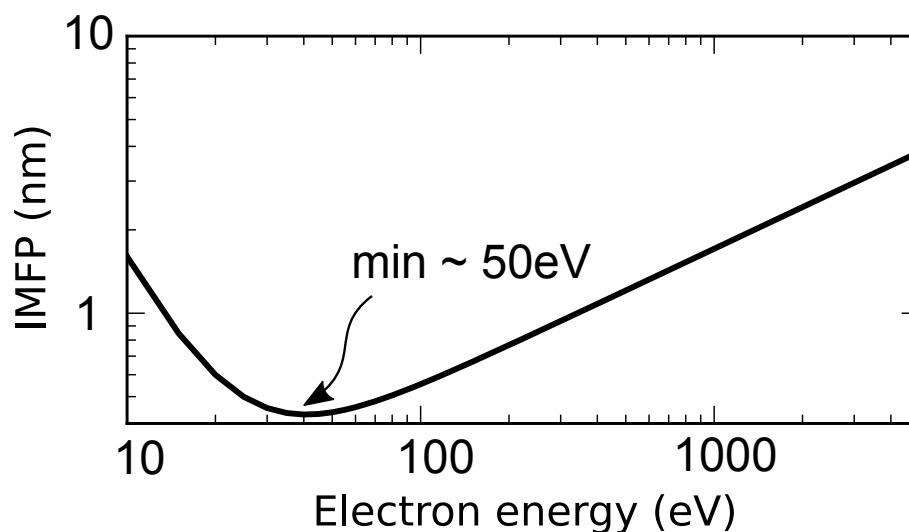


Figure 4.3: Universal curve for electron inelastic mean free path through a solid. Based on Equation 5 from Ref [52].

where E_{photon} is the known energy of the incoming X-ray and ϕ is the work function of the material under study.

Since the escaping photoelectrons serve as the information carrier in this experiment, the surface sensitivity of XPS is determined by the inelastic mean free path through which an electron can leave the material under study. This mean free path has a minimum of ≈ 0.5 nm at between 40-60 eV kinetic energy, and then increases with higher energies (up to 5nm under typical XPS exciting radiation). If an X-ray source with tunable energy is used (such as a synchrotron) there can be some control of the surface sensitivity of a measurement, but this is most often achieved by changing the experimental geometry to a grazing angle. By angling the sample surface such that the incoming X-ray beam and outbound path to the electron analyser are at grazing angles, the path length through the material is maximized, thus attenuating photoelectrons generated deeper within the surface. Changing the sample angle is therefore used to quickly probe different depth regimes, to give an idea of "bulk" versus "surface" chemical environments.

4.2.2 X-ray Absorption Spectroscopy

If an absorbed X-ray does not have sufficient energy to free an electron from a material, it can instead promote the electron to a bound, unoccupied state. Since the majority of unoccupied states in a system are above the Fermi level, X-ray absorption spectroscopy (XAS) provides an elementally specific probe of a material's conduction band. As we are specifically interested in conduction band information, only the lowest energy transitions that do not undergo further scattering processes are of interest; this is known as X-ray absorption near edge structure (XANES) or near edge X-ray absorption fine structure

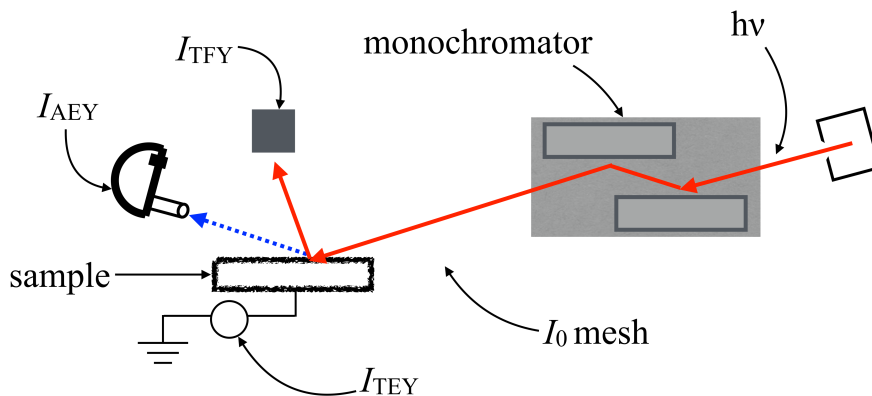


Figure 4.4: Setup of a synchrotron XAS experiment, with TFY, TEY and AEY being measured.

(NEXAFS)[53].

An X-ray absorption experiment consists of the following general elements:

- A monochromatic X-ray source, most typically produced by a synchrotron bending magnet or other insertion device refracted off a crystal monochromator. The source must have tunable energy E in order to sweep over the absorption edge of interest.
- A metallic mesh, used to measure the beam current $I_0(E)$ before it impinges on the sample under measurement.
- The sample, connected to ground to prevent charge from building up as electrons leave
- A detector, to be described below, that measures the degree to which the X-ray beam is absorbed.

A depiction of the experimental set up can be seen in Figure 4.4.

As the incoming X-rays are absorbed by the sample, it is the goal to measure an absorption co-efficient $\mu(E)$. Ideally, total absorption of an X-ray beam passing through a sample is measured by placing another detector behind the sample to measure another beam current $I_t(E)$. Then the absorption co-efficient is simply:

$$\mu(E) = \frac{1}{t} \ln \left(\frac{I_0(E)}{I_t(E)} \right) \quad (4.5)$$

where t is the uniform sample thickness. Unfortunately, this type of *transmission* measurement is only possible if the X-ray beam is not fully absorbed by the sample,

which typically occurs for the low X-ray energies used to probe the K edges of light elements. Instead, another process that is the result of the X-ray absorption must be measured, and assumed to be linearly related to $\mu(E)$. For the purposes of this dissertation, two such measurements are considered:

- When a core electron is promoted to the conduction band in the vicinity of the sample surface, while it may remain bound to the sample for a relatively long period of time relative to the excitation process, it may eventually cause a secondary electron to be ejected from the surface. If the sample is conducting and connected to ground, the ground current $I_{TEY}(E)$ can be measured. The so-called *total electron yield* (TEY) is then the ratio of $I_{TEY}(E)$ to $I_0(E)$. At energies below 1000 eV, these electrons escape from a depth of up to 2 nm [54].
- In elements with multiple core levels (e.g. a $1s$ and a $2s$ level below the valence band), after an X-ray absorption event the resulting core hole can be refilled by another core electron (e.g. a $2s \rightarrow 1s$ transition). The transition energy is then imparted to a valence level electron, which when ejected from the sample is known as an *Auger electron*, as depicted in Figure 4.5. Auger electrons have low kinetic energy, and hence a low mean free path within the sample. Therefore, if an Auger electron current $I_{AEY}(E)$ can be collected with an electron analyzer (as described in Section 4.2.1 above), then it is known to have occurred within a few atomic lengths from the surface, making the *Auger electron yield* (AEY) an extremely surface sensitive measurement of $\mu(E)$. An example of the Auger lines used to measure AEY in SrTiO_3 is shown in Figure 6.3.
- While not used in this work, the relaxation of an X-ray excited atom can, through a number of processes, result in the emission of another X-ray, usually of lower energy, a process known as fluorescence. These fluorescent X-rays have an attenuation length through the sample similar to the exciting X-ray, allowing a measure of $\mu(E)$ from within the bulk, though subject to distortion due to re-adsorption. A fluorescence current $I_{TFY}(E)$ can be measured with a photodiode or channel plate detector, yielding the *total fluorescence yield* (TFY). If an energy sensitive detector is used to measure the fluorescence, a particular decay channel can be chosen to eliminate background radiation, giving the *partial fluorescence yield* (PFY). If a sample has a strong decay channel at lower energy than the adsorption edge being measured, such as a lower energy core level transition, the *decrease* in PFY of that channel, or the *inverse partial fluorescence yield* (IPFY), provides a bulk-sensitive measurement of $\mu(E)$ without self-adsorption effects[55].

If adsorption is measured beyond the near edge, excited core electrons will not be bound and instead become propagating photoelectrons. As they propagate away from the core, there is backscatter interference from the surrounding atoms, which appears as a modulation of $\mu(E)$. By Fourier transforming $\mu(E)$ over an extended energy range above the adsorption edge it is possible to recover scattering intensity as a function of radial

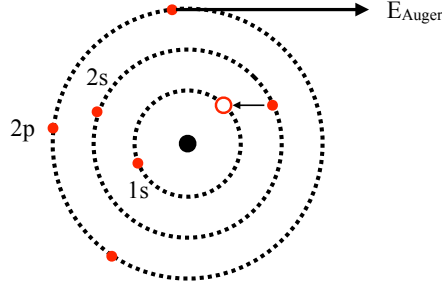


Figure 4.5: An example of a $KL_1L_{2,3}$ Auger electron process, where a $1s$ core hole is filled by a $2s$ electron, with the resulting kinetic energy imparted to a $2p$ electron.

distance; this is known as extended X-ray absorption fine structure, or EXAFS[56]. Since the core electrons can be selectively excited by the necessary tunable X-ray source, this measurement provides information about the coordinating environment about the atoms of a particular element in a sample.

4.2.3 Theory of XAS

Considering the interaction between a classical X-ray and an electron, we can use Fermi's golden rule to describe a transition through the transition operator T [57][58]:

$$T = -\frac{e}{mc} \exp\left(i\frac{E_f - E_i}{\hbar c} \hat{n} \cdot \vec{r}\right) \vec{p} \cdot \vec{A} \quad (4.6)$$

where E_i and E_f are the energies of the initial and final states, \vec{A} is the vector potential of the X-ray field propagating in direction \hat{n} , and the absorbing electron has position \vec{r} , angular momentum \vec{p} and mass m . In the case of low-energy transitions ($E_f - E_i \ll \hbar c/|\vec{r}|$) the argument to the exponential is small, and can be taken as the first term of a Maclaurin series expansion:

$$f(x) = f(0) + f'(0)x + \frac{f''(0)}{2!}x^2 + \dots \quad (4.7)$$

leading to a result of unity, and when considering excitation by linearly polarized radiation ($\vec{A} = A\hat{e}$) gives the so-called *dipole approximation* for initial state i and final state f :

$$T_{i \rightarrow f} \simeq -\frac{eA}{mc} \vec{p} \cdot \hat{e} \quad (4.8)$$

An important consequence of the dipole approximation is that the X-ray transition probability $\Gamma_{i \rightarrow f}$ is non-zero under certain selection rules. Specifically, if $\Gamma_{i \rightarrow f}$ is expressed in terms of spherical harmonics, which well describe core electrons:

$$\Gamma_{i \rightarrow f}(\hat{e}) \approx \left| \sum_q Y_{1q}^\dagger(\hat{e}) \langle \psi_f | r Y_{1q}(\hat{r}) | \psi_i \rangle \right|^2 \delta(E_f - E_i - h\nu) \quad (4.9)$$

This transition probability is significant only when $\Delta\ell = \pm 1$, $\Delta m = 0, \pm 1$ and there is no change in electron spin, $\Delta s = 0$. Overall, it can be considered that total angular momentum j during the transition must be conserved. For example, a $1s \rightarrow 2p$ transition is allowed, and will have a non-zero transition probability. For increasing l (e.g. quadrupole and higher order transitions), the transition probability decreases with the square of the exponential in equation 4.6. This corresponds to taking the second term of the Maclaurin series expansion ($e^{i\vec{k} \cdot \vec{r}} \approx 1 + i\vec{k} \cdot \vec{r}$), and explains why quadrupole transitions become more prevalent as transition energies increase (i.e. $E_f - E_i$ becomes significant compared to $\hbar c/|\vec{r}|$).

The breakdown of the dipole approximation becomes particularly important in *electron energy loss spectroscopy* (EELS) which can also be used to measure core transitions through energy-loss near-edge structure (ELNES). Because the core transitions in EELS are caused by high energy electrons (typically in a transmission electron microscope (TEM) with energies on the order of 100 keV), both the low energy and low momentum transfer approximations used above no longer hold. Instead it is necessary to calculate a full transition matrix, which becomes dependant on excitation energy and the relative orientation of the sample and beam. However, because a modern TEM can measure energy loss on a pixel-by-pixel basis there is the possibility to conduct spatially resolved spectroscopy of the conduction band of a material with up to atomic resolution.

4.2.4 Simulating XAS in WIEN2k

Within the LAPW formalism used in WIEN2k, X-ray absorption can be calculated as a transition intensity between a core level and a conduction band state within the R_{MT} sphere, since the core wave function will usually be zero outside the sphere (and particularly so for transitions to $1s$ states). Considering equation 4.9, it is necessary to sum over magnetic moments m and crystal momenta q , as they cannot be freely experimentally selected for during an experiment. However, the use of polarized light allows for some control of the m transition in highly oriented systems, allowing for example states with P_z or $P_{x,y}$ symmetry to be selected. The result is then the product of the local, partial density of states decomposed into the proper symmetry $\rho_l(E)$ with a radial transition matrix element with the form[59–61]:

$$\left[\int r^2 u_{\ell_{core}}(r, E_{core}) r u_\ell(r, E) dr \right]^2 W(\ell_{core}, 1, \ell) \quad (4.10)$$

where W is a Wigner 3j symbol[62], r is the distance from the nucleus of the atom in question, and the core subscript indicates the initial electron state.

To simulate an absorption spectrum in WIEN2k requires four main steps

- The decomposed, partial charge density is calculated with **x lapw2 -qtl**.
- Using this, the density of states for $(\ell + 1)$ and $(\ell - 1)$ around the desired edge quantum number are calculated with **tetra** using the modified tetrahedral method[63].
- The radial transition elements are calculated with **txspec**, and multiplied with the partial DOS by **xspec**.
- The spectrum is broadened with the **lorentz** program, to account both for state lifetime and spectrometer broadening.

However, the steps above neglect one of the greatest physical considerations of the problem: the final state being described during an X-ray absorption event is not the time-independent ground state of the system. The system is instead perturbed by a core-hole, a short lifetime non-equilibrium event. Density Functional Theory as introduced in Section 2 only allows one to describe the ground state of a system of independent quasiparticles (the independent particle approximation) that approximates a solid system. It is therefore necessary to construct a system with a ground state that approximates the excited state of the system of interest. While such a system will not describe exactly the physics of a electron-hole pair, it can provide a first approximation of the change in core shielding that will occur. Core-hole effects are particularly important in non-metallic materials, as the valence electrons do not have the ability to screen the hole charge[64].

In WIEN2k we can create a "frozen" core-hole in a system by selectively removing a core-level electron of choice by modifying the core level occupation the input files. The occupation can be adjusted by non-integer amounts, allowing for "partial" core-holes that allow a degree of control over the strength of the effect and the resulting relaxations in the electronic structure. Because the structure is periodic, one must isolate this introduced core-hole, in order to prevent spurious self-interaction. This is accomplished through a *supercell*, which has the effect of increasing the size and cost of converging the system. In some cases a supercell becomes infeasible due to the size of the unit cell under study, in which case it is important that core hole images are separated by some reasonable distance.

It is also important to compensate for the charge that has been removed, and WIEN2k provides two methods for placing the former core electron into the system. The first is to add an additional electron when filling states in **lapw2**, occupying a state that would otherwise be unoccupied in the ground state. While this seems to physically correspond to the situation occurring during an experiment, the specifics of the conduction band minimum can potentially cause unintended results. For example if the conduction band edge is dominated by states from an atom other than where the core-hole sits, the effects of charge transfer between atoms could be overstated. Alternatively, a uniform background charge can be applied in the **mixer**, which prevents any particular unoccupied state from being filled. The better method to use depends on the electronic structure of the system.

Using similar electronic structure models, it is also possible to simulate EELS spectrum in WIEN2k using the **telnes3** module[65]. This is accomplished by calculating a double differential scattering cross section (DDSCS) over a grid of energy loss ($E_f - E_i$) and impulse transfer (\vec{p}) vectors, allowing the transition operator in Equation 4.6 to be computed for any desired orientation. The formalism allows transitions of arbitrary order (i.e. beyond the dipole approximation) to be calculated in a fully-relativistic manner.

4.3 Low Energy Electron Diffraction (LEED)

One of the earliest methods of probing the structure of a material surface with high resolution is the use of diffracted beams of low energy electrons ($E_k < 500$ eV). In fact, the observation by Davisson and Germer of diffraction patterns in electrons backscattered from the surface of crystalline nickel served as the first experimental confirmation of the wave-like nature of matter proposed by de Broglie[66][67]. While considerable technical development was required before Low Energy Electron Diffraction (LEED) could provide useful information about surface reconstructions (e.g. ultra-high vacuum systems to allow clean surfaces to be measured), the low penetration depth of these low energy beams is one of the best methods of probing a material surface for structural information.

A LEED experimental setup consists of the following general components:

- An electron gun, typically consisting of a cathode filament held at a negative bias versus the sample, along with electron optics to produce a collimated, monoenergetic beam.
- A sample mount, where a prepared sample is fixed with its surface normal along the beam path.
- A display system, consisting of biased grids to accelerate the diffracted electron beams into a spherical fluorescent screen. The sample is positioned in the centre of this sphere, which results in a direct measurement of the reciprocal lattice of the crystal surface.

A diagram of the apparatus and a sample LEED image can be seen in Figure 4.6.

To understand a LEED IV measurement, the types of scattering interactions must be considered. Of primary interest are beams of elastically scattered electrons. Obviously only backscattered electrons can be measured; forward scattered electrons will be lost in the sample. Other inelastic scattering events can occur, where electrons will lose energy to lattice phonons, surface plasmons, or undergo more complicated multi-electron scattering to produce secondary electrons. Low energy electrons are deflected away from the screen by the display grids, so that only high energy, singly-scattered electrons will be imaged.

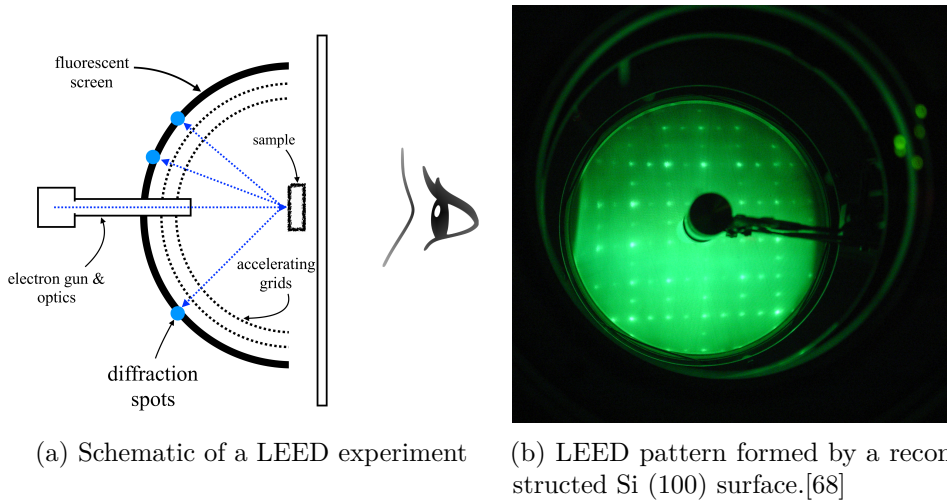


Figure 4.6: Low energy electrons are scattered off a sample surface (left). Constructive interference from the backscatter forms diffraction spots on a fluorescent grid. The resulting pattern is observed through a window and can be quickly used to identify surface reconstructions (right).

Similar to X-ray scattering, the backscattered electron beams can be understood to constructively interfere when they satisfy the Laue condition:

$$\vec{k} - \vec{k}_0 = \vec{G}_{hkl} \quad (4.11)$$

where \vec{k} is the wave vector of the scattered beam, \vec{k}_0 is the incoming beam, and \vec{G}_{hkl} is a reciprocal lattice vector with integer indices h, k, ℓ . Selecting for elastically scattered electrons, $|\vec{k}| = |\vec{k}_0|$. Since electrons at low energies have a low penetration depth, on the order of 6\AA , we do not consider the ℓ component of \vec{G} , and instead consider the 2D condition:

$$\vec{k}^{\parallel} - \vec{k}_0^{\parallel} = \vec{g}_{hk} = h\vec{a}^* + k\vec{b}^* \quad (4.12)$$

where the \parallel superscript indicates a vector component parallel to the surface, and \vec{a}^* and \vec{b}^* are 2D reciprocal space vectors.

Since at the surface of a material there is typically a relaxation of the bulk structure, LEED measures a *superstructure* of this relaxed surface as well as the more bulk-like substrate beneath. The resulting pattern will have bright spots corresponding to the substrate layer and dimmer spots in-between, corresponding to the surface layer. The surface spots are spaced closer together since the surface layer usually has larger real space dimensions (and hence shorter reciprocal space dimensions).

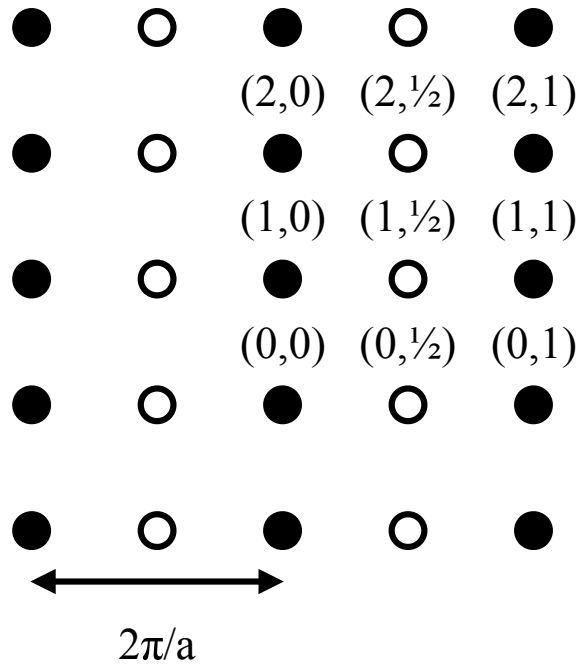


Figure 4.7: Labelling scheme for the (100) face of a simple cubic lattice with a (2×1) superstructure with the same symmetry. Open circles are the extra spots associated with the surface structure, and would appear dimmer in LEED.

We can therefore begin to label spots of a LEED pattern using the integer indices h and k . The direct reflection spot $(0,0)$ is blocked by the electron beam source, with higher order spots radiating outward from the centre of the image, as depicted in Figure 4.7. In the case of a superstructure, the brighter spots are given integer labels, with the dim spots fractional labels depending on their spacing. For simple superstructures with commensurate symmetry to the substrate, Wood's notation is used to label the pattern, based on the spacing of bright spots and any rotation necessary to overlay the two patterns in the superstructure (typically 45° or 30°).

4.3.1 LEED-IV

While visual inspection of a LEED image allows some cursory information about a surface reconstruction, for example its 2D symmetry and periodicity versus the bulk, more quantitative analysis is required to extract a structure from the LEED diffraction pattern. In this case, intensity measurements of individual spots can be performed with a spot photometer, Faraday cup or CCD camera. By measuring spot intensity (I) over a range of bias voltages (V) more information can be extracted in a so-called LEED IV measurement. Some LEED IV curves can be seen in Figure 5.12.

A full discussion of simulating a LEED IV curve is beyond the scope of this work, but

can be found discussed in Ref [67] and [69]. Briefly, one can think of each LEED spot being composed of contributions from multiple scattering sites (largely the atomic cores) within the surface unit cell. The intensity of each contribution will be affected by many factors, including atomic number or local structure around an atom, attenuation by depth beneath the surface, thermal vibrations and inelastic losses. As such, a search for the wave field of an individual scatterer must be made self consistently to include incoming waves from neighbouring sites. These individual fields can then be summed and their far-field behaviour compared to an experimental LEED pattern.

In order to predict a surface structure, it is therefore necessary to begin with a trial model, perform a multiple scattering simulation, compare the resulting IV curves to experiment, then update free parameters in the model and repeat until convergence. The goal is to minimize the *reliability* or *R-factor*, a fitness factor between the simulated and experimental curves. The most commonly used is the Pendry R-factor[70], given by:

$$R_p = \frac{\sum_g \int (Y_{g,theory} - Y_{g,exp})^2 dE}{\sum_g \int (Y_{g,theory}^2 + Y_{g,exp}^2) dE} \quad (4.13)$$

where the Y functions (for theory and experiment) are defined as:

$$Y_g(E) = \frac{L_g^{-1}}{L_g^{-2} + V_{oi}^2} \quad (4.14)$$

where the L_g are the logarithmic intensity ($L = I'/I$) of each of a set of Lorentzian peaks g . V_{oi} is the imaginary part of the electron self energy. This reliability is designed to be sensitive to the position of peaks, but relatively insensitive to their amplitude. However, zeros in the LEED signal also factor in, as they can be caused by important multiple scattering effects. In general, $R_p < 0.2$ is considered a good fit, $R_p \approx 0.3$ is considered a reasonable fit for surfaces containing many defects (to be discussed below), and $R_p > 0.5$ is extremely poor agreement.

Of course, generating a structural model to fit a LEED IV curve is an expensive process involving a search through a large multidimensional coordinate space. As such, it is most helpful to have an understanding of the physics of the surface in question, which can be gained from other experimental and theoretical methods.

The Subsurface Cation Vacancy Surface Reconstruction of Magnetite

5.1 Introduction

Iron oxide surfaces have been found to have a wide variety of applications, including in catalysis[71–74], spintronics[75], magnetic nanoparticles[76], biomedicine[76, 77], photocatalytic water splitting[78] and groundwater remediation[79, 80]. Many recent advancements in the study of iron oxide surfaces are compiled in the recent review of collaborator G.S. Parkinson[81]. To understand and improve upon these applications, it is important that we have a good understanding of the science of such surfaces, such as their structure and chemical behaviours. Since in DFT all properties are derived from an initial model structure, a good understanding of that structure is necessary before further properties can be explored.

One iron oxide surface of particular importance is the (001) surface of Fe_3O_4 , commonly known as magnetite. Magnetite was the first material in which magnetism was discovered, and has been used in magnetic compasses since ancient times. Its magnetism derives from the ordering of its inverse spinel structure. The spinel structure consists of a body-centred cubic anion array, with cations filling $\frac{1}{2}$ of the octahedral holes and $\frac{1}{8}$ of the tetrahedral holes. In a normal spinel the tetrahedral (*A*) and octahedral (*B*) sites are filled with cations in the $2+$ ($3d^6$) and $3+$ ($3d^5$) state, respectively. In an inverse spinel, this is reversed. The *A* sites in magnetite have tetrahedrally coordinated Fe^{3+} cations, while in the octahedrally coordinated *B* sites Fe have an average occupation of $\text{Fe}^{2.5+}$, as shown in Figure 5.1. In the [001] direction, magnetite can be modelled as alternating layers of $(\text{Fe}_2)^{6+}$ (the *A*-layer) and $(\text{Fe}_4\text{O}_8)^{6-}$ (the *B*-layer). The spins of the two layers oppose

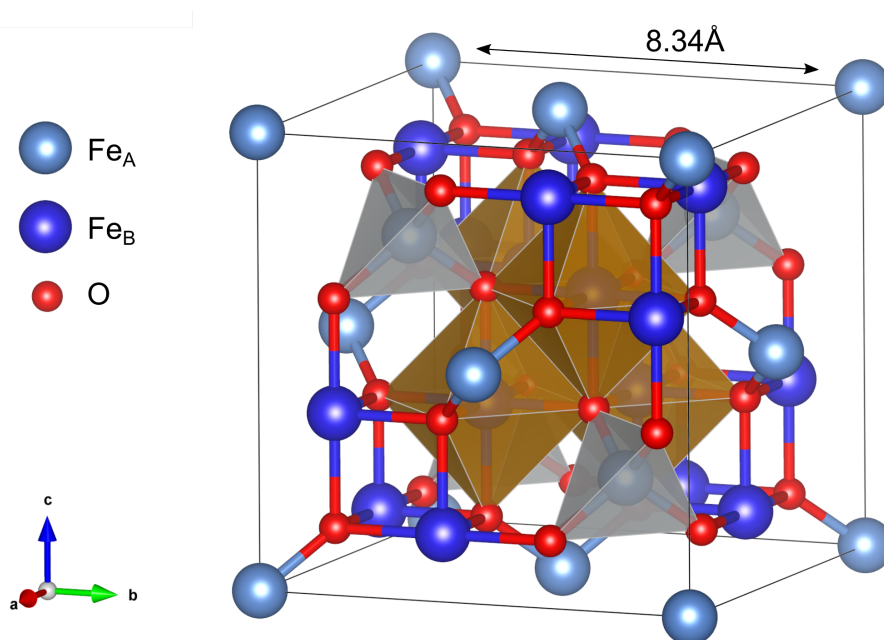


Figure 5.1: Structure of bulk magnetite. Tetrahedral Fe_A and octahedral Fe_B occupy a body-centred cubic O lattice in anti-ferromagnetically coupled layers.

each other, leading to a bulk ferrimagnetic ordering that gives the overall magnetic structure of the material.

While magnetite is a half-metal at room temperature, it undergoes a first-order metal-insulator transition at its Verwey temperature, about 125 K[82]. Below the Verwey temperature the conductivity of magnetite decreases by two orders of magnitude. This transition occurs due to a charge ordering of the B-layer Fe^{2.5+} into localized Fe²⁺ and Fe³⁺ at low temperature, in addition to a distortion of the cubic inverse spinel structure into a large monoclinic cell[83]. However, the exact nature of the charge ordering below the Verwey transition is still disputed, with charge disproportionation between neighbouring Fe_B shown to be less than 0.5 e⁻[84]. For the purposes of this chapter Fe_B sites will be discussed as if they have a formal oxidation state of either 2+ or 3+ in order to distinguish them, as they become inequivalent in DFT calculations. There has been recent work in attempting to induce the Verwey transition in strained magnetite through an applied voltage to create a "Mottronic" switch[85].

5.2 Previous Understanding of the (001) Surface

Magnetite has a well understood crystal structure, and its surfaces have been studied extensively in the literature. DFT studies have shown that the (001) surface is the most energetically favourable surface, dominating the Wulff construction of a Fe₃O₄

particle[86]. The (111) and (011) surfaces are both less favourable than (001), though their respective energy penalty is disputed[87]. Experimental studies of magnetite clearly show that the (001) surface of annealed samples will form a $(\sqrt{2}\times\sqrt{2})R45^\circ$ reconstruction; this is common enough to be taken as an indication of a clean surface[88, 89]. This reconstruction is easily confirmed with LEED, as shown in Figure 5.2.

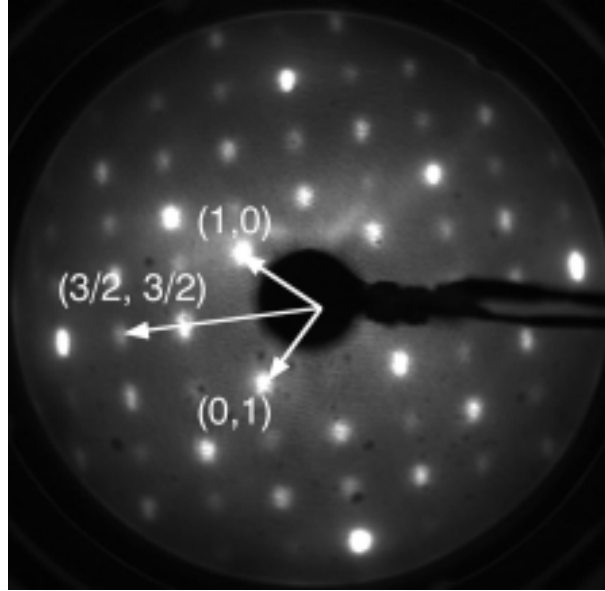


Figure 5.2: $(\sqrt{2}\times\sqrt{2})R45^\circ$ LEED pattern on an annealed Fe_3O_4 (001) surface, $E=95$ eV. Reprinted from Ref. [89] with permission from Elsevier.

Annealed (001) surfaces were understood to terminate at the B-layer based on STM studies such as Ref [89]. The surface consists of Fe_B rows separated by 6 \AA that rotate by 90° between surface layers with step height of 2.1 \AA . The rows travel along the $[110]$ and $[\bar{1}10]$ directions, consistent with Fe_B positions in the bulk unit cell. Collectively the rows adopt a wavy pattern, with the spacing between rows alternating between narrow and wide sites (to be expanded on below). A sample STM image is presented in Figure 5.3.

As mentioned in Section 5.1, in the $[001]$ direction magnetite is a layered material, with each plane possessing a net charge of $\pm 6 e^-$. As discussed in Section 3.0.7, such a layering must be terminated by a surface with net charge of $\pm 3 e^-$ to prevent a polar catastrophe and subsequent surface faceting. Two simple terminations would satisfy this polar criteria:

- A half-monolayer termination of Fe_A^{3+} in the bulk-continuing tetrahedral site. However, this termination is inconsistent with STM experiments that show a largely flat surface without protrusions.
- One oxygen vacancy per $(\sqrt{2}\times\sqrt{2})$ unit cell, plus an oxidation state change of either one Fe_B^{2+} or two $\text{Fe}_B^{2.5+}$ to a $3+$ state[89]. However, such a reconstruction

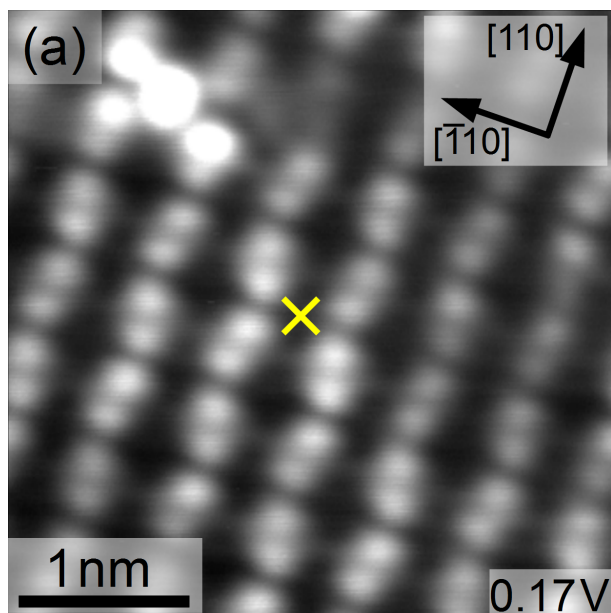


Figure 5.3: High resolution image of the magnetite surface (001). At low bias (here $V=0.17\text{ V}$), individual Fe_B sites can be distinguished. The wavy pattern alternates between rows, giving a $(\sqrt{2}\times\sqrt{2})$ unit cell. The \times indicates the site of selective adatom adsorption in the reconstruction. From Ref [90]. Reprinted with permission from AAAS.

would strongly promote dissociative water adsorption at the surface, and this is not observed [91, 92].

With neither simple alternative to B-layer termination being consistent with experiment, a consensus built around the reconstruction being some sort of distorted B-layer.

5.2.1 Distorted B-layer Termination

As mentioned above, polarity arguments prohibit a simple (1×1) B-layer termination, as depicted in Figure 5.4. It is therefore necessary for some combination of structural or electronic relaxation to occur. Such models were proposed by Pentcheva and Łodziana on the basis of PBE and PBE+U calculations, respectively[93, 94].

The Pentcheva model described a 9-layered Fe_3O_4 slab undergoing a Jahn-Teller distortion at the surface, leading to the $(\sqrt{2}\times\sqrt{2})$ reconstruction and a wavy pattern in the surface B-layer, in qualitative agreement with the STM measurements. Polarity compensation seems to be achieved by a migration of charge away from the surface, leading to a substantial quenching of the magnetic moment of surface Fe_B sites ($3.00\ \mu_B$) as compared to bulk Fe_A tetrahedral ($3.43\ \mu_B$) and Fe_B octahedral ($3.50\ \mu_B$) sites. They additionally observe a magnetic moment of $0.25\ \mu_B$ to surface O sites without a sub-surface Fe_A neighbour. Additionally, Pentcheva makes use of a surface phase diagram to demonstrate

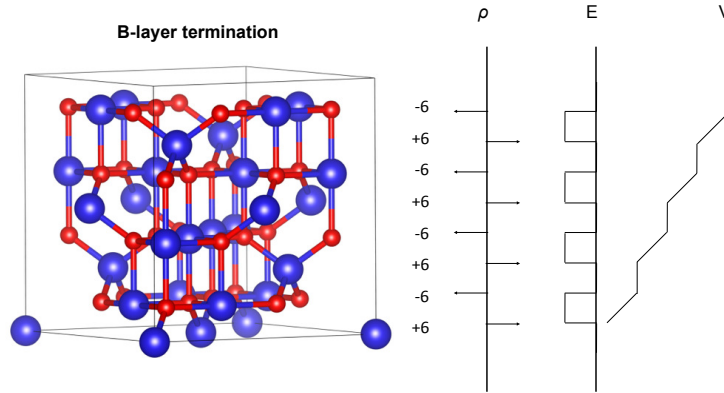


Figure 5.4: Depiction of the polar catastrophe of an un-reconstructed B-layer termination. The divergent surface energy will force the surface to reconstruct.

that this distorted B-layer termination (DBT) has lower surface energy than a variety of other surface terminations, including the two simple terminations mentioned above, as well as unrelaxed A and B-layer terminations and a half-monolayer Fe_A put in-plane with the terminal B-layer. This model was later compared to LEED IV experiments, resulting in an overall fit of $R_p = 0.34$. The low level of agreement was attributed to the inclusion of defects, domain boundaries and surface roughness in the measured sample, as well as being in line with other oxide surfaces.

The DBT model was improved by Łodziana by the inclusion of a Hubbard-U correction ($U = 4.5 \text{ eV}$, $J = 0.89 \text{ eV}$) and an increase to a 15-layer slab. The inclusion of the Hubbard-U produced more realistic moments of $4.10 \mu_B$ and $3.90 \mu_B$ on the two inequivalent surface Fe_B sites, as compared to the bulk Fe_B moment of $3.90 \mu_B$ and Fe_A moment of $3.95 \mu_B$. In addition, Łodziana notices a band gap of 0.3 eV opening and a charge ordering in the subsurface iron layers, likening the effect to a Verwey transition happening at the surface. Scanning tunnelling spectroscopy studies also observe a gap of $\sim 0.2 \text{ eV}$ at room temperature[95], and spin polarizations at the Fermi edge of less than 100% is noted experimentally (see Section 5.8). However, the DBT structure does not sufficiently displace the surface Fe_B sites to account for the experimental behaviour of adatoms, as will be discussed below.

5.3 Adatoms on the (100) surface

The magnetite (100) surface has been shown to stabilize single adatoms of Au (as shown in Figure 5.5), Ag and Pd, making it an excellent model substrate with which to

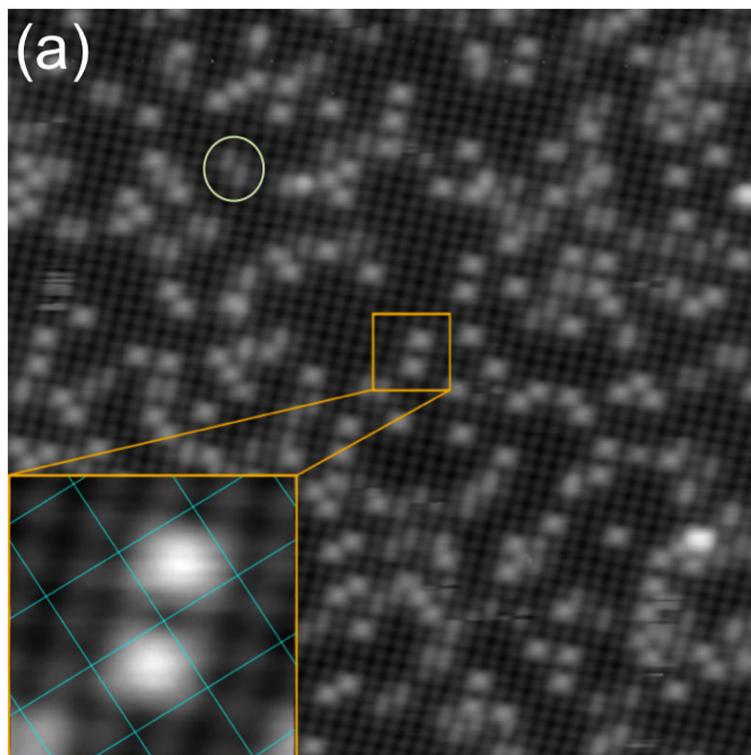


Figure 5.5: STM image ($300 \times 300 \text{ \AA}^2$, $V = +1 \text{ V}$) of 0.12 ML Au deposited on Fe_3O_4 at room temperature. The inset shows two adatoms occupying neighbouring $(\sqrt{2} \times \sqrt{2})$ unit cells. Reprinted figure with permission from Ref [96]. Copyright 2012 by the American Physical Society.

understand catalysis reactions using these metals[96, 97]. The adatoms are stable against agglomeration up to temperatures of 700 K, indicating a strong binding reaction with the surface. Interestingly, after being deposited, these adatoms are found to occupy only one of two bulk-continuation sites in the $(\sqrt{2} \times \sqrt{2})$ unit cell, as seen in the Figure 5.5 inset.

This selective adsorption posed a challenge to the DBT surface model. Even with subsurface charge ordering, the distortion of the surface layer was too subtle to impact the geometry of the bulk-continuation sites. In the DBT model used in this work, the neighbouring oxygens that bound these two sites are 3.386 \AA and 3.460 \AA apart; adsorbing atoms in these sites would see a difference in bond length on the order of 0.04 \AA . Indeed, DFT+U calculations for Au adsorbates show a nearly identical adsorption energy for both sites. While it is shown that occupation of both sites in a single unit cell is unstable[98], this does not explain why site selectivity can occur at low adatom coverages such as the 0.12 ML coverage imaged in Figure 5.5.

A clue to resolve this issue came about when adsorbed Co on the magnetite (001) surface was found to incorporate into the surface at room temperature[99]. Sequences of STM

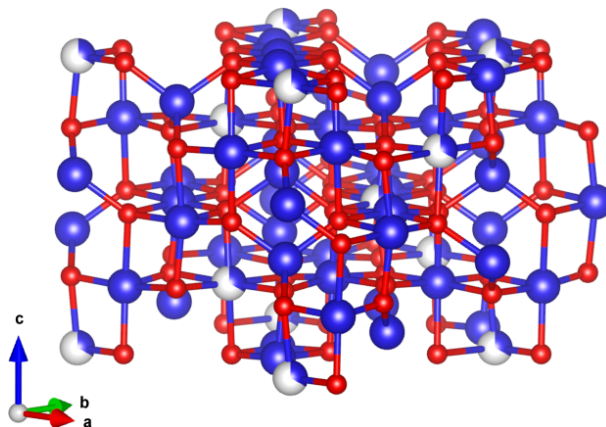


Figure 5.6: Structure of the magnetite-like maghemite, $\gamma\text{-Fe}_2\text{O}_3$. The maghemite structure is characterised by a random distribution of octahedral Fe_B vacancies, depicted here as un-filled blue spheres.

images clearly show a Co adatom transforming into a bright feature in line with a row of surface Fe_B s. In addition, sufficient incorporation of adatoms in this way causes the $(\sqrt{2} \times \sqrt{2})$ surface reconstruction to lift, and a (1×1) LEED pattern to emerge. Since the surface Fe_B s remain visible after incorporation, it seemed that the Co was being incorporated into sub-surface vacancies. These vacancies both exist in sufficient quantity to adsorb 1 Co adatom per $(\sqrt{2} \times \sqrt{2})$ unit cell, and seemed to control the unit cell reconstruction itself. Since the subsurface could not be directly observed with STM, other experimental and theoretical techniques were required to investigate this phenomenon.

5.4 SCV termination

Magnetite itself is a metastable form of iron oxide, forming at oxygen potentials between that of Fe_2O_3 (hematite), the most thermodynamically stable form, and FeO (wüstite), which forms under the most oxidizing conditions[100]. It therefore makes sense to consider surface reconstructions that are non-stoichiometric. In metal oxides surfaces this consideration is usually made by considering oxygen vacancies (V_O s). This choice is natural, as on any oxide surface under standard atmosphere, oxygen can be assumed to be the more mobile, reactive species[101].

Of interest in considering the problems of the magnetite surface reconstruction is the structure of $\gamma\text{-Fe}_2\text{O}_3$, maghemite. Maghemite possesses the same inverse-spinel structure as magnetite, but contains a distribution of octahedral Fe vacancies, as depicted in Figure 5.6 in the cubic approximation. The existence of B vacancies in magnetite are shown to be preferred under a previous DFT+U study[102], and are stabilized by a relaxation of nearby Fe cations towards the vacancy and O away from it. Further, the existence of a bulk phase demonstrates the underlying stability of the O-lattice in its body-centred cubic sub-lattice structure, which remains intact until after all Fe^{2+} is removed[103].

One additional property of magnetite is that it appears to be a fairly good conductor of Fe ions, at least in the vicinity of the surface. Most notably, when annealing magnetite in O_2 at elevated temperature, hundreds of virgin (001) layers are formed, requiring Fe be supplied from the crystal bulk[104]. Therefore, if magnetite conducts Fe easily and its inverse spinel structure can stabilize a large fraction of octahedral Fe_B vacancies, and the (001) surface can incorporate Co into subsurface layers at room temperature, it seems feasible that the $(\sqrt{2}\times\sqrt{2})$ reconstruction includes subsurface octahedral Fe cation vacancies (SCV) with long-range crystalline order.

To create an initial model it became necessary to consider migrating two Fe_B out of the sub-surface B-layer (hereafter labelled the (S-2) layer). Two vacancies were necessary to maintain mirror symmetry in the $(\sqrt{2}\times\sqrt{2})$ cell; as seen in Figure 5.3 the surface rows appear to be mirror images of each other in STM. It seemed unreasonable that the surface stoichiometry would shift to such a large degree, with the surface unit cell going from a bulk-like stoichiometry of $Fe_{12}O_{16}\rightarrow Fe_{10}O_{16}$. Instead, it was hypothesized that one of the two subsurface Fe_B s moved into an interstitial position in the (S-1) A-layer to block one of the two bulk continuation sites. The other Fe_B would meanwhile migrate away into the bulk, or at least far enough from the surface that it would not affect its long-range periodicity. This would lead to a smaller stoichiometry change ($Fe_{11}O_{16}$) and reconcile the structural model with the two problematic adsorption phenomena.

Having formed a hypothetical model of the $(\sqrt{2}\times\sqrt{2})$ surface reconstruction, it was then necessary to go about testing it. It was decided that the model would be tested theoretically by comparing it with the DBT reconstruction through a surface phase diagram. Additionally the model would be tested experimentally using LEED IV as surface sensitive test of structure. These methods are described below.

5.5 Theoretical Techniques

5.5.1 Unit cell expansion due to Hubbard U

The ferrimagnetic behaviour of magnetite, along with the disordered filling of the octahedral $Fe^{2.5}$ sites causes a distortion of its structure from that of an ideal inverse spinel[105]. This magnetic coupling causes a slight contraction of Fe_A-O and lengthening of Fe_B-O bonds. Conversely, external factors that would change bond lengths in the material, such as pressure and temperature, will therefore be coupled to the magnetic state. Below the Verwey temperature, the charge ordering of the Fe_B sites increases the distortion sufficiently that magnetite undergoes a phase change from the $Fd\bar{3}m$ space group to a monoclinic structure[106]. Since our adsorption experiments are performed above the Verwey temperature, it was decided to use the simpler cubic structure of magnetite as the basis for slab models its surface. The SCV model turns out to be consistent above and below the Verwey transition.

Due to the role of magnetism in driving the magnetite structure, an important consideration arises: if we will use a Hubbard U to approximate the correlation of Fe $3d$ electrons,

what effect will this have on the structure? In principle we expect a systematic error in Fe–O bond lengths, leading to an expansion or contraction of simulated bulk or slab models. As a first approximation, this could be modelled as a hydrostatic pressure applied to each unit cell, depending on U . Practically this would change the unit cell volume while maintaining a constant ratio of cell dimensions a, b and c . This approximation will not be ideal in the case of a slab model, as d electrons at the surface discontinuity will be affected differently by this change in cell volume (and any surface lift-off). However this volume correction turns out to be appropriate, as will be discussed in Sections 5.6.1.

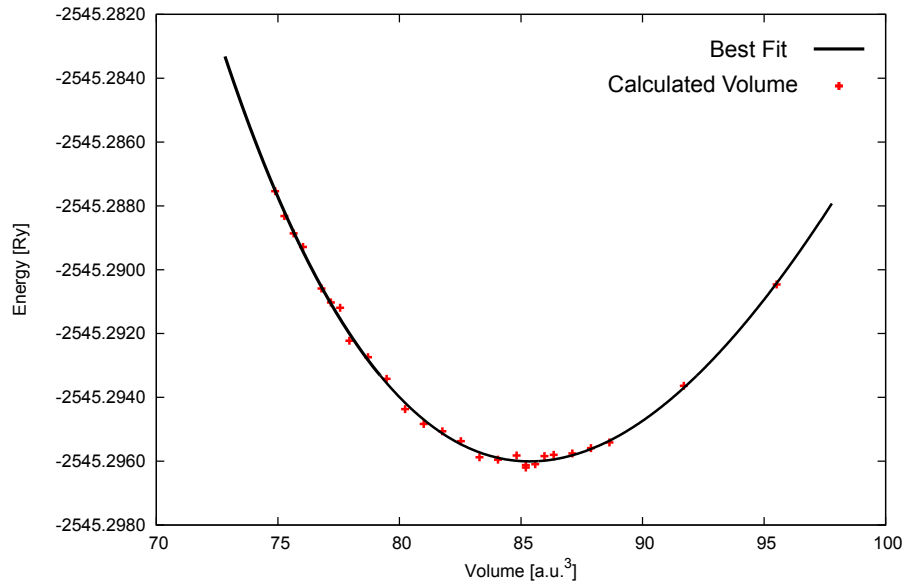
To determine the required volume correction on Fe with $U = 3.8$ eV applied to $3d$ electrons, volume optimization was carried out using the tools provided in WIEN2k on both bulk cubic Fe_3O_4 (in a 17-layer structure for later re-use of the calculation) and FCC Fe. A volume expansion step size of 0.5% was used, and the total energy at each step compared. The results of this optimization are shown in Figure 5.7. The application of $U = 3.8$ eV resulted in an 11.5% expansion in the unit cell volume of FCC Fe and a 3.5% expansion in cubic Fe_3O_4 . These expansion ratios were used in subsequent calculations of Fe_3O_4 surface slabs and in constructing the surface phase diagram.

5.5.2 DFT Relaxation of the SCV Model Structure

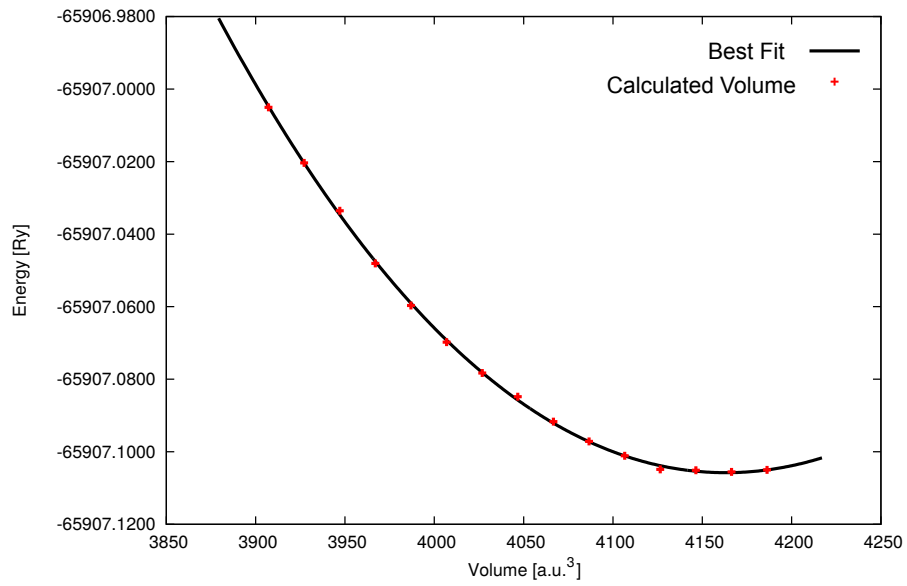
To find relaxed positions of the SCV structure, a slab model was constructed. To maintain inversion symmetry in the bi-layered magnetite structure, a slab must be $4n + 1$ layers thick for integer n . One layer serves as the central B-layer, with n A-B units layered "above" and "below" it. Previous calculations in our group had found that magnetic moments were not realistic and charge-ordering was not recovered in the centre of a 13-layer ($n = 3$) slab, so relaxation was performed on a 17-layer ($n = 4$) slab with $30 a_0$ of vacuum separating its two B-layer surfaces. Validation of the convergence of the structure was performed on a 25-layer ($n = 6$) model. If we consider the surface-most 4 layers on each side of a slab as the reconstructed portion, a 13, 17 and 25 layer slab would therefore have 5, 9 and 17 "bulk-like" layers, respectively.

Once the 17-layer model was constructed, it was relaxed with WIEN2k's MSR1a mixer, which simultaneously updates atomic positions along with orbital coefficients during the SCF cycle[107]. Atomic sphere size R_{MT} of 1.86 bohr and 1.5 bohr were used for Fe and O, respectively. Over the course of the relaxation the O sphere size had to be reduced to 1.15 bohr to avoid atomic sphere collisions, both in the SCV model and in a molecular O_2 model used to calculate the enthalpy of formation. Relaxation was performed with a $2 \times 2 \times 1$ k -mesh (the cell's c axis was interrupted by vacuum). An initial RK_{max} of 5 was used, then increased to 5.5 after an initial convergence for fine adjustment of atomic positions. An anti-ferromagnetic spin configuration was used as the starting point for relaxation, however a subsequent test showed that anti-ferromagnetic ordering was recovered from a non-magnetic initial state.

The SCV model was successfully relaxed, with the resulting structure shown in Figure 5.8. Several comments can be immediately made on the basis of the structure:



(a) Volume optimization of FCC Fe. $R_{MT} = 1.86$, $RK_{max} = 6.4$, k-mesh $21 \times 21 \times 21$, $U = 3.8$ eV



(b) Volume optimization of a cubic, 17 layer Fe_3O_4 structure. $R_{MT}^{Fe} = 1.86$, $R_{MT}^O = 1.60$, $RK_{max} = 5.5$, k-mesh $6 \times 6 \times 2$, $U = 3.8$ eV

Figure 5.7: Unit cell volume optimizations for $U = 3.8$ eV

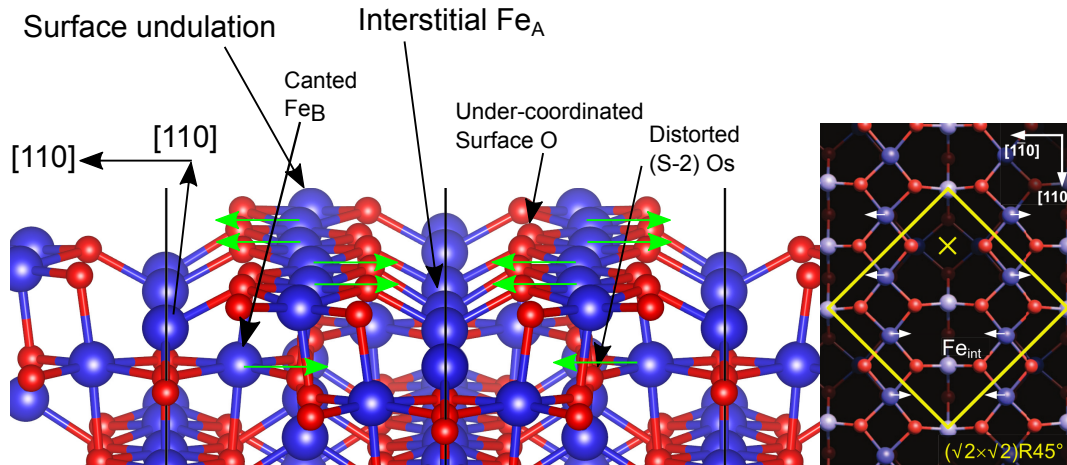


Figure 5.8: Relaxed SCV structure on the surface of a 17-layer slab (left). Undulation of the surface Fe_B layers becomes pronounced, and the interstitial Fe_A sits in the "narrow" site between Fe_B rows. The "wide" site is bounded by under-coordinated Os that sit slightly relaxed towards the bulk. Viewed from above (right), the selective adsorption site is marked with a ×.

- The undulation of the surface Fe_B layers is pronounced as compared to the DBT structure. In our relaxed DBT structure, surface Fe_Bs are at most 6.073 Å and at minimum 5.933 Å apart, an undulation of only 0.14 Å. In the SCV model it is 3.5× greater, increasing to 0.49 Å, with the wide site and narrow site 6.249 Å and 5.758 Å apart, respectively.
- The interstitial Fe_A placed into the (S-1) row stays in the layer with its neighbours, only relaxing 0.0915 Å down towards the bulk. The adjacent surface layer Fe_Bs relax towards it in the $[\bar{1}10]$ direction, while its neighbouring Fe_As relax slightly away from it in $[110]$.
- The under-coordinated surface layer O (i.e. the ones not bonded to an (S-1) Fe_A) relax slightly into the surface, about 0.15 Å lower than the other surface Os.
- There is a waviness in the (S-2) O rows that opposes the waviness in the surface Fe_B rows that they are beneath. While in the bulk these Os are in a tetrahedral coordination, in the SCV the Os are adjacent to a Fe_B vacancy are closer to a strained trigonal coordination.
- The remaining Fe_Bs in the (S-2) layer form canted octahedra, as they connect bulk-like O positions in the (S-4) layer with the under-coordinated O on the surface. They relax towards the interstitial Fe_A beside them in the neighbouring row.

5.5.3 Surface Phase Diagram - SCV versus DBT

Using a similarly relaxed DBT structure, using the same calculation parameters (U , RK_{max} , R_{MT} sphere sizes, k -mesh, etc), it is then possible to construct a surface phase diagram as described in Section 3.1. The result, shown in Figure 5.9, shows that the SCV surface has lower energy than the DBT surface for all oxygen potential μ_O accessible under the UHV preparation conditions, and is only higher energy at extremely reducing (low μ_O) conditions. Since the SCV structure was published, collaborators have calculated several other surface reconstructions described by Pentcheva as higher energy than the DBT structure, including some modified SCV structures with additional surface Fe_A ; all have higher surface energy than the SCV structure (see Figure 28 in ref [81]).

This theoretical result was very positive, as it showed that the assumptions that were made about the SCV structure were reasonable. In addition, the structure was stable under adsorption of Au, which binds strongly (2.03 eV) in a position above and between the under-coordinated Os in the "wide" site[90]; adsorption in the "narrow" site was not possible due to the blocking interstitial Fe_A in the (S-1) row. However, while the structure seemed physically reasonable, it was built on indirect evidence from adsorption experiments, and actually contradicts a detail of the site-selective adsorption phenomenon. It had been assumed that adatoms would be favourable in the "narrow" position between the Fe_B rows (the position of the \times in Figure 5.3), but the SCV model showed adsorption was only possible in the "wide" site!

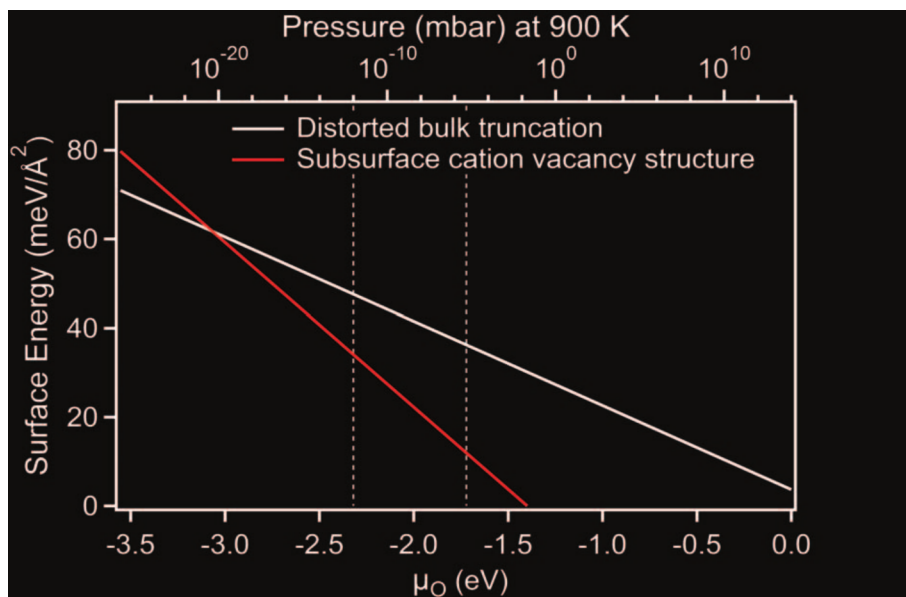


Figure 5.9: Surface phase diagram comparing the SCV and DBT structures over two extremes of μ_O : rejection of O from the bulk (low μ_O) to spontaneous formation of O_2 on the surface (high μ_O). From Ref [90]. Reprinted with permission from AAAS.

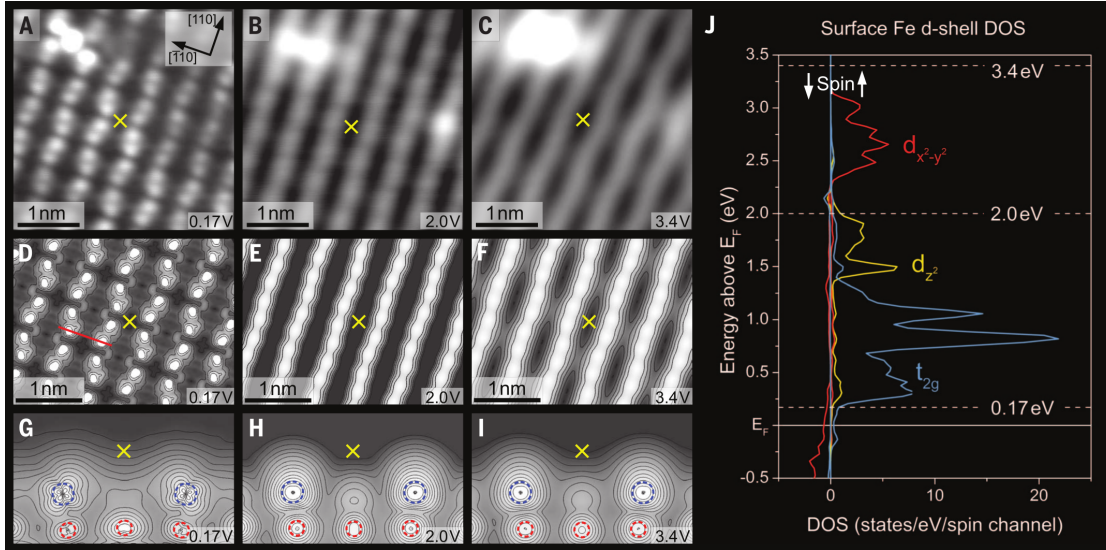


Figure 5.10: The appearance of row undulations on the SCV surface are strongly controlled by STM bias. Experimental STM images (A-C) were obtained at the same position (in comparison to the Fe adatom in the top-left). As the bias voltage was increased the apparent phase of the surface undulations shift, with the preferred adatom adsorption site (marked with an \times) going from "narrow" to "wide". This can be understood as a purely electronic effect, as seen in simulated STM images (D-F). By looking at an adsorption site in cross section (G-I, showing the path marked by a red line in D), it is clear that t_{2g} orbitals on the surface Fe_B atoms (blue dashed circles) are tilted towards the adsorption site. As shown in J, t_{2g} orbitals contribute at energies just above E_F , and are consequently imaged at low bias. As bias increases, the spherically symmetric d_z^2 and $d_{x^2-y^2}$ begin to dominate the STM image, and the true underlying row structure is revealed. From Ref [90]. Reprinted with permission from AAAS.

5.5.4 Simulated STM of the SCV Surface

To resolve the adsorption site discrepancy, it was necessary to consider that STM measures the electron density of a surface. While at long range the electron density around surface atoms are roughly spherically symmetric, for very high resolution measurements it becomes important to consider the exact shape of the orbitals being imaged. In the case of the magnetite surface, Fe $3d$ states dominate the valence band maximum and conduction band minimum. In particular, the empty states closest to the Fermi level are non-spherically symmetric t_{2g} orbitals (the $3d_{xy}$, $3d_{xz}$ and $3d_{yz}$ orbitals), as shown in Figure 5.10J. By simulating STM measurements at various biases above the Fermi level (Fig 5.10D-F), higher energy orbitals with e_g symmetry could be included, which turn out to be more spherically symmetric around the surface Fe_B sites.

Going from low to high bias, the density around the preferred adsorption site (i.e. the site between under-coordinated Os) goes from being pointed towards the centre of the site

(making it appear narrow) to pointing out of the surface plane (making it appear wide), as shown in Fig 5.10G-I. At low bias the surface Fe_B 's t_{2g} orbitals appear to be turned towards the centre of the row in order to remain antibonding with the neighbouring O atom in the (S-2) site below. This O is in a strained position due to an adjacent cation vacancy (as mentioned above), giving it an out-of-plane empty $2p$ orbital in the vicinity of the Fermi level. At higher energy both the surface Fe_B and the (S-2) O adopt more spherical empty state distributions, making the site appear wide, in agreement with the position of the surface Fe_B nuclei.

The simulated STM are in good agreement with STM images collected at the same bias voltages (Fig 5.10A-C, described in Section 5.6) and aligned through the use of a landmark (a Fe_A adsorbate). It can be seen that the narrow position of the wavy rows at low bias (marked with a \times) becomes difficult to distinguish, as the rows become apparently straight at 2.0 eV bias, as $3d_{z^2}$ orbitals become accessible. At 3.4 eV the rows again become wavy, but in the opposite phase. The adsorption site now appears wide, in agreement with the positions of the Fe_B atoms that bound it. The agreement of this peculiar feature of the SCV's electronic structure with experiment provided another sign that the model is an improvement on the DBT structure.

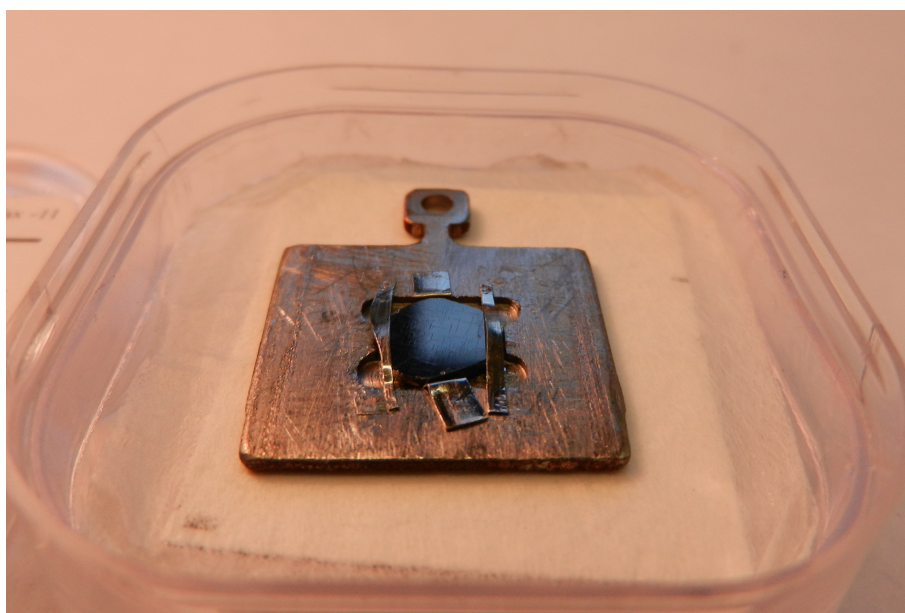


Figure 5.11: Photo of a crystalline magnetite sample mounted on a conducting sample plate. Courtesy of Roland Bliem.

5.6 Experimental Techniques

Unless noted otherwise, experiments for this chapter were performed on a synthetic crystal grown using the floating zone method, provided by Z. Mao and P. J. Liu (Tulane

University)). A mounted sample is depicted in Figure 5.11. The magnetite surface ($\sqrt{2}\times\sqrt{2}$)R45° reconstruction was prepared in the STM setup by sputtering with Ar^+ ions ($I_{\text{sample}} = 1 \mu\text{A}$ for 15 min) followed by annealing in 1×10^{-6} mbar O_2 (930 K, 30 min). This was repeated for at least 4 cycles. For the LEED experiments, the sample was annealed at 920 K in 1×10^{-8} mbar O_2 , but using a doser that resulted in a ≈ 500 increase of O_2 pressure at the surface[90].

STM measurements were performed at 78 K, below the Verwey temperature. The sample was biased to measure empty states at 0.17 V, 2.0 V and 3.4 V. Due to current instability, the 0.17 V images were acquired in constant height mode; the other images were acquired in constant current mode (this distinction was considered when making simulated images for comparison).

LEED measurements were performed at 90 K by measuring spot intensities in the range 50 eV to 500 eV at normal incidence (within 0.1°) to the primary beam. All symmetrically equivalent beams were measured (where accessible), averaged together and smoothed to remove experimental noise. The resulting data set consists of 40 beams, 23 of integer order (from bulk-like diffraction) and 17 of fractional order (from the surface reconstruction). The total energy range measured was 11 308 eV.

5.6.1 Comparison of SCV with LEED IV

To provide further evidence of the SCV model, LEED IV measurements were performed and compared to a refinement model built using the same initial conditions as the DFT model (e.g. subsurface Fe_B vacancies and an interstitial Fe_A in the (S-1) layer). Refinement of this model allowed simulated LEED beam intensities to be compared to the measured intensities. The overall agreement was comparable to LEED IV measurements of clean metal surfaces, with a total R_P of 0.125. Selected beams of high agreement are shown in Figure 5.12; all beams are published in the supplemental to Ref [90].

It should be noted that the refinement of the LEED IV model was carried out independently from the DFT model relaxation and compared afterwards, giving an independent confirmation of the model. The overall agreement of the two models is excellent, with surface LEED and DFT positions being within at most 0.06 \AA of each other (Ref [90] Supplemental, Table S2). It should be noted that this comparison required rescaling of the DFT structure to experimental lattice constants (to counteract the 3.5% volume expansion added to balance the Hubbard U approximation). Since the DFT model is periodic in the c direction (normal to the surface), when rescaling in this direction there is an implicit assumption that any surface lift-off effects will be negligible, as any non-linear errors in the lift-off of simulated atoms will be reduced when the model is scaled back down. Regardless, the agreement of z coordinates between both models remains good at the surface (below $\Delta z = 0.02 \text{ \AA}$ in the surface layer).

The excellent fit of the LEED IV structure with the relaxed SCV model serves as a confirmation that this model well-describes the Fe_3O_4 ($\sqrt{2}\times\sqrt{2}$)R45° surface reconstruction. That the LEED IV model so well describes the surface demonstrates that LEED

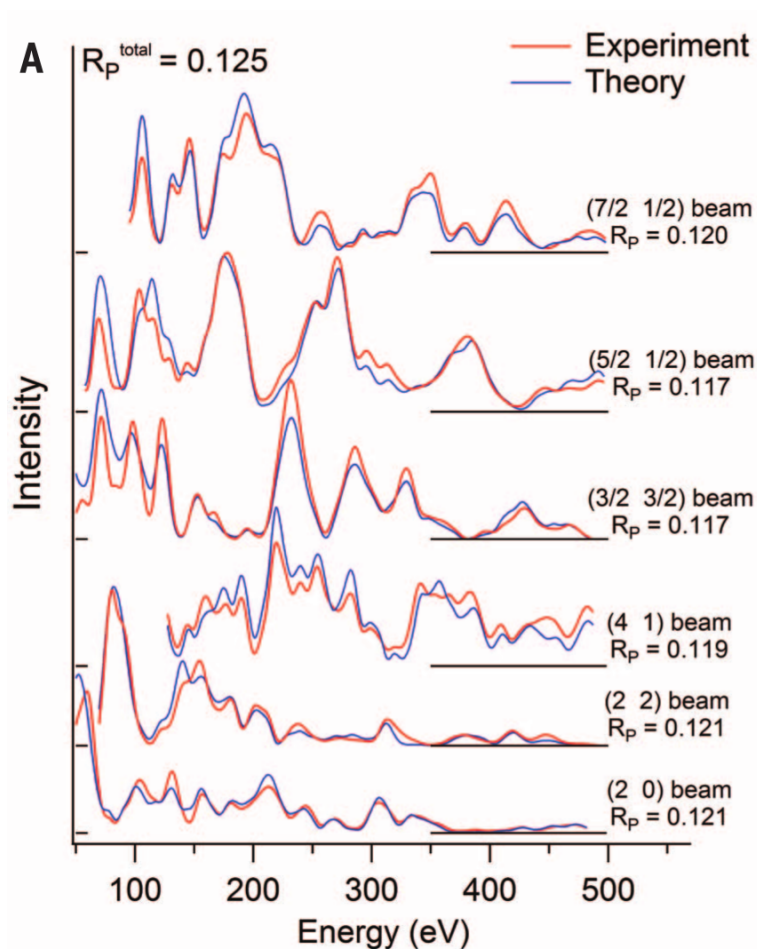


Figure 5.12: Comparison of measured and simulated LEED IV beams of an SCV reconstructed surface. All symmetrically equivalent beams are compared in the supplemental to Ref [90]. The overall agreement of all beams with the best-fit structure gives a R_P of 0.125. From Ref [90]. Reprinted with permission from AAAS.

IV is a suitable technique for experimentally modelling complex metal-oxide surfaces, not requiring any arguments about defects or oxygen vacancies. The agreement between theory and experiment is a demonstration of how accurate both these techniques are in discovering subtle relaxations in a surface layer, on a sub-angstrom level. With the SCV structure now understood, we can consider some consequences that arise from it.

5.7 Consequences of the SCV Surface Reconstruction

The primary consequence of the SCV surface reconstruction, and indeed the motivation for developing the reconstruction beyond a simple B-layer termination model, is that the surface is able to stabilize single adatoms that are resistant to agglomeration into

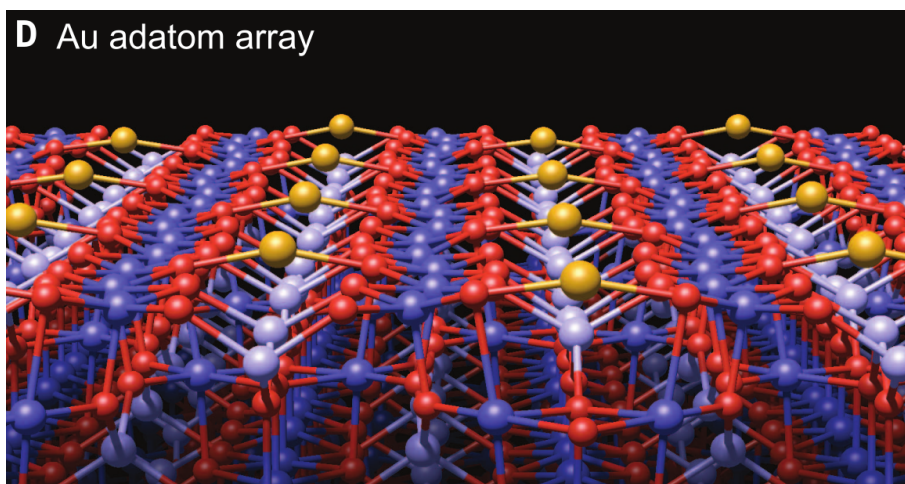


Figure 5.13: Structure of adsorbed Au on the SCV surface, with one Au per $(\sqrt{2} \times \sqrt{2})$ cell. The Au binds (2.03 eV) above the unblocked bulk-continuation site, between the two under-coordinated surface Os. From Ref [90]. Reprinted with permission from AAAS.

clusters at temperatures up to 400 °C. This is a result of one of the two bulk continuation sites per $(\sqrt{2} \times \sqrt{2})$ unit cell being blocked by the extra interstitial Fe_3^+ in the (S-1) layer. With this site blocked, the nearest neighbour distance between stable adatom adsorption sites is 8.4 Å, the periodicity of the reconstructed unit cell [96, 97]. By keeping its adatoms further apart, the tendency for metals, especially precious metals, to cluster is avoided, making the (001) surface of magnetite an ideal model substrate on which to study single-atom catalysis. The adsorption geometry is demonstrated with Au adatoms in Figure 5.13.

The presence of the vacancies in the SCV surface also leads to an unusual adsorption behaviour: the ability of a variety adsorbed adatoms to be incorporated into the surface structure and occupy subsurface vacancies after mild annealing (or even at room temperature). The controlling factor seems to be the propensity for these metal adatoms to form solid solution for Fe_3O_4 , and more specially for them to have a valence shell compatible with the octahedral cation vacancy which they migrate to. This phenomenon is discussed in detail in Ref [99] for Ti, Mn, Co, Ni and Zr.

5.7.1 Low Net Moment at the SCV Surface

The change in stoichiometry at the surface leads to a local abundance of Fe^{3+} at the surface, with exclusive Fe^{3+} -like iron in the first 4 layers. This change is seen in the DFT model as an absence of low-spin moment $\text{Fe}_{\text{B}}\text{s}$; all surface Fe has a moment of $\approx \pm 3.9 \mu_{\text{B}}$, as compared to the bulk Fe_{B} moments of either $\approx 3.6 \mu_{\text{B}}$ or $3.9 \mu_{\text{B}}$, referred to as Fe^{2+} and Fe^{3+} , respectively. This change in oxidation state population had previously been noted in surface sensitive XPS measurements, which found that the top two atomic layers of magnetite (001) had significantly less Fe^{2+} [108]. This was attributed to either a

half-layer Fe_A termination or B-layer termination with oxygen vacancies, both of which were later ruled out by DFT studies that did not take Fe^{3+} abundance into account[93].

More recently, X-ray magnetic circular dichroism (XMCD) spectra notes a net magnetic moment of the reconstructed magnetite (001) that is lower than would be expected from a stoichiometric surface termination[109]. While bulk magnetite has an experimental magnetic moment of $4.07 \mu_B$ [110], a moment of $3.48 \mu_B$ was reported for an XMCD measurement with sensitivity to the top 0.6 nm of a reconstructed sample. The effect is clearly linked to the surface reconstruction, as similar measurements performed on an *in-situ* vacuum cleaved magnetite sample result in a bulk-like moment of $3.90 \mu_B$ [111]. This reduction of spin moment is consistent with the SCV reconstruction in an anti-ferromagnetically ordered system: both the removal of a Fe_B and the flip in orientation as a Fe_B migrates to occupy the extra Fe_A position would reduce overall magnetization. The authors of this study estimated a net magnetic moment of $3.25 \mu_B$ based solely on the change in surface structure.

5.7.2 Magnetic Oxygen Sites

In addition to an increase of moment on surface Fe_B sites, the under-coordinated O sites (without a neighbouring Fe_A in the (S-1) layer) that surround the preferred adsorption site also gain a magnetic moment $\mu_O \approx 0.35 \mu_B$. This effect was also noted in the Pentcheva DBT model (with a smaller moment of $0.25 \mu_B$), and has been previously reported for the oxygen-terminated $\text{Fe}_2\text{O}_3(0001)$ surface[112].

The magnetization in the SCV model is similar to the reported μ_O of $0.36 \mu_B$ of a single FeO cluster embedded in Ar performed without a Hubbard U (but instead using the B1LYP functional[113], which incorporates exact exchange)[114]. This suggests that magnetized oxygen could simply be the result of a polarizing effect on O in the 2-oxidation state bound to Fe. However, given that the stoichiometry is moving *away* from FeO at the SCV surface ($\text{Fe}_{12}\text{O}_{16} \longrightarrow \text{Fe}_{11}\text{O}_{16}$), while Fe is simultaneously moving to a high oxidation state, in addition to under-coordination of these O and the need to terminate a layered, polar structure (discussed below), it is plausible that these sites are instead taking on a 1-oxidation state instead, with the unpaired electron resulting in magnetic moment. It is not clear that such an oxidation state is well described in DFT by examining the moment alone. For example, there is no magnetization of O in an isolated H_2O_2 molecule relaxed using PBE by this author; in this circumstance the lack of a bonded Fe does not allow any spin polarization at the O site.

The magnetization of these oxygen sites is quenched when they bond to adsorbing atoms, suggesting a further mechanism for the site-selectivity and strength of adsorption on the magnetite surface. If this is indeed an O^{1-} site it should prefer to reduce to a 2- state during adsorption. For example this is suggested in the case of a Ni adatom, which takes on a 1+ oxidation state ($\mu_{Ni} \approx 1.0 \mu_B$) when adsorbing on the surface, but has a 2+ state ($\mu_{Ni} \approx 2.0 \mu_B$) if it incorporates into the subsurface vacancy[99].

The stabilization of an O^{1-} site at a solid surface would be a further interesting phenomenon if it can be confirmed, and experimental evidence should be sought. Some indirect evidence exists in O $1s$ XPS measurements of the SCV surface (see Ref. [81] Fig 42), which shows a slight shift in the peak to lower binding energy. While it is typical that core binding energy decreases at a surface[115], the magnetic site diverges significantly from the other surface sites. The effect is similar in both a 17 and 25-layer SCV slab, with the 25-layer showing good convergence with a bulk Fe_3O_4 cell in its central layers. Regardless, its presence at the magnetite (001) surface may also explain why a supposedly polar surface termination does not facet due to the polar catastrophe.

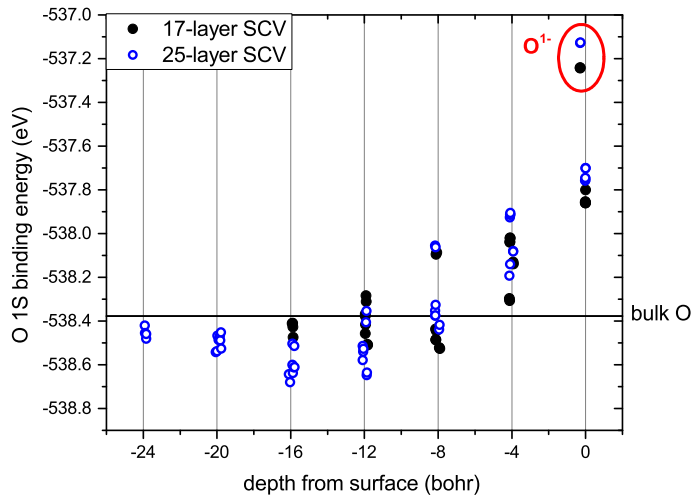


Figure 5.14: Core O $1s$ binding energies of the SCV structure as a function of depth, for both a 17 and 25-layer slab. The magnetic O^{1-} site diverges significantly from the other oxygen at the structure, suggesting a change in oxidation state that is potentially observed in XPS measurements. Final state effects are considered by including a half-core hole on bulk magnetite and surface SCV sites as described in Ref [115].

5.7.3 Surface Polarity at the SCV Surface

Given the SCV structure with all Fe in the top four layers in a 3+ oxidation state, along with the presence of high-spin oxygen sites which we assume to be in a 1- state, we are able to resolve the issue of surface polarity at a B-layer surface termination. If we considering the top four layers of the SCV reconstruction (the surface unit), one Fe has been removed to the bulk, leaving a stoichiometry of $Fe_{11}O_{16}$. Beyond this the magnetite layers are bulk-like, with alternating layers with charge of ± 6 . The layer beneath the surface is a B-layer, with charge -6, so ideally it will be capped with a layer with charge +3 as described in Section 3.0.7.

Computing the charge of the surface unit, we have $11 \times 3+ = +33$ as a positive charge on the Fe, with $16 \times 2- = -32$ on the oxygen, an overall charge of +1. However, if two of the O are instead in a 1- state, the overall charge becomes +3 as necessary (see Figure 5.15). Of course this is a simplified model; there will be additional effects due to the charge of the surface unit being spread over 4 layers rather than one, but the Tasker polarity compensation model is already a simplification. Given the LEED IV confirmation of the SCV surface, the issue of magnetite (001) having an unresolved polar surface termination is settled.

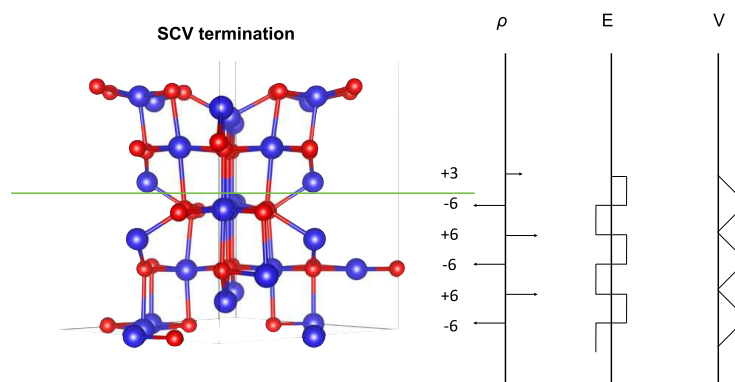


Figure 5.15: Assuming the two magnetic O sites have a -1 formal charge, the SCV surface gives a total formal charge of +3, as is necessary to prevent a polar catastrophe.

5.8 Conductivity of the SCV Surface

One desired application of magnetite is as a spintronic material. By relying on the half-metallicity of bulk Fe_3O_4 , it has been hoped that spin-polarized currents can be controlled in a practical device[116], or in the creation of magnetic sensors or nonvolatile magnetic memory. However, efforts to build such a device has been challenged by the appearance of magnetic dead layers at magnetite surfaces or interfaces[117].

The SCV surface termination gives us a lens to examine this problem. As discussed in Section 5.7.3, the change in surface stoichiometry at the SCV surface towards a more oxidized state leaves the top four layers containing only Fe^{3+} . In addition, our slab models do not recover a charge ordered B-layer in the bulk until several layers below the surface, in contrast to the case when modelling the modified B-layer termination[118]. This suggests that the SCV layer disrupts the normal conductivity mechanism in Fe_3O_4 , both by removing the availability of Fe^{2+} sites for charge hopping conductivity at the

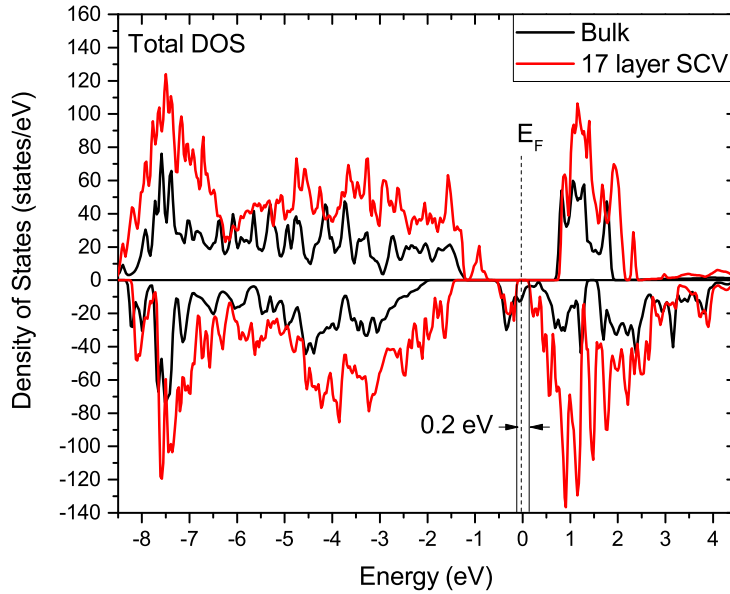


Figure 5.16: Total DOS of bulk cubic Fe_3O_4 versus the SCV reconstruction on a 17 layer slab. The bulk band crossing the Fermi level, originating from Fe_B $3d$ electrons, splits in the SCV model, creating a 0.2 eV band gap. The filled states below E_F are contributed by bulk-like $\text{Fe}_B^{2.5+}$, while the empty states just above the gap are surface Fe_B^{3+} states.

surface, and disrupting the ability of octahedral sites from taking on a Fe^{2+} character deeper into the crystal.

This argument is supported by comparing the DOS of the SCV structure with that of the bulk, as shown in Figure 5.16. In the bulk at $U = 3.8$ eV conduction occurs in electrons occupying a t_{2g} band associated with the Fe_B site which crosses the Fermi level. In the SCV structure this band disconnects, with a gap of 0.2 eV, in line with the scanning tunnelling spectroscopy study mentioned above[95]. This disconnected, filled band is still associated with the undistorted, bulk-like Fe_B sites in the centre of the SCV slab, while the surface Fe_B s contribute only to the lower filled bands.

The resulting modification to the surface DOS could also shed light on a standing issue in the understanding of spin-polarized photoemission measurements of Fe_3O_4 . Several studies making this measurement under a variety of preparation have found a range of values all less than 100% spin polarization, as would be expected from a purely half-metallic surface[119–122]. A common conclusion is that a magnetic dead layer precludes half-metallicity at the magnetite surface, with one study concluding that a dead layer approximately 1 unit cell deep would be necessary to explain their results[120].

Surface Reconstructions of Strontium Titanate (110)

6.1 Introduction

Strontium titanate (SrTiO_3 or STO) presents another complex metal oxide with interesting properties, and which is even more complex to understand than magnetite. Like magnetite, SrTiO_3 is a layered, polar material, and it is of interest as a substrate for growing thin films[123], nanoparticles[124] and depositing catalysts[125, 126]. Bulk STO forms a perovskite structure with alternating layers of $(\text{SrTiO})^{4+}$ and $(\text{O}_2)^{4-}$ in the [110] direction. As a result STO's (110) surface cannot have a stable, ordered bulk surface termination, but must reconstruct with a layer charge of ± 2 per unit cell, as described in Section 3.0.7.

STO has a number of unusual properties that are of quantum mechanical origin. For example, it is a paraelectric[127], with a reported giant piezoelectric effect at temperatures below 50 K[128] and quantum paraelectric properties below 4 K[129]. At heterostructure interfaces of SrTiO_3 and LaAlO_3 between their (001) surfaces, a highly mobile, two-dimensional electron gas forms due to polarity-negating charge transfer between materials[130, 131]. It appears that such a two-dimensional electron gas can also be formed between the SrTiO_3 (110) and its 4×1 surface reconstruction by introducing oxygen vacancies[132], demonstrating the importance of understanding the physics of such a reconstructed surface.

SrTiO_3 is also interesting as a material capable of photocatalyzing both half-reactions in the decomposition of water[133]. It was the first reported material with a better quantum efficiency than TiO_2 , the first known photocatalyst for the water-splitting reaction[134]. While the bulk band gap of STO, $E_g = 3.2$ eV, is not suitable for harvesting visible light this can be circumvented by doping (e.g. with Rh[135]) or by the deposition of co-catalysts

6. SURFACE RECONSTRUCTIONS OF STRONTIUM TITANATE (110)

on the surface, such as NiO[136]. A proper description of the surface reconstruction is important in understanding photocatalytic processes in this material, as processes such as water adsorption and carrier transfer can be affected by surface structure.

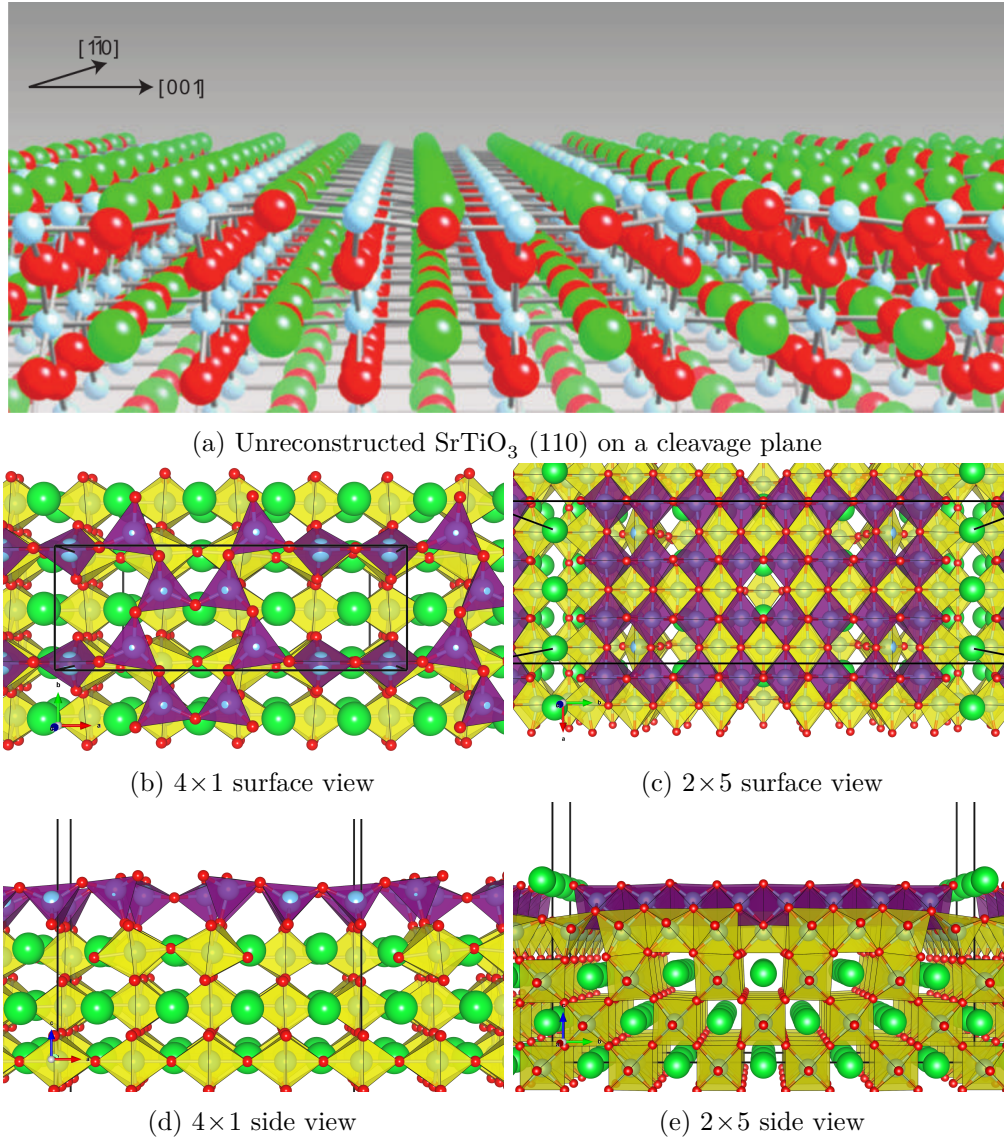


Figure 6.1: A cleaved plane of the SrTiO_3 (110) surface, as well as the surface reconstructions studied experimentally in this chapter. A smaller 2×4 unit cell with similar structure was used for the 2×5 O *K* XANES calculations (see Appendix A). Sr - green, Ti - blue, O - red. Purple polyhedra in the 4×1 reconstruction are tetrahedral, while in the 2×5 they are highly strained octahedra, as depicted in Figure 6.6. Yellow octahedra are bulk-like Ti. Fig 6.1a is reprinted by permission from Macmillan Publishers Ltd: Ref [137], copyright 2010.

6.1.1 Known reconstructions of SrTiO₃ (110)

As mentioned above, the (110) surface of STO is polar, which seems to have limited its experimental study as compared to the non-polar (001) surface until recently. LEED and STM work has demonstrated 5×2 , 2×5 , $3 \times 4/1 \times 4$, 6×6 and 4×4 reconstructions under a variety of preparation conditions[138, 139]. Additionally, faceted surface terminations have been demonstrated as another mechanism by which STO (110) can be terminated without a divergent surface energy[140].

Many surface reconstructions of STO (110) are now known to exist in an equilibrium that are interchangeable under different preparation conditions. In particular, a wide variety of $n \times 1$, $1 \times m$ and $2 \times m$ reconstructions can be selectively prepared by controlled evaporation of Sr or Ti followed by annealing under oxygen[141]. These structures have been largely solved by a combination of STM, TEM and DFT calculations[142–144].

Reconstructions of the $n \times 1$ type consist of networks of interconnected rings of six or eight corner-sharing TiO₄ units. The rings form into domains, separated and marked by coordinating surface Sr adatoms, which serve to relieve strain[145]. Higher dosing of Ti to the surface leads to a double layer of TiO_x units, which form mainly $2 \times m$ reconstructions[144]. This transition, to be discussed in further detail below, involves the addition of a strained octahedrally coordinated (*O_h*) Ti layer beneath the unusual tetrahedral (*T_d*) layer at the surface. Bulk Ti in STO occupies an octahedral site, as in TiO₂. The presence of a titania overlayer caused by surface reconstructions may help explain the photocatalytic activity of STO, by positioning the conduction band minimum at an appropriate absolute energy to facilitate the hydrogen reduction half-cell reaction.

In this work, two surface reconstructions were considered: the 4×1 and 2×5 reconstructions. The structures used for each are shown in Figure 6.1.

6.2 Experimental Considerations

XANES and XPS experiments were performed on a single crystal SrTiO₃ wafer purchased from the MTI Corporation. The sample was pre-cut to the (110) surface and mechanically polished. It was cleaned by sputtering with Ar⁺ ions, followed by annealing under ultra-high vacuum (UHV) at a pressure of 1×10^{-9} torr or better. The 4×1 and mixed 1×5 with 2×5 surface reconstructions were prepared from a clean, sputtered STO surface by vapour deposition of Ti and Sr at room temperature. This method is described in Ref [141], and from a starting surface preparation that was a mixture of 4×1 and 2×4 , approximately 1 Å of Sr was deposited. To transition to a $1/2 \times 5$ surface, approximately 1.66 Å Ti was deposited. Calibration of the deposition cycles was performed using a quartz crystal microbalance. Following each deposition cycle, the sample was annealed under oxygen at high temperature (950 °C to 1100 °C) and low pressure (approximately 2×10^{-6} torr) for up to 1 h to allow the surface reconstruction to stabilize. The desired surface reconstruction was then confirmed by LEED imaging at approximately 50 eV bias.



Figure 6.2: Sample crystal of SrTiO_3 as used in the XPS/XANES experiments, mounted on a conducting sample holder.

Measurements were made with a Scienta electron analyzer at the I311 beamline on the MAX II ring at the MAX-lab synchrotron facility. I311 uses an undulator insertion device and a plane-grating monochromator to provide plane-polarized X-rays in the range of 30 eV to 1500 eV. At photon energies around the O K and Ti $L_{2,3}$ edges the beamline achieves an energy resolution of at least 0.1 eV. Due to the high brilliance of synchrotron radiation, changes in the spectra (particularly in valence XPS) were noticed after prolonged exposure, believed to be caused by the formation of O vacancies[146]. To counteract this, the sample was periodically repositioned so that all measurements could be made on fresh spots.

Measurements were performed on the 4×1 and 2×5 surface reconstructions at both a grazing and normal angle of incidence in order to control both the path-length of the adsorbed X-rays, as well as the orbitals occupied by excited core electrons. Total electron yield (TEY) was captured by measuring the sample ground current with a nanoammeter. Auger electron yield (AEY) was measured to provide an even more surface sensitive signal using the Ti LMM and the O KLL lines. It is estimated that AEY should result in a surface sensitivity of less than 1 nm, while the TEY signal will include contributions from photoelectrons emanating from more than 2 nm beneath the surface.

6.3 Calculated Ti $L_{2,3}$ XANES

The single-particle approximation used in Density Functional Theory is reasonable when calculating K -edge X-ray absorption spectra at experimental resolutions[147]. However, the relatively small energy between $2p_{1/2}$ and $2p_{3/2}$ core levels in L -edge spectra, in combination with the coupled interaction of core-hole and conduction band electron

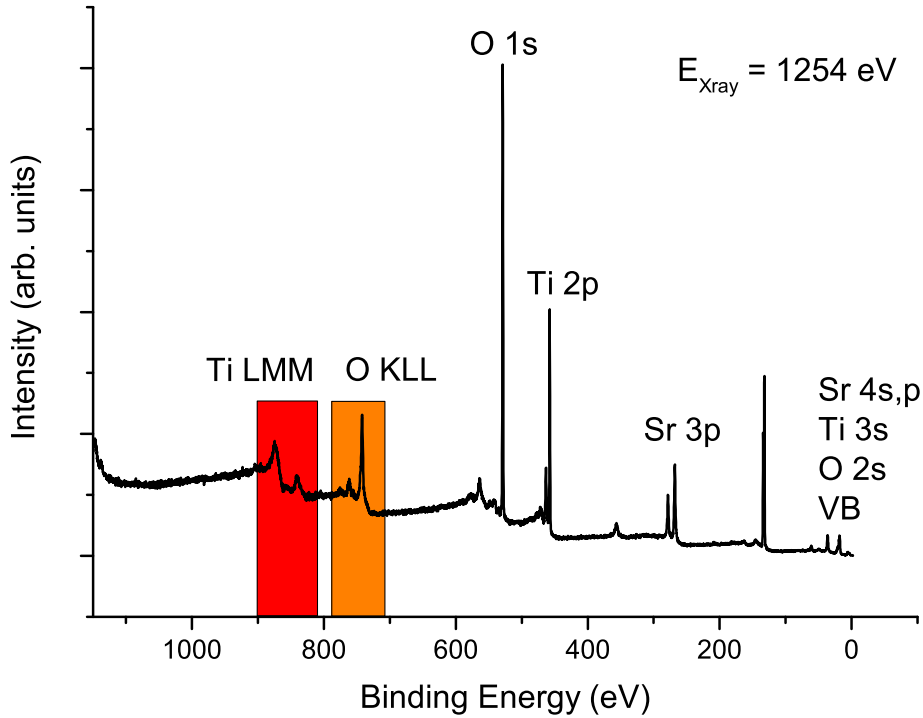


Figure 6.3: Sample XPS overview of clean SrTiO_3 (110) with a 4×1 reconstruction. Under an X-ray excitation of 1254 eV, the Ti LMM Auger lines appear as highlighted in red, while the O KLL Auger lines are highlighted in orange. The intensity of these lines are used for collecting the Auger Electron Yield measurements mentioned. Other relevant lines are labelled.

(the exciton) give rise to multiplet effects. These effects tend to dominate the spectra, which can no longer be viewed as a convolution of the conduction band DOS with some core state transition operator. While post-DFT techniques such as the Bethe-Salpeter equation (BSE) can provide good agreement with $L_{2,3}$ spectra of light elements[148], BSE is very computationally expensive and not well suited to the extended unit cells necessary to describe surface reconstructions.

Due to the apparent surface sensitivity of our Ti measurements of the $\text{STO}(110)$ surface with 4×1 and 2×5 reconstructions, it became necessary to identify an approximate method for describing the measured peak structure. The $L_{2,3}$ spectra of bulk SrTiO_3 is well understood in the framework of BSE[149], which includes only octahedrally coordinated Ti sites. Since XANES spectra are largely sensitive to the local bonding environment around an atom, an empirical calculation of point charges in the appropriate crystal field

can accurately reproduce the $L_{2,3}$ edge[150]. In such a simulation, the X-ray transition is treated as an atomic multiplet of a metal centre in a non-spherical potential (a single impurity Anderson model)[151], leading to a crystal field splitting energy $10Dq$. The metal centre experiences charge transfer Δ with its neighbouring ligands, with which there is an associated hopping integral V . On-site Coulomb repulsion U , the spin orbit interaction and a core hole potential Q are also necessary to describe the transition. While physical in origin, these parameters may be determined empirically through the use of standardized values, as implemented in the **CTM4XAS** code.

Based on the 4×1 reconstruction in Ref [142], it was possible to simulate XANES spectrum beyond the assumption of purely octahedral and tetrahedral site symmetry. If the surface Ti sites are considered as compressed in the direction of the surface normal, as occurs in the model for surface sites, it is additionally possible to calculate the dichroism of the X-ray spectra. The calculations presented below are based on a derivative method described in Ref [152, 153], where the parameters are fit to experimental measurements in an iterative process. In this case it was not necessary to perform cluster calculations, and so only the parameters in Table 6.1 are necessary to produce the calculated spectra in Figure 6.5.

While in their high symmetry configurations, both T_d and O_h sites would experience splitting of their $3d$ orbitals into e_g and t_{2g} orbitals with splitting controlled by only a $10Dq$ parameter, the surface compression of leads to D_{4h} symmetry at both sites. In this situation, the e_g orbitals further split into b_{1g} and a_{1g} orbitals, while the t_{2g} group splits into b_{2g} and e_g (see Figure 6.4). The single-particle energy shifts for each group can then be computed as follows:

$$\begin{aligned}
 E_{b_{1g}} &= 6Dq + 2Ds - Dt \\
 E_{a_{1g}} &= 6Dq - 2Ds - 6Dt \\
 E_{b_{2g}} &= -4Dq + 2Ds - Dt \\
 E_g &= -4Dq - Ds + 4Dt
 \end{aligned}
 \tag{6.1}$$

Table 6.1: Crystal field calculation parameters

Site	$10Dq$ (eV)	Ds (eV)	Dt (eV)	κ
T_d	-0.90	0.0298	-0.0037	0.65
O_h	2.20	0.0105	-0.0014	0.60

In the case of the 2×5 reconstruction, the surface Ti sites have a strained coordination between octahedral and tetrahedral. While each Ti has six neighbouring O's, they can be grouped into three pairs with Ti–O bond lengths of approximately 1.85 Å, 2.0 Å and 2.15 Å, as shown in Figure 6.6. The nearest two pairs are arranged in distorted tetrahedron, while including the third pair gives an overall distorted octahedral shape. In addition, each surface Ti in the structure has a slightly different configuration. Therefore,

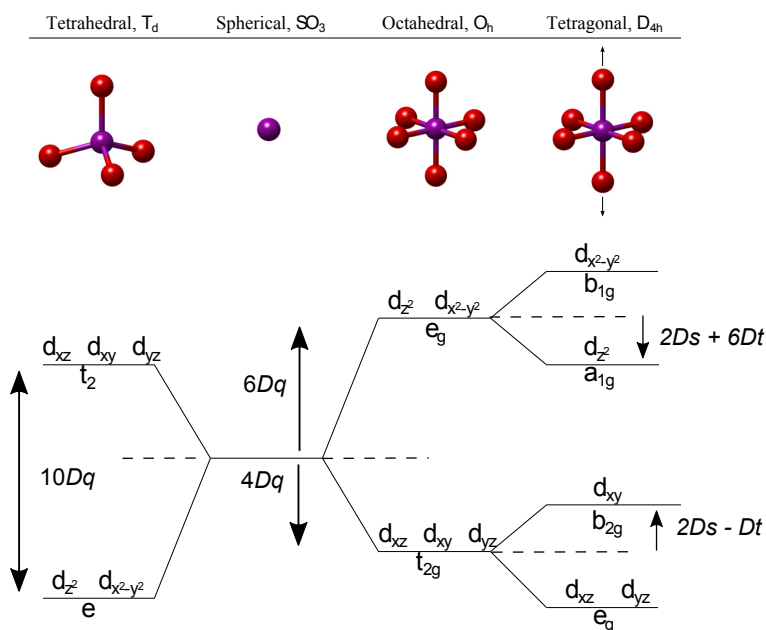


Figure 6.4: As ligands around a metal centre impose different site symmetries, $3d$ orbitals are split by the crystal field. The symmetry of each orbital leads to an associated energy gain or penalty for electrons occupation, causing degenerate orbitals to split. Adapted from Ref [152]

it is reasonable to model the Ti XANES spectrum as having both T_d and O_h contributions, and for it to be less sharply defined as it is an average of many inequivalent positions.

6.4 Calculated O *K* XANES

6.4.1 SrTiO₃ (110) 4×1 surface

O *K* spectra for the 4×1 reconstruction were calculated using the structure reported in Ref [142]. The following atomic sphere sizes were used: Sr - 2.4 bohr, Ti - 1.78 bohr, O - 1.61 bohr. To be consistent with the optimization conditions for the 2×5 structure, the PBEsol functional was used along with WIEN2k's EECE option to mix in Hawtree-Fowk exchange on the Ti $3d$ orbitals within the atomic spheres. A k -point mesh of $2 \times 6 \times 1$ was used (the cell's c axis was interrupted by vacuum). An RK_{max} of 5.00 was used.

Due to the large size of the 4×1 unit cell, it would have been computationally inefficient to attempt to simulate X-ray spectra using core-hole calculations on each of the surface O sites. Therefore, a selection of sites (as labelled in the primitive cell structure) was made, as summarized in Table 6.2 and shown in Figure B.1.

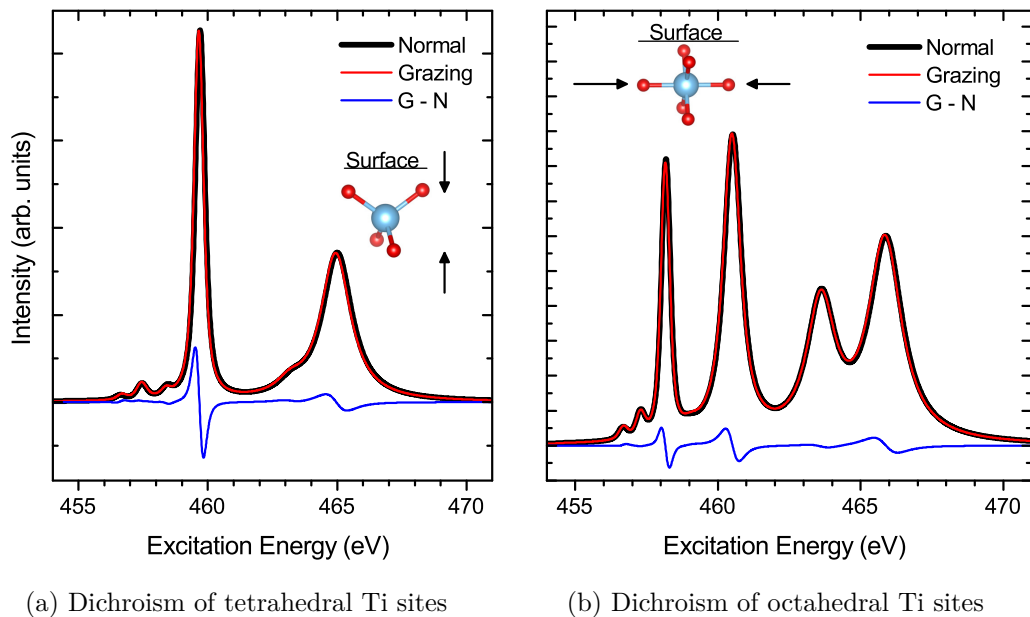


Figure 6.5: Calculated dichroism of the Ti $L_{2,3}$ XANES spectrum considering a compression in the surface normal of the upper-most tetrahedral sites, and tangential compression of the sub-surface octahedral sites.

Table 6.2: Calculated O K XANES sites in the 4x1 model

Site Name	Layer (cations)	Note
O69	S	Surface O bridging Ti's out of plane
O70	S-1	Surface O bridging Ti's in plane
O55	S-2	Subsurface O bonded to surface Ti
O18	S-6	Bulk O, out of plane with Sr
O2	S-7	Bulk O, in plane with Sr

6.4.2 SrTiO_3 (110) 2×5 surface

As a test, O K spectra for the 2×5 reconstruction were calculated on a 2×4 unit cell. While this model does not have the same periodicity in the b direction, it has nearly an identical structure, with the predominant feature in the O environment being strained Ti–O octahedra that approach tetrahedral coordination at the surface layer (see Appendix A for a comparison). Since the surface enthalpy of the predicted $2 \times 4a$ and $2 \times 5a$ reconstructions are equal within an error of 0.1 eV per unit cell (see Figure 6.14), and the high sensitivity of XANES to the local chemical environment, this model should be sufficient as an estimation of the O K XANES features.

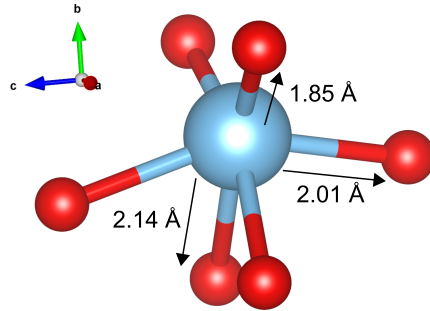


Figure 6.6: A sample bonding environment of a Ti site on the 2×5 surface. Bond length are the average of each pair (upper, middle, lower). The upper O's (in red) are at the surface (i.e. there is vacuum beyond them in the b direction).

The following atomic sphere sizes were used: Sr - 2.26 bohr, Ti - 1.76 bohr, O - 1.59 bohr. This structure was optimized using the PBEsol functional, along with WIEN2k's EECE option to mix in 50% Hawthtree-Fowk exchange on Ti $3d$ orbitals within the atomic spheres. A k -point mesh of $2 \times 1 \times 4$ was used (the cell's b axis was interrupted by vacuum). An RK_{max} of 6.25 was used (as a result of previous calculation performed using this model).

Similar to the 4×1 cell, only a subset of O sites were chosen for core-hole calculations, as summarized in Table 6.3 and shown in Figure B.2.

Table 6.3: Calculated O K XANES sites in the 2×4 model

Site Name	Layer	Note
O213	S	Nearest neighbour (NN) to surface Sr
O181	S	Mid-way between surface Sr rows
O119	S-2	3 NN Ti, 1 NN Sr
O133	S-2	4 NN Ti, in T_d symmetry site
O41	S-4	2 Sr NN, near T_d symmetry site
O129	S-4	beneath surface Sr
O141	S-4	beneath surface Sr, bonds perpendicular to surface
O157	S-4	next to bulk Sr

6.5 Experimental Results and Discussion

6.5.1 4×1 Surface Reconstruction

Of particular interest in the study of the 4×1 was its predicted tetrahedrally coordinated Ti sites. Since the majority of Ti in STO occupies bulk octahedral positions, it was hoped that the local bonding environment at the surface would prove sufficiently different from the bulk that it could be detected using XANES. Such detection would provide a

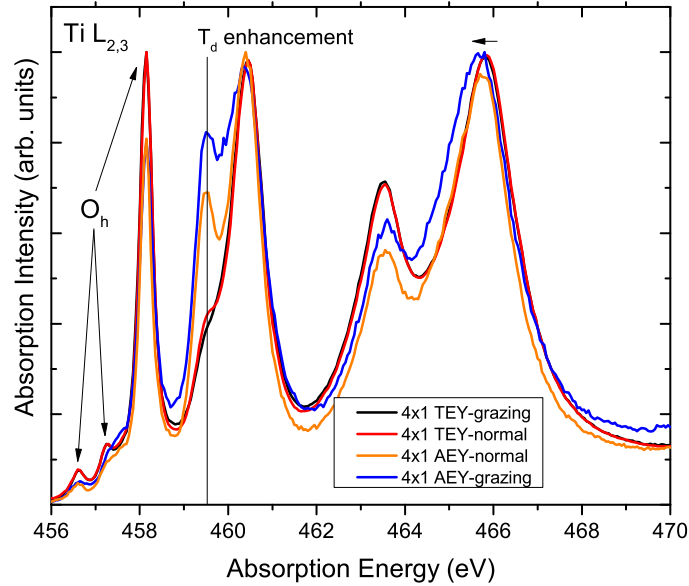


Figure 6.7: Ti $L_{2,3}$ XANES of the 4×1 surface reconstruction. As the measurement becomes increasingly surface sensitive, there is enhancement of a peak at 459.5 eV associated with tetrahedrally coordinated Ti. Also the onset peaks and the first major peak at 458 eV, contributed by octahedral states, decrease in intensity.

strong experimental confirmation of the structure in Ref [142]. As shown in Figure 6.7, a feature in the Ti $L_{2,3}$ XANES spectra at 459.5 eV (to be referred to as the T_d feature) was seen to be strongly associated with the upper-most surface states, being enhanced in AEY versus TEY, and further enhanced when the experiment was performed in a grazing-angle geometry.

The location of the T_d feature is in good agreement with the calculated XANES of tetrahedrally coordinated Ti, as shown in Figure 6.8. It also agrees with measured Ti $L_{2,3}$ XANES spectra for TiCl_4 [154], as well as ELNES of orthorhombic Ba_2TiO_4 [155], both of which contain tetrahedrally coordinated Ti in the bulk. In addition, by considering a weighted sum of the simulated dichroism (in Figure 6.9 using a sum $0.35T_d + 0.65O_h$), the experimental dichroism is well reproduced, indicating a good agreement of the surface relaxations in the structural model with the physical surface.

6.5.2 2×5 Surface Reconstruction

As discussed in section 6.3, the 2×5 reconstruction (and other similar reconstructions) feature a surface semi-tetrahedral Ti layer on top of a less-strained octahedral Ti layer. As a result, the T_d feature is no longer as sharply defined, as shown in Figure 6.10. The

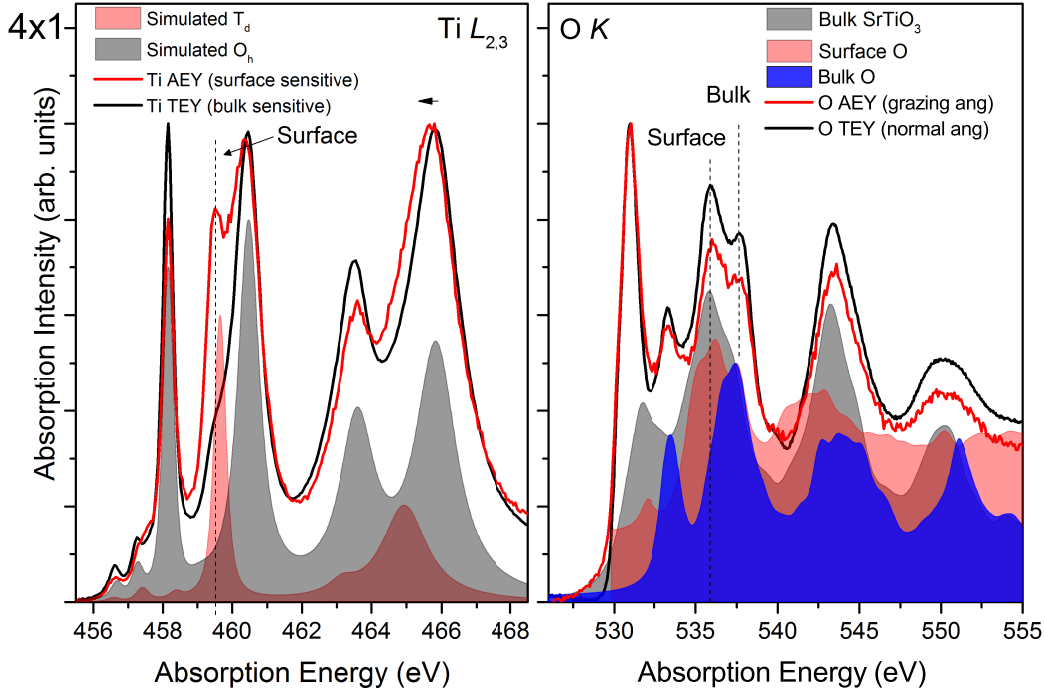


Figure 6.8: Comparison of the calculated and experimental XANES for the STO110 4×1 surface reconstruction. The Ti $L_{2,3}$ simulations are crystal field multiplet calculations, while the O K simulations are WIEN2k `xspec` simulations. The "Surface O" simulation is a sum of the O55 and O69 sites, while "Bulk O" is a sum of the O2 and O18 sites. In the Ti $L_{2,3}$ measurements, the surface feature at 459.5 eV is sharply defined in the AEY channel, indicating a clear contribution from tetrahedral surface sites. In the O K measurements, there are no strongly sensitive surface states (that AEY can discriminate). However the XANES simulation shows that the feature at 537.5 eV has more near-bulk O contribution than the peak below it at 536 eV. The other features (besides the onset excitonic peak, which did not to as low energy as in experiments) are bulk in origin, and compare well bulk SrTiO₃.

local structure probed by AES XANES is no longer particularly able to discriminate between the bulk octahedral Ti and these strained surface octahedral sites. As a result, the Ti $L_{2,3}$ measurements of this reconstruction are not particularly useful in elucidating its structure.

An interesting result of the O K measurements is that the feature at 537.5 eV becomes strongly surface sensitive, unlike the 4×1 measurement. By decomposing the simulated WIEN2k X-ray spectra into in and out-of-plane contributions it becomes clear that this sensitivity is due to a sharp contribution from the in-plane orbitals (in this case PX+PZ orbitals) of the surface O sites. This is the most prominent difference in the X-ray spectra

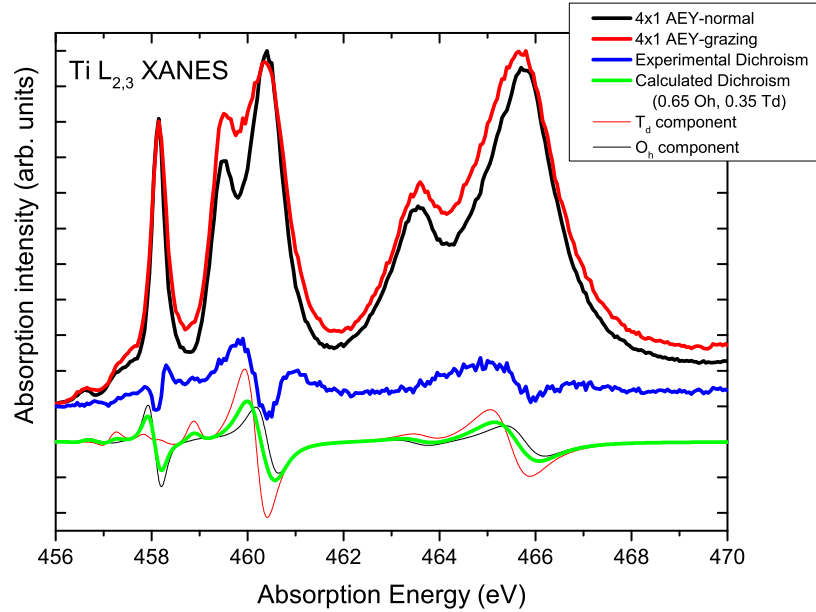


Figure 6.9: Comparison of the simulated and experimental (grazing minus normal) Ti $L_{2,3}$ dichroism, arising from the selective excitation of Ti orbitals in and perpendicular to the surface plane.

between these two surface reconstructions, and in contradiction to the 4×1 calculations that indicated this feature was primarily of near-bulk O origin. This would seem to indicate that the distortion of the T_d surface Ti sites, along with the reconstruction change, leads to a re-ordering of orbitals, which could have a significant effect on the chemical properties of this surface versus the more stable 4×1 reconstruction.

6.6 Calculated DOS

Below E_F , XPS measures occupied density of states in the valence band, and can be compared to ground state calculated DOS from the two structural models. The valence band of SrTiO_3 is composed primarily of Ti $3d$ and O $2p$ states, and is shown in Figure 6.12. There are three main differences between the two surface structures considered:

- The 4×1 has more Ti states at the lower energy end of the valence band. This is seen in the valence band XPS as a higher peak ratio favouring the lower energy peak.
- The 2×4 has a slightly higher valence band width, likely due to the larger unit cell and higher number of inequivalent Ti atoms causing greater band dispersion.

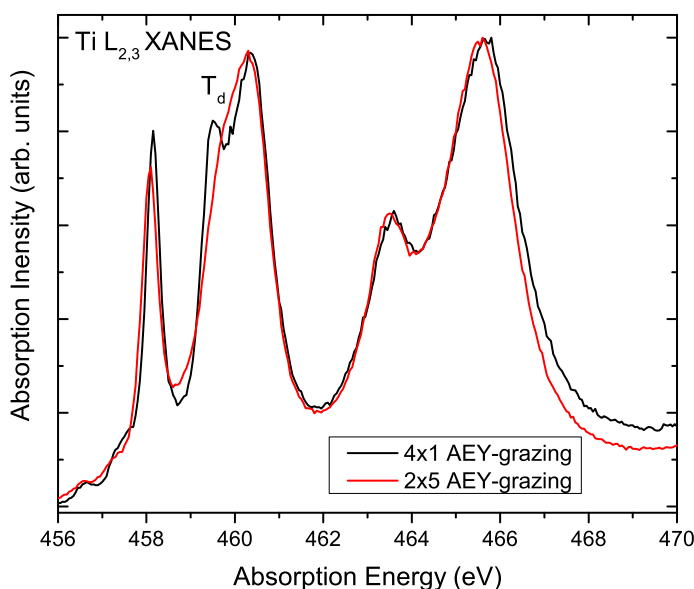


Figure 6.10: In comparison to the 4×1 surface, the T_d peak on the 2×5 surface becomes a broad shoulder. This is consistent with the mixture of T_d and O_h -like sites in the surface reconstruction, caused by distorted octohedral sites in the 2×5 reconstruction's sublayer.

- The 2×4 structure has a band gap about 0.6 eV lower than the 4×1 structure.

In general the DOS calculations are in good agreement with the VB XPS with respect to bandwidth and peak ratio. However VB XPS is significantly broadened by state lifetime effects and cannot reveal fine structure directly, so there are limited features with which to compare. To show the contribution of surface Ti and O to the density of states near the Fermi edge, overall partial DOS plots were created by averaging contributions from each Ti and O site, then comparing to a restricted surface set. This comparison is shown in Figure 6.13. In general the surface states did not contribute to the valence and conduction band edges, suggesting a stable surface without a defect-like termination with dangling bonds.

6.7 Stoichiometry Change at the STO (110) Surface

STO is another example of a metal oxide that undergoes a stoichiometry change at its surface reconstruction. In this case we have specifically tuned the surface stoichiometry by dosing of Sr or Ti, but unlike in magnetite, the perovskite lattice does not permit cations to easily migrate in order to compensate. Instead, oxygen vacancies are the more

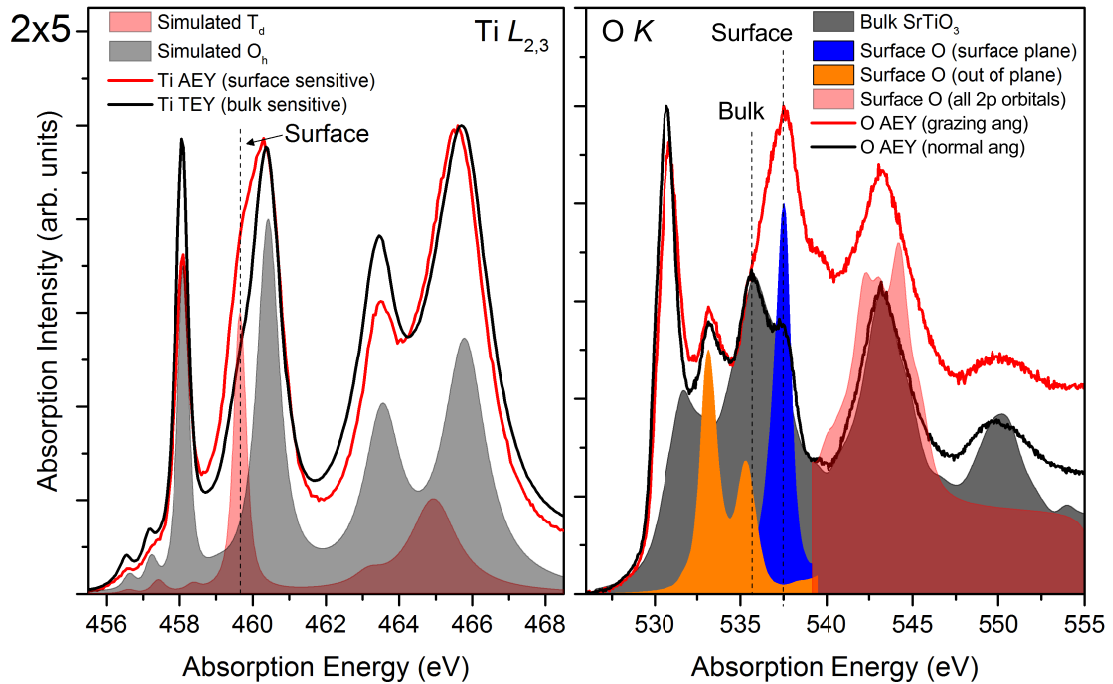


Figure 6.11: Comparison of the calculated and experimental XANES for the STO110 2×5 surface reconstruction. The T_d feature in the Ti $L_{2,3}$ spectra is no longer as sharp in the AEY, consistent with a transition from tetrahedral to strained octahedral Ti on the 2×5 surface. While the normal O K AEY and both TEY orientations (not shown) appear the same as the 4×1 reconstruction, the grazing angle AEY becomes strongly peaked at 537.5 eV, which can be attributed to a contribution from PY orbitals of the surface O's (O181, and O213 in the model).

stable, intrinsic defect, even to the point of being able to form clusters[156]. Indeed, the mobility of oxygen (and oxygen vacancies) in STO is high enough that the effect could potentially be used for resistive switching[157].

At the STO surface, oxygen vacancies that form are likely to result in oxygen being expelled into the vacuum. Therefore the appearance of tetrahedral Ti sites can be thought of as an equilibrium being established between oxygen vacancy formation and Ti's preferred octahedral coordination. The propensity for sub-surface oxygen vacancies to migrate to the surface has been established by molecular dynamics simulations[132]. In this case 6-fold coordinated octahedral Ti is reduced to 4-fold coordinated tetrahedral Ti, beyond which further oxygen does not leave, at least in our system being annealed in UHV at elevated temperature. We can therefore think of this situation as a rejection of oxygen from the STO surface, leading to the stabilization of an unusual Ti–O species

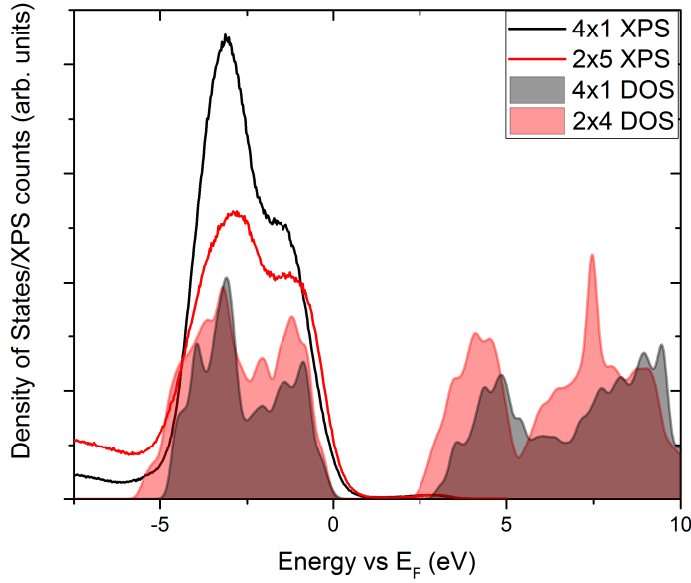


Figure 6.12: Comparison of the total DOS for the 4×1 and 2×4 calculations with valence band XPS (note the 2×5 surface was measured). The band gap of the 2×4 structure has decreased by about 0.56 eV (to 2.34 eV) as compared to the 4×1 (2.90 eV). Additionally, the bandwidth of the valence band has slightly increased.

that does not occur in the bulk. This change in the O stoichiometry directly relates to the chemical potential through the Gibbs free energy of the system (N_O being the number of O in the system):

$$\mu_O = \left(\frac{\partial G}{\partial N_O} \right)_{T,P,N_{i \neq O}} \quad (6.2)$$

Thus the chemical potential of oxygen can be considered a driving force in the surface reconstruction of STO. While it does not directly act on cation occupation, as in the magnetite (001) surface, there is a sufficient change in oxygen concentration/occupation to force the cations into otherwise unfavourable configurations.

Of the two surface reconstructions considered here, the 2×5 surface has been shown to be slightly more stable. as shown in Figure 6.14, while the 4×1 surface is the most stable of a homologous series of $m\times 1$ reconstructions[142]. In transitioning from 2×5 to 4×1 the surface density of TiO_2 decreases by almost a factor of two, which is roughly consistent with the transition from a monolayer to a bi-layer surface reconstruction. If one thinks of the surface reconstruction as a thin film growing on top of the STO (110)

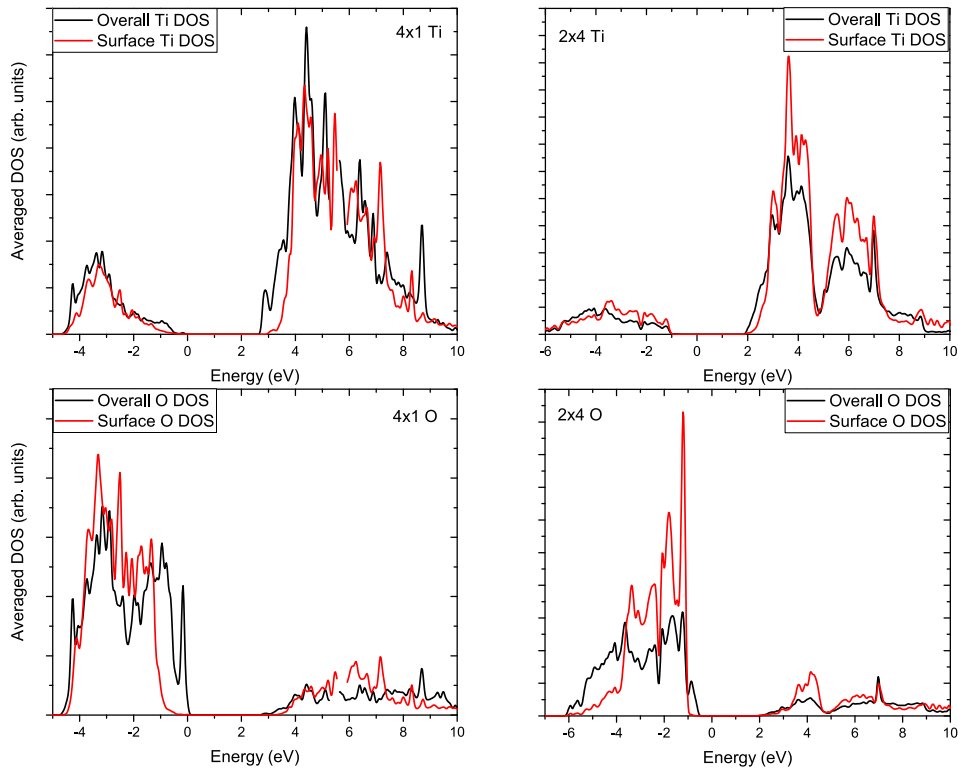


Figure 6.13: The relative contribution of surface O and Ti to the DOS. At the 4×1 surface, surface atoms do not contribute to valence or conduction band edges. This effect is less pronounced in the 2×4 structure, with the surface O contributing strongly in the upper valence band.

bulk, then the small difference in the enthalpy of the two films serves as a demonstration that competing processes in each film's formation must have free energy costs or gains of roughly equal magnitude. In this case, the energy penalty of forming Ti–O tetrahedra and the associated tensile stress in placing this structure on the STO substrate beneath must roughly equal a free energy gain from changing the surface stoichiometry and oxygen chemical potential.

That the 4×1 surface can be formed at all is evidence that oxygen or other chemical potentials can serve as "control knobs" and used to engineer surface films that have unusual structure or electronic properties but would be otherwise unstable. Such control could be of general interest in the creation of functional surfaces with properties very different from that of a bulk material or its simple surface reconstructions. The reported 2-dimensional electron gas beneath the STO (110) 4×1 surface after the creation of synchrotron beam-induced oxygen vacancies already presents an example of such an application[132].

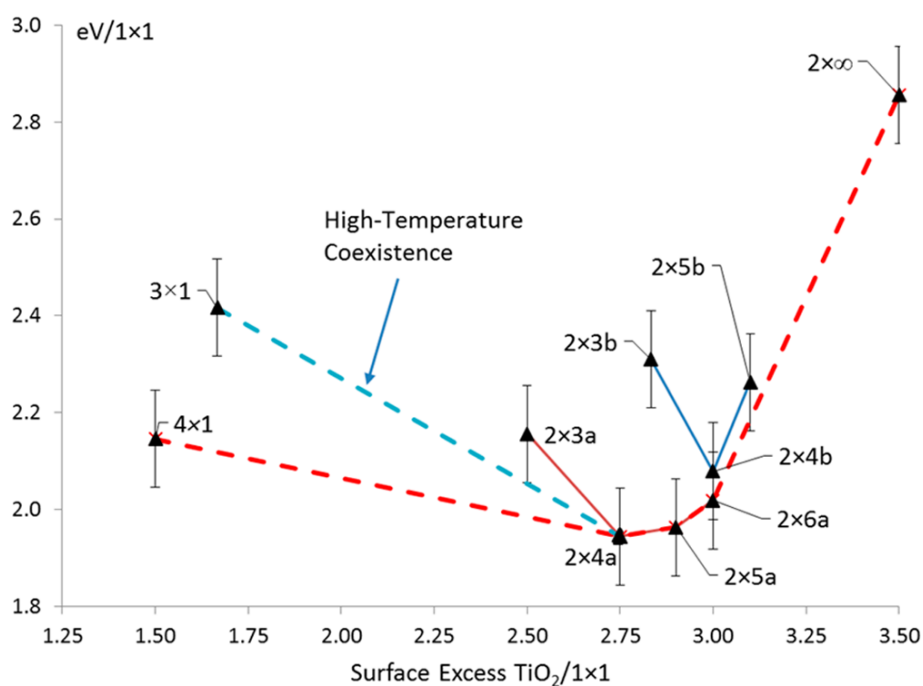


Figure 6.14: Convex-hull diagram of the surface enthalpies of various surface reconstructions on the STO (110) surface, plotted per excess unit of TiO₂ per unit cell (lower is more stable). Error bars are 0.1 eV per 1 × 1 bulk unit cell. Reproduced from Ref. [144]

Conclusions

Throughout this dissertation, the important interplay between theory and experiment has been highlighted, as well as the necessity of using both to understand the behaviour and properties of complex metal oxide systems. Below the results will be summarized, and some brief are made about directions of future work.

7.1 Magnetite (001)

In Chapter 5 the magnetite (001) surface was introduced, including the understanding of its B-layer surface reconstruction that existed before this work commenced. Several problems were highlighted with this understanding, including the difficulty in reconciling the $(\sqrt{2} \times \sqrt{2})R45^\circ$ surface reconstruction with polar considerations, the challenge of understanding why only one of two sites in the $(\sqrt{2} \times \sqrt{2})$ served as an adsorption site for metals adatoms, and indeed the structural nature of that site: is it "wide" or "narrow"?

To resolve these issues, an unusual concept for a surface reconstruction was introduced: a structure including an ordered array of subsurface cation vacancies (SCV). First the structure was proposed based on experimental observations of selective site adsorption and adatom incorporation into the surface. The proposed structure was relaxed with DFT, producing a surface with wavy rows as observed in STM measurements. The DFT model allowed for the selective adsorption of Au and other adatoms to be understood, since an interstitial Fe_A blocked one of two sites in the $(\sqrt{2} \times \sqrt{2})$ unit cell. STM simulations using the DFT model also correctly reproduced the change in phase of the "wide" and "narrow" surface sites being reversed when imaging at low versus high bias. Most importantly, the SCV structure was shown to have a lower surface energy than a distorted B-layer termination under UHV preparation conditions. The chemical potential of oxygen at the magnetite surface seems and its ability to modify the surface stoichiometry seems to be key to this stability.

In parallel, the SCV structure was refined from a conceptual structure and compared with LEED IV measurements, resulting in an excellent fit of $R_P = 0.125$, comparable to the fit of clean metal surfaces. This independent experimental confirmation of the SCV structure allows us to be confident in using it to study other behaviour and phenomenon on the magnetite (001) surface, including adsorption and incorporation of various elements as adatoms. The existence of the SCV structure also has some interesting consequences, including a magnetic surface oxygen site that may be stabilized in a 1- oxidation state. The stoichiometry change of the SCV structure also leaves the surface rich in Fe^{3+} , which explains reports of a magnetic dead layer, low net moment and a band gap at the magnetite surface. The stoichiometry change also serves a critical role in terminating the layered polar structure without a polar catastrophe.

Not all problems with the magnetite (001) surface are resolved however, and there exists potential for future work. The dynamics of the reconstruction are difficult to investigate using DFT, but may give interesting answers as to how metal adatom incorporation functions, or what energy barriers exist to the either cation vacancies formation or the surface B-layers straightening as the $(\sqrt{2}\times\sqrt{2})$ reconstruction lifts. In particular, it has been reported that adsorption of hydrogen causes a lifting of the $(\sqrt{2}\times\sqrt{2})$ structure and a 1×1 LEED pattern to emerge[158]. The mechanism of this transition is an interesting question. Does hydrogen allow the surface layers to straighten? Does it incorporate into the vacancies and lift the reconstruction that way? Does the introduction of hydrogen create such a reducing environment that Fe can migrate out of the bulk to refill the vacancies? Further investigation will be required to answer these questions.

7.2 Strontium Titanate (110)

Similarly to magnetite, Chapter 6 introduces the (110) surface of SrTiO_3 . This ternary oxide is even more complicated, and a large number of mutually metastable surface reconstructions can be formed on the surface by changing the Sr and Ti concentration, then annealing. Understanding the electronic structure of these different surface reconstructions promises a better ability to control this material for a variety of interesting applications.

X-ray spectroscopy measurements of two SrTiO_3 (110) surface reconstructions were presented, and their agreement with simulated spectra serves as supporting verification of the published structures for the 4×1 and 2×4 surface reconstructions. In particular, the ability to measure the XANES contribution of surface tetrahedral Ti on the 4×1 gives a clear confirmation of the presence of this unusual Ti species in the surface termination. The inclusion of T_d Ti at the surface reinforces the ability of the surface discontinuity at polar surfaces to stabilize otherwise unfavourable configurations.

The ability for a wide range of surface reconstructions to be prepared on the STO (110) surface shows that control of the oxygen chemical potential (in this case indirectly, through cation concentrations) at the surface of a metal oxide can play a strong role in the creation of non-equilibrium surfaces with interesting functional properties. The emergence of novel properties, such as a 2-dimensional electron gas under a 4×1 structure with oxygen

vacancies serves as a call to better understand the processes at play during formation of these reconstructions, so that they can be integrated with other semiconductor processing techniques for use in devices, for example. The presence of complex surface reconstruction also creates a large playing field for investigating the deposition of catalysts or adsorption of water molecules, to understand how STO serves as a catalytic support.

7.3 Contributions to Publications

7.3.1 Magnetite SCV model

The model present in this dissertation was a result of intense collaboration, and while I present a variety of theoretical and experimental work, I was chiefly responsible for relaxing the structure that would serve as the theoretical basis of the Surface Cation Vacancy reconstruction. With this model, I contributed and interpreted STM simulations of the magnetite (001) ($\sqrt{2}\times\sqrt{2}$)R45° surface and, with the assistance of Roland Bliem, constructed a surface phase diagram. This work resulted in two manuscripts where I appear as an author (Refs [90, 99]). I contributed substantially to the preparation of the first manuscript, but the second was prepared and submitted while I was unavailable to assist for health reasons.

7.3.2 SrTiO₃ Surface Reconstructions

In this section I present highly surface sensitive X-ray adsorption measurements that I collected with members of the surface physics group of Prof. Ulrike Diebold. I analyse these spectra here with the aid of theoretical O *K* spectra calculated by myself from structures produced by the group of Laurence D. Marks, and Ti *L*_{2,3} spectra calculated in collaboration with Robert J. Green. The experimental and Ti *L*_{2,3} work resulted in two publications (Refs [144, 146]), for both of which I assisted by reviewing the manuscript. However, the analysis of O *K* XANES presented in this dissertation remains unpublished to date.

7.3.3 Other Publications

While not exactly in keeping with the theme of this dissertation, I also performed DFT calculations on Co-decorated, partially oxidized graphene during the course of my Doctoral studies, resulting in one publication (Ref [159]). While a 2-dimensional material is similar to the surface of a solid in many ways, there did not exist sufficient understanding of the structure of this material to treat it with a similar depth as the other systems I have presented in this work. For this reason it did not make sense to include discussion of this project in this dissertation.

During the first few months of my Doctoral studies I also wrote and published a manuscript based on experimental work performed during my Masters degree (Ref [160]), in addition to making minor contributions to other manuscripts (as listed in my CV). I acknowledge Prof. Blaha and the FWF for their resources and financial support while I completed this work.

STO 2×4 Surface Reconstruction

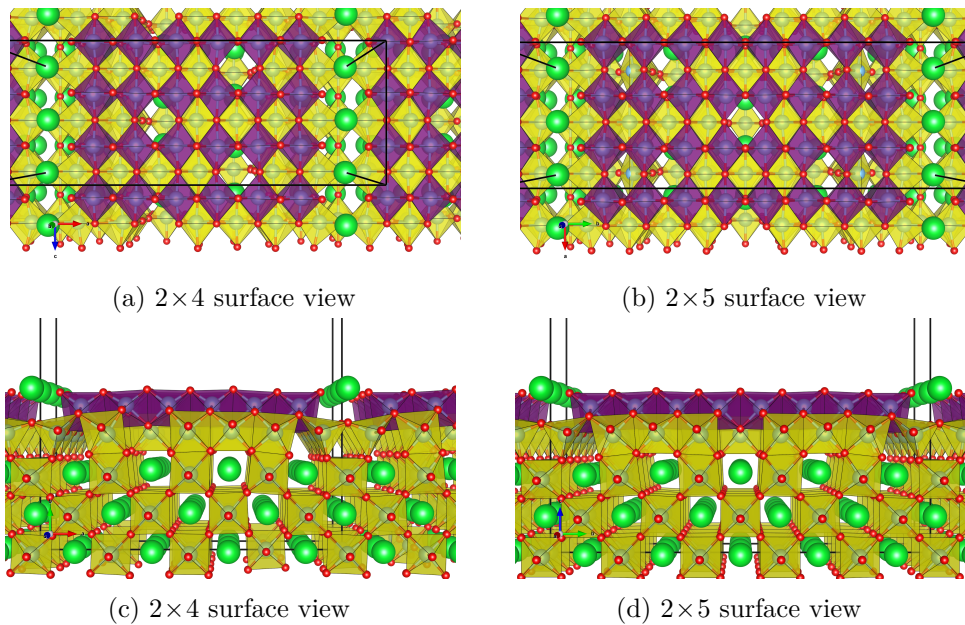


Figure A.1: Comparison of the 2×4 reconstruction used for O K XANES calculations (left) and the measured 2×5 reconstruction (right). The 2×5 reconstruction is wider, allowing it to be more symmetric about the coordinating surface Sr sites. Sr - green, Ti - blue, O - red. Purple polyhedra are the strained octahedral surface sites, yellow polyhedra are more bulk-like, though there is still significant distortion in the subsurface layer.

Core Hole Sites for STO Calculations

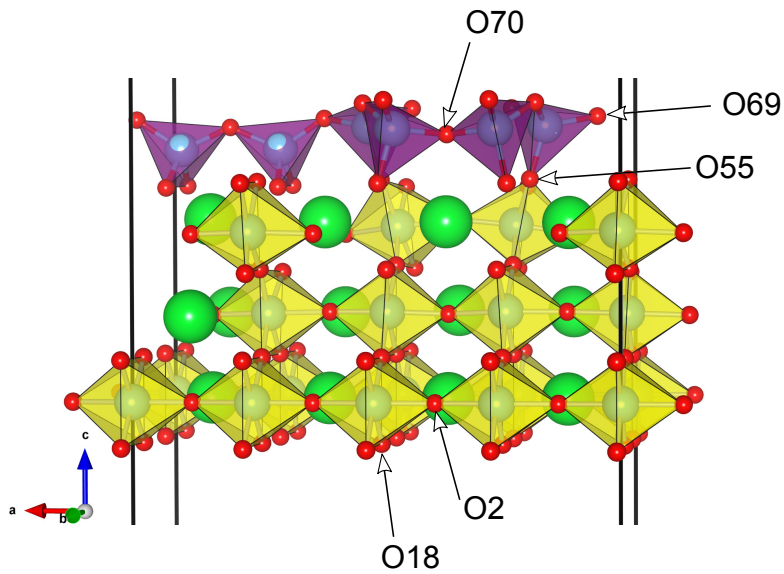


Figure B.1: Locations of the O core holes in calculations performed on the 4×1 surface structure, for O K XANES simulations. Three classes of surface site were chosen: the surface-most O69, a lower bridging O70 closer to a surface Sr, and O55 which connects to a more bulk-like Ti. Two "bulk" O were chosen, O2 in the Sr column and O18 in the Ti column, to account for any loss of degeneracy due to the presence of the surface.

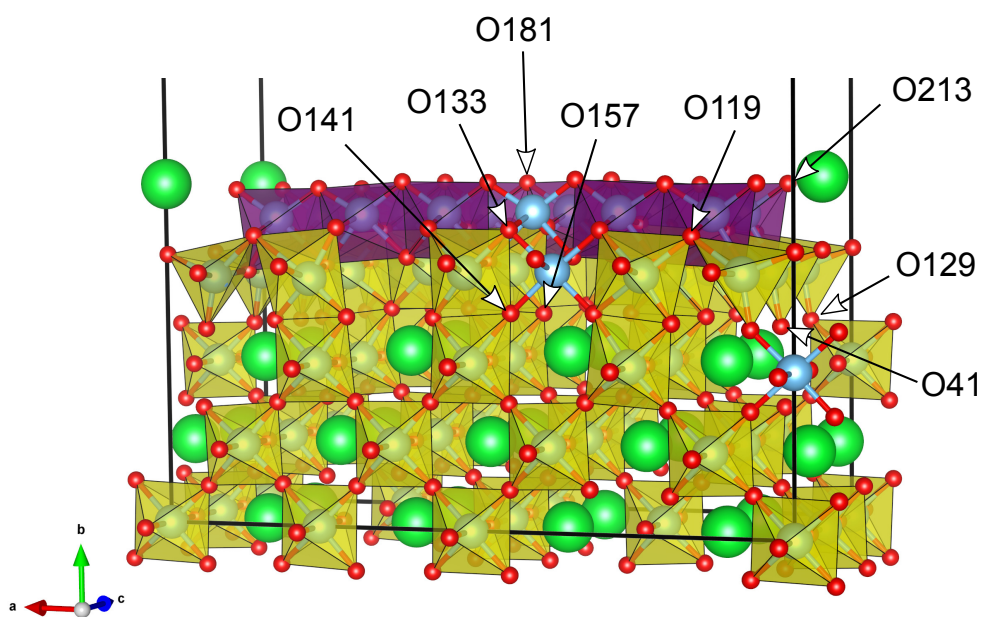


Figure B.2: Locations of the O core holes in calculations performed on the 2×4 surface reconstruction, for O K XANES simulations. While the structure was too large to be comprehensively sampled with core holes, O sites were chosen "near" and "far" from the coordinating surface Sr in the a direction, and "adjacent" and "not adjacent" to bulk Sr.

List of Figures

2.1	Exchange correlation enhancement factor $F_{xc}(r_s, s)$ versus reduced density gradient of the PBE and PBEsol functionals. The above plot is made for Wigner-Seitz radius $r_s = 1$ bohr. Courtesy of Dr. Fabien Tran	8
2.2	In a Mott insulator, strong electron correlation is underestimated and LDA will place a $3d$ band at the Fermi level, giving an un-physical metallic solution. By adding a Hubbard U , electrons tend to localize on lattice sites and the metallic band splits into upper and lower Hubbard bands, producing the correct insulating behaviour. In the same way, the population of up vs down electrons can be tuned, correcting erroneous moments.	9
2.3	Depiction of a wave function between two atomic nuclei. The potential in the nuclear region causes the function to vary quickly rapidly within a certain radius, but slowly in the interstitial.	11
2.4	Division of space used in the APW method. Two atoms (S_α and S_β) are surrounded by interstitial region I . Within the sphere of radius \bar{R}_α centred at \bar{r}_α , wave functions will use S_α atomic orbitals as a basis. Reproduced from Ref. [30]	12
3.1	A simple slab structure of a rocksalt crystal. The unit cell is indicated by the solid line, and images of the unit cell are separated by a vacuum layer.	18
3.2	Tasker's three surface terminations for non-metallic surfaces. Layers in type 1 surfaces have no net charge. Type 2 surfaces have charged layers, but no macroscopic net dipole. Type 3 surfaces accumulate a net dipole, which must somehow be relieved.	20
3.3	A generic FCC structure with a compensating surface termination layer of $\frac{1}{2}\rho$. Such a surface has a converging surface energy.	21
4.1	STM tunnelling geometry	25
4.2	Experimental setup of an XPS measurement.	27
4.3	Universal curve for electron inelastic mean free path through a solid. Based on Equation 5 from Ref [52].	28
4.4	Setup of a synchrotron XAS experiment, with TFY, TEY and AEY being measured.	29
		87

4.5	An example of a $KL_1L_{2,3}$ Auger electron process, where a $1s$ core hole is filled by a $2s$ electron, with the resulting kinetic energy imparted to a $2p$ electron.	31
4.6	Low energy electrons are scattered off a sample surface (left). Constructive interference from the backscatter forms diffraction spots on a fluorescent grid. The resulting pattern is observed through a window and can be quickly used to identify surface reconstructions (right).	35
4.7	Labelling scheme for the (100) face of a simple cubic lattice with a (2×1) superstructure with the same symmetry. Open circles are the extra spots associated with the surface structure, and would appear dimmer in LEED.	36
5.1	Structure of bulk magnetite. Tetrahedral Fe_A and octahedral Fe_B occupy a body-centred cubic O lattice in anti-ferromagnetically coupled layers.	40
5.2	$(\sqrt{2} \times \sqrt{2})R45^\circ$ LEED pattern on an annealed Fe_3O_4 (001) surface, $E=95$ eV. Reprinted from Ref. [89] with permission from Elsevier.	41
5.3	High resolution image of the magnetite surface (001). At low bias (here $V=0.17$ V), individual Fe_B sites can be distinguished. The wavy pattern alternates between rows, giving a $(\sqrt{2} \times \sqrt{2})$ unit cell. The \times indicates the site of selective adatom adsorption in the reconstruction. From Ref [90]. Reprinted with permission from AAAS.	42
5.4	Depiction of the polar catastrophe of an un-reconstructed B-layer termination. The divergent surface energy will force the surface to reconstruct.	43
5.5	STM image ($300 \times 300 \text{ \AA}^2$, $V = +1$ V) of 0.12 ML Au deposited on Fe_3O_4 at room temperature. The inset shows two adatoms occupying neighbouring $(\sqrt{2} \times \sqrt{2})$ unit cells. Reprinted figure with permission from Ref [96]. Copyright 2012 by the American Physical Society.	44
5.6	Structure of the magnetite-like maghemite, $\gamma\text{-}Fe_2O_3$. The maghemite structure is characterised by a random distribution of octohedral Fe_B vacancies, depicted here as un-filled blue spheres.	45
5.7	Unit cell volume optimizations for $U = 3.8$ eV	48
5.8	Relaxed SCV structure on the surface of a 17-layer slab (left). Undulation of the surface Fe_B layers becomes pronounced, and the interstitial Fe_A sits in the "narrow" site between Fe_B rows. The "wide" site is bounded by under-coordinated Os that sit slightly relaxed towards the bulk. Viewed from above (right), the selective adsorption site is marked with a \times .	49
5.9	Surface phase diagram comparing the SCV and DBT structures over two extremes of μ_O : rejection of O from the bulk (low μ_O) to spontaneous formation of O_2 on the surface (high μ_O). From Ref [90]. Reprinted with permission from AAAS.	50

5.10	The appearance of row undulations on the SCV surface are strongly controlled by STM bias. Experimental STM images (A-C) were obtained at the same position (in comparison to the Fe adatom in the top-left). As the bias voltage was increased the apparent phase of the surface undulations shift, with the preferred adatom adsorption site (marked with an \times) going from "narrow" to "wide". This can be understood as a purely electronic effect, as seen in simulated STM images (D-F). By looking at an adsorption site in cross section (G-I, showing the path marked by a red line in D), it is clear that t_{2g} orbitals on the surface Fe_B atoms (blue dashed circles) are tilted towards the adsorption site. As shown in J, t_{2g} orbitals contribute at energies just above E_F , and are consequently imaged at low bias. As bias increases, the spherically symmetric d_z^2 and $d_{x^2-y^2}$ begin to dominate the STM image, and the true underlying row structure is revealed. From Ref [90]. Reprinted with permission from AAAS.	51
5.11	Photo of a crystalline magnetite sample mounted on a conducting sample plate. Courtesy of Roland Bliem.	52
5.12	Comparison of measured and simulated LEED IV beams of an SCV reconstructed surface. All symmetrically equivalent beams are compared in the supplemental to Ref [90]. The overall agreement of all beams with the best-fit structure gives a R_P of 0.125. From Ref [90]. Reprinted with permission from AAAS.	54
5.13	Structure of adsorbed Au on the SCV surface, with one Au per $(\sqrt{2} \times \sqrt{2})$ cell. The Au binds (2.03 eV) above the unblocked bulk-continuation site, between the two under-coordinated surface Os. From Ref [90]. Reprinted with permission from AAAS.	55
5.14	Core O $1s$ binding energies of the SCV structure as a function of depth, for both a 17 and 25-layer slab. The magnetic O^{1-} site diverges significantly from the other oxygen at the structure, suggesting a change in oxidation state that is potentially observed in XPS measurements. Final state effects are considered by including a half-core hole on bulk magnetite and surface SCV sites as described in Ref [115].	57
5.15	Assuming the two magnetic O sites have a -1 formal charge, the SCV surface gives a total formal charge of +3, as is necessary to prevent a polar catastrophe. 58	
5.16	Total DOS of bulk cubic Fe_3O_4 versus the SCV reconstruction on a 17 layer slab. The bulk band crossing the Fermi level, originating from Fe_B $3d$ electrons, splits in the SCV model, creating a 0.2 eV band gap. The filled states below E_F are contributed by bulk-like $\text{Fe}_B^{2.5+}$, while the empty states just above the gap are surface Fe_B^{3+} states.	59

6.1	A cleaved plane of the SrTiO ₃ (110) surface, as well as the surface reconstructions studied experimentally in this chapter. A smaller 2×4 unit cell with similar structure was used for the 2×5 O <i>K</i> XANES calculations (see Appendix A). Sr - green, Ti - blue, O - red. Purple polyhedra in the 4×1 reconstruction are tetrahedral, while in the 2×5 they are highly strained octahedra, as depicted in Figure 6.6. Yellow octahedra are bulk-like Ti. Fig 6.1a is reprinted by permission from Macmillan Publishers Ltd: Ref [137], copyright 2010.	62
6.2	Sample crystal of SrTiO ₃ as used in the XPS/XANES experiments, mounted on a conducting sample holder.	64
6.3	Sample XPS overview of clean SrTiO ₃ (110) with a 4×1 reconstruction. Under an X-ray excitation of 1254 eV, the Ti LMM Auger lines appear as highlighted in red, while the O KLL Auger lines are highlighted in orange. The intensity of these lines are used for collecting the Auger Electron Yield measurements mentioned. Other relevant lines are labelled.	65
6.4	As ligands around a metal centre impose different site symmetries, 3 <i>d</i> orbitals are split by the crystal field. The symmetry of each orbital leads to an associated energy gain or penalty for electrons occupation, causing degenerate orbitals to split. Adapted from Ref [152]	67
6.5	Calculated dichroism of the Ti <i>L</i> _{2,3} XANES spectrum considering a compression in the surface normal of the upper-most tetrahedral sites, and tangential compression of the sub-surface octahedral sites.	68
6.6	A sample bonding environment of a Ti site on the 2×5 surface. Bond length are the average of each pair (upper, middle, lower). The upper O's (in red) are at the surface (i.e. there is vacuum beyond them in the <i>b</i> direction). . . .	69
6.7	Ti <i>L</i> _{2,3} XANES of the 4×1 surface reconstruction. As the measurement becomes increasingly surface sensitive, there is enhancement of a peak at 459.5 eV associated with tetrahedrally coordinated Ti. Also the onset peaks and the first major peak at 458 eV, contributed by octahedral states, decrease in intensity.	70
6.8	Comparison of the calculated and experimental XANES for the STO110 4×1 surface reconstruction. The Ti <i>L</i> _{2,3} simulations are crystal field multiplet calculations, while the O <i>K</i> simulations are WIEN2k xspe c simulations. The "Surface O" simulation is a sum of the O55 and O69 sites, while "Bulk O" is a sum of the O2 and O18 sites. In the Ti <i>L</i> _{2,3} measurements, the surface feature at 459.5 eV is sharply defined in the AEY channel, indicating a clear contribution from tetrahedral surface sites. In the O <i>K</i> measurements, there are no strongly sensitive surface states (that AEY can discriminate). However the XANES simulation shows that the feature at 537.5 eV has more near-bulk O contribution than the peak below it at 536 eV. The other features (besides the onset excitonic peak, which did not to as low energy as in experiments) are bulk in origin, and compare well bulk SrTiO ₃	71

6.9	Comparison of the simulated and experimental (grazing minus normal) Ti $L_{2,3}$ dichroism, arising from the selective excitation of Ti orbitals in and perpendicular to the surface plane.	72
6.10	In comparison to the 4×1 surface, the T_d peak on the 2×5 surface becomes a broad shoulder. This is consistent with the mixture of T_d and O_h -like sites in the surface reconstruction, caused by distorted octohedral sites in the 2×5 reconstruction's sublayer.	73
6.11	Comparison of the calculated and experimental XANES for the STO110 2×5 surface reconstruction. The T_d feature in the Ti $L_{2,3}$ spectra is no longer as sharp in the AEY, consistent with a transition from tetrahedral to strained octahedral Ti on the 2×5 surface. While the normal O K AEY and both TEY orientations (not shown) appear the same as the 4×1 reconstruction, the grazing angle AEY becomes strongly peaked at 537.5 eV, which can be attributed to a contribution from PY orbitals of the surface O's (O181, and O213 in the model).	74
6.12	Comparison of the total DOS for the 4×1 and 2×4 calculations with valence band XPS (note the 2×5 surface was measured). The band gap of the 2×4 structure has decreased by about 0.56 eV (to 2.34 eV) as compared to the 4×1 (2.90 eV). Additionally, the bandwidth of the valence band has slightly increased.	75
6.13	The relative contribution of surface O and Ti to the DOS. At the 4×1 surface, surface atoms do not contribute to valence or conduction band edges. This effect is less pronounced in the 2×4 structure, with the surface O contributing strongly in the upper valence band.	76
6.14	Convex-hull diagram of the surface enthalpies of various surface reconstructions on the STO (110) surface, plotted per excess unit of TiO_2 per unit cell (lower is more stable). Error bars are 0.1 eV per 1×1 bulk unit cell. Reproduced from Ref. [144]	77
A.1	Comparison of the 2×4 reconstruction used for O K XANES calculations (left) and the measured 2×5 reconstruction (right). The 2×5 reconstruction is wider, allowing it to be more symmetric about the coordinating surface Sr sites. Sr - green, Ti - blue, O - red. Purple polyhedra are the strained octahedral surface sites, yellow polyhedra are more bulk-like, though there is still significant distortion in the subsurface layer.	83
B.1	Locations of the O core holes in calculations performed on the 4×1 surface structure, for O K XANES simulations. Three classes of surface site were chosen: the surface-most O69, a lower bridging O70 closer to a surface Sr, and O55 which connects to a more bulk-like Ti. Two "bulk" O were chosen, O2 in the Sr column and O18 in the Ti column, to account for any loss of degeneracy due to the presence of the surface.	85

B.2	Locations of the O core holes in calculations performed on the 2×4 surface reconstruction, for O <i>K</i> XANES simulations. While the structure was too large to be comprehensively sampled with core holes, O sites were chosen "near" and "far" from the coordinating surface Sr in the <i>a</i> direction, and "adjacent" and "not adjacent" to bulk Sr.	86
-----	---	----

List of Tables

6.1	Crystal field calculation parameters	66
6.2	Calculated O <i>K</i> XANES sites in the 4×1 model	68
6.3	Calculated O <i>K</i> XANES sites in the 2×4 model	69

Bibliography

1. Lejaeghere, K., Bihlmayer, G., *et al.* “Reproducibility in density functional theory calculations of solids”. *Science* **351** (2016).
2. Jones, R. O. “Density functional theory: Its origins, rise to prominence, and future”. *Rev. Mod. Phys.* **87**, 897–923 (2015).
3. Schrödinger, E. “An undulatory theory of the mechanics of atoms and molecules”. *Physical Review* **28**, 1049–1070 (1926).
4. Born, M. & Oppenheimer, R. “Zur quantentheorie der molekeln”. *Annalen der Physik* **20**, 457–484 (1927).
5. Hohenberg, P. & Kohn, W. “Inhomogeneous Electron Gas”. *Physical Review* **136**, B864–B871 (1964).
6. Kohn, W. & Sham, L. J. “Self-Consistent Equations Including Exchange and Correlation Effects”. *Physical Review* **140**, A1133–A1138 (1965).
7. Dirac, P. “Note on Exchange Phenomena in the Thomas Atom”. *Mathematical Proceedings of the Cambridge Philosophical Society* **26**, 376 (1930).
8. Ceperley, D. M. & Alder, B. J. “Ground State of the Electron Gas by a Stochastic Method”. *Physical Review Letters* **45**, 566–569 (1980).
9. Perdew, J. P. & Wang, Y. “Accurate and simple analytic representation of the electron-gas correlation energy”. *Physical Review B* **45**, 13244–13249 (1992).
10. Barth, U. V. & Hedin, L. “A local exchange-correlation potential for the spin polarized case: I”. *Journal of Physics C: Solid State Physics* **5**, 1629–1642 (1972).
11. Oliver, G. L. & Perdew, J. P. “Spin-density gradient expansion for the kinetic energy”. *Physical Review A* **20**, 397–403 (1979).
12. Haas, P., Tran, F., *et al.* “Systematic investigation of a family of gradient-dependent functionals for solids”. *Physical Review B* **81**, 16–18 (2010).
13. Perdew, J. P., Burke, K. & Ernzerhof, M. “Generalized Gradient Approximation Made Simple”. *Physical Review Letters* **77**, 3865–3868 (1996).
14. Perdew, J. P., Ruzsinszky, A., *et al.* “Restoring the Density-Gradient Expansion for Exchange in Solids and Surfaces”. *Physical Review Letters* **100**, 136406 (2008).

15. Anisimov, V. I., Zaanen, J. & Andersen, O. K. “Band theory and Mott insulators: Hubbard U instead of Stoner I”. *Physical Review B* **44**, 943–954 (1991).
16. Anisimov, V. I. & Gunnarsson, O. “Density-functional calculation of effective Coulomb interactions in metals”. *Physical Review B* **43**, 7570–7574 (1991).
17. Aryasetiawan, F., Imada, M., *et al.* “Frequency-dependent local interactions and low-energy effective models from electronic structure calculations”. *Physical Review B* **70**, 1–8 (2004).
18. Novák, P., Boucher, F., *et al.* “Electronic structure of the mixed valence system $(YM)_2\text{BaNiO}_5$ ($M=\text{Ca},\text{Sr}$)”. *Physical Review B* **63**, 235114 (2001).
19. Anisimov, V. I. “Density-functional theory and NiO emission spectra”. *Physical Review B* **48**, 16929 (1993).
20. Blaha, P., Schwarz, K., *et al.* *WIEN2k, an augmented plane wave + local orbitals program for calculating crystal properties*. ISBN: 3-9501031-1-2 (Karlheinz Schwarz, Techn. Universität Wien, Austria, 2001).
21. Puschnig, P. & Ambrosch-Draxl, C. “Optical absorption spectra of semiconductors and insulators including electron-hole correlations: An ab initio study within the LAPW method”. *Physical Review B* **66**, 165105 (2002).
22. Laskowski, R. & Christensen, N. E. “Ab initio calculations of excitons in AlN and Elliott’s model”. *Physical Review B* **74**, 1–8 (2006).
23. Jiang, H., Gómez-Abal, R. I., *et al.* “FHI-gap: A GW code based on the all-electron augmented plane wave method”. *Computer Physics Communications* **184**, 348–366 (2013).
24. Parcollet, O., Ferrero, M., *et al.* “TRIQS: A toolbox for research on interacting quantum systems”. *Computer Physics Communications* **196**, 398–415 (2015).
25. Kuneš, J., Arita, R., *et al.* “Wien2wannier: From linearized augmented plane waves to maximally localized Wannier functions”. *Computer Physics Communications* **181**, 1888–1895 (2010).
26. Parlinski, K., Li, Z. & Kawazoe, Y. “First-Principles Determination of the Soft Mode in Cubic ZrO_2 ”. *Physical Review Letters* **78**, 4063–4066 (1997).
27. Togo, A., Chaput, L. & Tanaka, I. “Distributions of phonon lifetimes in Brillouin zones”. *Physical Review B* **91**, 094306 (9 2015).
28. Alfè, D. “PHON: A program to calculate phonons using the small displacement method”. *Computer Physics Communications* **180**, 2622–2633 (2009).
29. Bloch, F. “Über die Quantenmechanik der Elektronen in Kristallgittern”. *Zeitschrift für Physik* **52**, 555–600 (1929).
30. Cottenier, S. *Density Functional Theory and the family of (L)APW-methods: a step-by-step introduction*. ISBN: 90-807215-1-4 (Instituut voor Kern- en Stralingsfysica, K.U. Leuven, Belgium, 2002).

31. Slater, J. “Wave functions in a periodic potential”. *Physical Review* **51**, 846 (1937).
32. Andersen, O. “Simple approach to the band-structure problem”. *Solid State Communications* **13**, 133–136 (1973).
33. Singh, D. “Ground-state properties of lanthanum: Treatment of extended-core states”. *Physical Review B* **43**, 6388–6392 (1991).
34. Madsen, G., Blaha, P., *et al.* “Efficient linearization of the augmented plane-wave method”. *Physical Review B* **64**, 1–9 (2001).
35. Sjöstedt, E., Nordström, L. & Singh, D. “An alternative way of linearizing the augmented plane-wave method”. *Solid State Communications* **114**, 15–20 (2000).
36. Novák, P., Kuneš, J., *et al.* “Exact exchange for correlated electrons”. *Physica Status Solidi B* **243**, 563–572 (2006).
37. Tran, F., Blaha, P., *et al.* “Hybrid exchange-correlation energy functionals for strongly correlated electrons: Applications to transition-metal monoxides”. *Physical Review B - Condensed Matter and Materials Physics* **74**, 1–10 (2006).
38. Noguera, C. *Physics and Chemistry at Oxide Surfaces*. ISBN: 9780521472142 (Cambridge University Press, 1996).
39. Noguera, C. “Polar oxide surfaces”. *Journal of Physics: Condensed Matter* **12**, R367–R410 (2000).
40. Tasker, P. W. “The stability of ionic crystal surfaces”. *Journal of Physics C: Solid State Physics* **12**, 4977–4984 (1979).
41. Gibbs, J. W. *A Method of Geometrical Representation of the Thermodynamic Properties of Substances by means of Surfaces*. in *Transactions of the Connecticut Academy of Arts and Sciences* **2** (Connecticut Academy of Arts and Sciences, New Haven, CT, United States, 1873), 382–404.
42. Reuter, K. & Scheffler, M. “Composition, structure, and stability of RuO₂(110) as a function of oxygen pressure”. *Physical Review B* **65**, 035406 (2001).
43. Binnig, G., Rohrer, H., *et al.* “Surface studies by scanning tunneling microscopy”. *Physical Review Letters* **49**, 57–61 (1982).
44. Binnig, G., Rohrer, H., *et al.* “7×7 Reconstruction on Si(111) Resolved in Real Space”. *Physical Review Letters* **50**, 120–123 (1983).
45. Eigler, D. M. & Schweizer, E. K. “Positioning single atoms with a scanning tunnelling microscope”. *Nature* **344**, 524–526 (1990).
46. Crommie, M. F., Lutz, C. P. & Eigler, D. M. “Confinement of Electrons to Quantum Corrals on a Metal Surface”. *Science* **262**, 218–220 (1993).
47. Tersoff, J. & Hamann, D. R. “Theory of the scanning tunneling microscope”. *Physical Review B* **31**, 805–813 (1985).
48. Bardeen, J. “Tunnelling from a Many-Particle Point of View”. *Physical Review Letters* **6**, 57–59 (1961).

49. Tersoff, J. & Lang, N. D. “Tip-dependent corrugation of graphite in scanning tunneling microscopy”. *Physical Review Letters* **65**, 1132–1135 (1990).
50. Briggs, D. *Practical surface analysis; by Auger and X-ray photoelectron spectroscopy*. ISBN: 0-471-26279-X (John Wiley & Sons Ltd, Chichester, UK, 1983).
51. Hofmann, S. *Auger- and X-ray photoelectron spectroscopy in materials science; a user-oriented guide*. ISBN: 978-3-642-27380-3 (Springer, Heidelberg, Germany).
52. Werner, W. S. M. “Electron transport in solids for quantitative surface analysis”. *Surface and Interface Analysis* **31**, 141–176 (2001).
53. Stöhr, J. *NEXAFS spectroscopy*. ISBN: 3-540-54422-4 (Springer, Berlin, Germany, 1992).
54. Frazer, B. H., Gilbert, B., *et al.* “The probing depth of total electron yield in the sub-keV range: TEY-XAS and X-PEEM”. *Surface Science* **537**, 161–167 (2003).
55. Achkar, A. J., Regier, T. Z., *et al.* “Bulk sensitive x-ray absorption spectroscopy free of self-absorption effects”. *Physical Review B* **83**, 081106 (2011).
56. Teo, B. K. *EXAFS: Basic Principles and Data Analysis*. ISBN: 978-3-642-50031-2 (Springer-Verlag Berlin Heidelberg, 1986).
57. Dirac, P. “The Quantum Theory of the Emission and Absorption of Radiation”. *Proceedings of the Royal Society A: Mathematical, Physical and Engineering Sciences* **114**, 243–265 (1927).
58. Sakurai, J. J. & Tuan, S. F. *Modern quantum mechanics* Revised Edition. ISBN: 0-201-53929-2 (Addison-Wesley, Reading, MA, USA, 1993).
59. Neckel, A., Schwarz, K., *et al.* *Elektronische Struktur und Valenzbandspektren einiger metallischer Hartstoffe*. in *Siebentes Kolloquium über metallkundliche Analyse mit besonderer Berücksichtigung der Elektronenstrahl-Mikroanalyse: Wien, 23. bis 25. Oktober 1974* (Springer Vienna, Vienna, 1975), 257–291. ISBN: 978-3-7091-8422-6.
60. Schwarz, K., Neckel, A. & Nordgren, J. “On the X-ray emission spectra from FeAl”. *Journal of Physics F: Metal Physics* **9**, 2509–2521 (1979).
61. Mcleod, J. A. *X-ray Transitions in Broad Band Materials*. PhD thesis (University of Saskatchewan, 2013).
62. Wigner, E. P. *On the Matrices Which Reduce the Kronecker Products of Representations of Simply Reducible Groups*. in *Quantum Theory of Angular Momentum: a Collection of Reprints and Original Papers* (eds Biedenharn, L. C. & van Dam H.) (Academic Press, New York, 1965). ISBN: 978-1114824430.
63. Blöchl, P. E., Jepsen, O. & Andersen, O. K. “Improved tetrahedron method for Brillouin-zone integrations”. *Physical Review B* **49**, 16223–16233 (1994).
64. Mauchamp, V., Jaouen, M. & Schattschneider, P. “Core-hole effect in the one-particle approximation revisited from density functional theory”. *Physical Review B* **79**, 1–16 (2009).

65. Hébert, C. “Practical aspects of running the WIEN2k code for electron spectroscopy”. *Micron* **38**, 12–28 (2007).
66. Davisson, C. & Germer, L. H. “The Scattering of Electrons by a Single Crystal of Nickel”. *Nature* **119**, 558–560 (1927).
67. Pendry, J. B. *Low energy electron diffraction; the theory and its application to determination of surface structure*. ISBN: 0-12-550550-7 (Acadademic Press Inc. (London) Ltd., London, 1974).
68. Killkoll at English Wikipedia, distributed under the Creative Commons Attribution-Share Alike 3.0 Unported license (<https://creativecommons.org/licenses/by-sa/3.0>). *Si100Reconstructed — Via Wikimedia Commons*. [Online; accessed 27-April-2016]. 2008.
69. Blum, V. & Heinz, K. “Fast LEED intensity calculations for surface crystallography using Tensor LEED”. *Computer Physics Communications* **134**, 392–425 (2001).
70. Pendry, J. B. “Reliability factors for LEED calculations”. *Journal of Physics C: Solid State Physics* **13**, 937–944 (1980).
71. Deng, W., Carpenter, C., *et al.* “Comparison of the activity of Au/CeO₂ and Au/Fe₂O₃ catalysts for the CO oxidation and the water-gas shift reactions”. *Topics in Catalysis* **44**, 199–208.
72. Wang, H.-F., Ariga, H., *et al.* “Surface science approach to catalyst preparation – Pd deposition onto thin Fe₃O₄(111) films from PdCl₂ precursor”. *Journal of Catalysis* **286**, 1–5 (2012).
73. Qiao, B., Wang, A., *et al.* “Single-atom catalysis of CO oxidation using Pt₁/FeOx.” *Nature chemistry* **3**, 634–641 (2011).
74. Rim, K., Eom, D., *et al.* “Charging and chemical reactivity of Au nanoparticles and adatoms on the (111) surface of single crystal magnetite: STM STS study”. *Journal of Physical Chemistry C* **113**, 10198 (2009).
75. Coey, J. & Chien, C. “Half-Metallic Ferromagnetic Oxides”. *MRS Bulletin* **28**, 720–724 (2003).
76. Wu, W., Wu, Z., *et al.* “Recent progress on magnetic iron oxide nanoparticles: synthesis, surface functional strategies and biomedical applications”. *Science and Technology of Advanced Materials* **16**, 023501 (2015).
77. Mejías, R., Pérez-Yagüe, S., *et al.* “Dimercaptosuccinic acid-coated magnetite nanoparticles for magnetically guided in vivo delivery of interferon gamma for cancer immunotherapy”. *Biomaterials* **32**, 2938–2952 (2011).
78. Tartaj, P., Morales, M. P., *et al.* “The Iron Oxides Strike Back: From Biomedical Applications to Energy Storage Devices and Photoelectrochemical Water Splitting”. *Advanced Materials* **23**, 5243–5249 (2011).
79. Zhang, W.-x. “Nanoscale Iron Particles for Environmental Remediation: An Overview”. *Journal of Nanoparticle Research* **5**, 323–332 (2003).

80. Adib, K., Mullins, D. R., *et al.* “Dissociative adsorption of CCl_4 on the $\text{Fe}_3\text{O}_4(111)-(2 \times 2)$ selvage of $\alpha\text{-Fe}_2\text{O}_3(0001)$ ”. *Surface Science* **524**, 113–128 (2003).
81. Parkinson, G. S. “Iron Oxide Surfaces”. *Surface Science Reports*. arXiv: 1602.06774 [cond-mat.mtrl-sci] (2016).
82. Verwey, E. J. W. “Electronic Conduction of Magnetite (Fe_3O_4) and its Transition Point at Low Temperatures”. *Nature* **144**, 327–328 (1939).
83. Senn, M. S., Wright, J. P. & Attfield, J. P. “Charge order and three-site distortions in the Verwey structure of magnetite”. *Nature* **481**, 173–176 (2011).
84. García, J. & Subías, G. “The Verwey transition—a new perspective”. *Journal of Physics: Condensed Matter* **16**, R145–R178 (2004).
85. Liu, M., Hoffman, J., *et al.* “Non-volatile ferroelastic switching of the Verwey transition and resistivity of epitaxial $\text{Fe}_3\text{O}_4/\text{PMN-PT}(011)$.” *Scientific reports* **3**, 1876 (2013).
86. Santos-Carballal, D., Roldan, A., *et al.* “A DFT study of the structures, stabilities and redox behaviour of the major surfaces of magnetite Fe_3O_4 ”. *Phys. Chem. Chem. Phys.* **16**, 21082–21097 (2014).
87. Yang, T., Wen, X.-d., *et al.* “Surface structures of $\text{Fe}_3\text{O}_4(111)$, (110) , and (001) : A density functional theory study”. *Journal of Fuel Chemistry and Technology* **38**, 121–128 (2010).
88. Tarrach, G., Bürgler, D., *et al.* “Atomic surface structure of $\text{Fe}_3\text{O}_4(001)$ in different preparation stages studied by scanning tunneling microscopy”. *Surface Science* **285**, 1–14 (1993).
89. Stanka, B., Hebenstreit, W., *et al.* “Surface reconstruction of $\text{Fe}_3\text{O}_4(001)$ ”. *Surface Science* **448**, 49–63 (2000).
90. Bliem, R., McDermott, E., *et al.* “Subsurface cation vacancy stabilization of the magnetite (001) surface”. *Science* **346**, 1215–1218 (2014).
91. Mulakaluri, N., Pentcheva, R. & Scheffler, M. “Coverage-Dependent Adsorption Mode of Water on $\text{Fe}_3\text{O}_4(001)$: Insights from First Principles Calculations”. *The Journal of Physical Chemistry C* **114**, 11148–11156 (2010).
92. Parkinson, G. S., Novotný, Z., *et al.* “Room Temperature Water Splitting at the Surface of Magnetite”. *Journal of the American Chemical Society* **133**, 12650–12655 (2011).
93. Pentcheva, R., Wendler, F., *et al.* “Jahn-Teller Stabilization of a “Polar” Metal Oxide Surface: $\text{Fe}_3\text{O}_4(001)$ ”. *Physical Review Letters* **94**, 126101 (2005).
94. Łodziana, Z. “Surface Verwey Transition in Magnetite”. *Physical Review Letters* **99**, 206402 (2007).
95. Jordan, K., Cazacu, a., *et al.* “Scanning tunneling spectroscopy study of the electronic structure of Fe_3O_4 surfaces”. *Physical Review B* **74**, 085416 (2006).

96. Novotný, Z., Argentero, G., *et al.* “Ordered array of single adatoms with remarkable thermal stability: Au/Fe₃O₄(001)”. *Physical Review Letters* **108**, 1–5 (2012).
97. Novotny, Z., Mulakaluri, N., *et al.* “Probing the surface phase diagram of Fe₃O₄(001) towards the Fe-rich limit: Evidence for progressive reduction of the surface”. *Physical Review B* **87**, 195410 (2013).
98. Bliem, R., Kosak, R., *et al.* “Cluster nucleation and growth from a highly super-saturated adatom phase: silver on magnetite.” *ACS Nano* **8**, 7531–7537 (2014).
99. Bliem, R., Pavelec, J., *et al.* “Adsorption and incorporation of transition metals at the magnetite Fe₃O₄ (001) surface”. *Physical Review B* **92**, 075440 (2015).
100. Darken, L. & Gurry, R. “The System Iron-Oxygen. II. Equilibrium and Thermodynamics of Liquid Oxide and Other Phases”. *Journal of the American Chemical Society* **68**, 798–816 (1946).
101. Santos-Carballal, D., Roldan, A., *et al.* “A DFT study of the structures, stabilities and redox behaviour of the major surfaces of magnetite Fe₃O₄”. *Physical Chemistry Chemical Physics* **16**, 21082–21097 (2014).
102. Arras, R., Warot-Fonrose, B. & Calmels, L. “Electronic structure near cationic defects in magnetite”. *Journal of Physics: Condensed Matter* **25**, 256002 (2013).
103. Grau-Crespo, R., Al-Baitai, A. Y., *et al.* “Vacancy ordering and electronic structure of γ -Fe₂O₃ (maghemite): a theoretical investigation.” *Journal of Physics: Condensed Matter* **22**, 255401 (2010).
104. Nie, S., Starodub, E., *et al.* “Insight into magnetite’s redox catalysis from observing surface morphology during oxidation.” *Journal of the American Chemical Society* **135**, 10091–10098 (2013).
105. Klotz, S., Steinle-Neumann, G., *et al.* “Magnetism and the Verwey transition in Fe₃O₄ under pressure”. *Physical Review B* **77**, 012411 (2008).
106. Wright, J. P., Attfield, J. P. & Radaelli, P. G. “Charge ordered structure of magnetite Fe₃O₄ below the Verwey transition”. *Physical Review B* **66**, 214422 (2002).
107. Marks, L. D. “Fixed-point optimization of atoms and density in DFT”. *Journal of Chemical Theory and Computation* **9**, 2786–2800 (2013).
108. Chambers, S. & Joyce, S. “Surface termination, composition and reconstruction of Fe₃O₄(001) and γ -Fe₂O₃(001)”. *Surface Science* **420**, 111–122 (1999).
109. Martín-García, L., Gargallo-Caballero, R., *et al.* “Spin and orbital magnetic moment of reconstructed ($\sqrt{2} \times \sqrt{2}$)R45° magnetite(001)”. *Physical Review B* **91**, 020408 (2015).
110. Weiss, P. & Forrer, R. “La Saturation absolue des ferro-magnétiques et les lois d’approche en fonction du champ et de la température”. *Annales de Physique* **12**, 20 (1929).

111. Goering, E., Gold, S., *et al.* “Vanishing Fe 3d orbital moments in single-crystalline magnetite”. *Europhysics Letters (EPL)* **73**, 97–103 (2006).
112. Wang, X. -.-G., Weiss, W., *et al.* “The Hematite (α -Fe₂O₃)(0001) Surface: Evidence for Domains of Distinct Chemistry”. *Physical Review Letters* **81**, 1038–1041 (1998).
113. Becke, A. D. “Density-functional thermochemistry. IV. A new dynamic correlation functional and implications for exact-exchange mixing”. *Journal of Chemical Physics* **104**, 1040–1046 (1996).
114. Uzunova, E. L., Mikosch, H. & Nikolov, G. S. “Electronic structure of oxide, peroxide, and superoxide clusters of the 3d elements: A comparative density functional study”. *Journal of Chemical Physics* **128** (2008).
115. Kendelewicz, T., Kaya, S., *et al.* “X-ray Photoemission and Density Functional Theory Study of the Interaction of Water Vapor with the Fe₃O₄(001) Surface at Near-Ambient Conditions”. *The Journal of Physical Chemistry C* **117**, 2719–2733 (2013).
116. Bibes, M. & Barthelemy, A. “Oxide Spintronics”. *IEEE Transactions on Electron Devices* **54**, 1003–1023 (2007).
117. Ramos, A. V., Moussy, J. B., *et al.* “Magnetotransport properties of Fe₃O₄ epitaxial thin films: Thickness effects driven by antiphase boundaries”. *Journal of Applied Physics* **100**, 103902 (2006).
118. Bernal-Villamil, I. & Gallego, S. “Charge order at magnetite Fe₃O₄(001): surface and Verwey phase transitions.” *Journal of physics. Condensed matter : an Institute of Physics journal* **27**, 012001 (2014).
119. Huang, D. J., Chang, C. F., *et al.* “Spin-resolved photoemission studies of epitaxial Fe₃O₄(100) thin films”. *Journal of Magnetism and Magnetic Materials* **239**, 261–265 (2002).
120. Tobin, J. G., Morton, S. a., *et al.* “Spin resolved photoelectron spectroscopy of Fe₃O₄: the case against half-metallicity”. *Journal of Physics: Condensed Matter* **19**, 315218 (2007).
121. Fonin, M., Dedkov, Y. S., *et al.* “Spin-resolved photoelectron spectroscopy of Fe₃O₄—revisited”. *Journal of Physics: Condensed Matter* **20**, 142201 (2008).
122. Fonin, M., Pentcheva, R., *et al.* “Surface electronic structure of the Fe₃O₄(100): Evidence of a half-metal to metal transition”. *Physical Review B* **72**, 104436 (10 2005).
123. Sum, R., Lang, H. P. & Güntherodt, H. J. “Scanning force microscopy study of single-crystal substrates used for thin-film growth of high-temperature superconductors”. *Physica C: Superconductivity and its applications* **242**, 174–182 (1995).
124. Lin, Y., Wen, J., *et al.* “Synthesis-dependent atomic surface structures of oxide nanoparticles”. *Physical Review Letters* **111**, 1–5 (2013).

125. Enterkin, J. A., Poeppelmeier, K. R. & Marks, L. D. "Oriented catalytic platinum nanoparticles on high surface area strontium titanate nanocuboids". *Nano Letters* **11**, 993–997 (2011).
126. Enterkin, J. A., Setthapun, W., *et al.* "Propane Oxidation over Pt/SrTiO₃ Nanocuboids". *ACS Catalysis* **1**, 629–635 (2011).
127. Schmidt, G. & Hegenbarth, E. "Elektromechanische Eigenschaften von Strontiumtitanateinkristallen". *physica status solidi (b)* **3**, 329–338 (1963).
128. Grupp, D. E. & Goldman, A. M. "Giant Piezoelectric Effect in Strontium Titanate at Cryogenic Temperatures". *Science* **276**, 392–394 (1997).
129. Müller, K. A. & Burkard, H. "SrTiO₃: An intrinsic quantum paraelectric below 4K". *Physical Review B* **19**, 3593–3602 (1979).
130. Ohtomo, A. & Hwang, H. Y. "A high-mobility electron gas at the LAO/STO heterointerface." *Nature* **427**, 423–426 (2004).
131. Santander-Syro, A. F., Copie, O., *et al.* "Two-dimensional electron gas with universal subbands at the surface of SrTiO₃." *Nature* **469**, 189–193 (2011).
132. Wang, Z., Zhong, Z., *et al.* "Anisotropic two-dimensional electron gas at SrTiO₃(110)". *Proceedings of the National Academy of Sciences* **111**, 3933–3937 (2014).
133. Wrighton, M. S., Ellis, A. B., *et al.* "Strontium Titanate Photoelectrodes. Efficient Photoassisted Electrolysis of Water at Zero Applied Potential". *Journal of the American Chemical Society* **98**, 2774–2779 (1976).
134. Mavroides, J. G., Kafalas, J. A. & Kolesar, D. F. "Photoelectrolysis of water in cells with SrTiO₃ anodes". *Applied Physics Letters* **28**, 241–243 (1976).
135. Konta, R., Ishii, T., *et al.* "Photocatalytic Activities of Noble Metal Ion Doped SrTiO₃ under Visible Light Irradiation". *The Journal of Physical Chemistry B* **108**, 8992–8995 (2004).
136. Gerhold, S., Riva, M., *et al.* "Nickel-Oxide-Modified SrTiO₃(110)-(4×1) Surfaces and Their Interaction with Water". *The Journal of Physical Chemistry C* **119**, 20481–20487 (2015).
137. Diebold, U. "Oxide surfaces: Surface science goes inorganic". *Nature Materials* **9**, 185–187 (2010).
138. Bando, H. "Structure and electronic states on reduced SrTiO₃(110) surface observed by scanning tunneling microscopy and spectroscopy". *Journal of Vacuum Science & Technology B: Microelectronics and Nanometer Structures* **13**, 1150 (1995).
139. Brunen, J. & Zegenhagen, J. "Investigation of the SrTiO₃ (110) surface by means of LEED, scanning tunneling microscopy and Auger spectroscopy". *Surface Science* **389**, 349–365 (1997).
140. Gunhold, A., Gömann, K., *et al.* "Changes in the surface topography and electronic structure of SrTiO₃(110) single crystals heated under oxidizing and reducing conditions". *Surface Science* **566-568**, 105–110 (2004).

141. Wang, Z., Yang, F., *et al.* “Evolution of the surface structures on SrTiO₃(110) tuned by Ti or Sr concentration”. *Physical Review B* **83**, 155453 (2011).
142. Enterkin, J. A., Subramanian, A. K., *et al.* “A homologous series of structures on the surface of SrTiO₃(110)”. *Nature Materials* **9**, 245–248 (2010).
143. Li, F., Wang, Z., *et al.* “Reversible Transition between Thermodynamically Stable Phases with Low Density of Oxygen Vacancies on the SrTiO₃(110) Surface”. *Physical Review Letters* **107**, 036103 (2011).
144. Wang, Z., Loon, A., *et al.* “Transition from Reconstruction toward Thin Film on the (110) Surface of Strontium Titanate”. *Nano Letters* **16**, 2407–2412 (2016).
145. Wang, Z., Li, F., *et al.* “Strain-Induced Defect Superstructure on the SrTiO₃(110) Surface”. *Physical Review Letters* **111**, 056101 (2013).
146. Wang, Z., Hao, X., *et al.* “Water Adsorption at the Tetrahedral Titania Surface Layer of SrTiO₃ (110)-(4×1)”. *The Journal of Physical Chemistry C* **117**, 26060–26069 (2013).
147. De Groot, F., Vankó, G. & Glatzel, P. “The 1s x-ray absorption pre-edge structures in transition metal oxides.” *Journal of physics. Condensed matter : an Institute of Physics journal* **21**, 104207 (2009).
148. Laskowski, R. & Blaha, P. “Understanding the L_{2,3} x-ray absorption spectra of early 3d transition elements”. *Physical Review B* **82**, 1–6 (2010).
149. Shirley, E. L. “Bethe–Salpeter treatment of X-ray absorption including core-hole multiplet effects”. *Journal of Electron Spectroscopy and Related Phenomena* **144–147**, 1187–1190 (2005).
150. De Groot, F., Fuggle, J., *et al.* “L_{2,3} x-ray-absorption edges of d⁰ compounds: K⁺, Ca²⁺, Sc³⁺, and Ti⁴⁺ in O_h (octahedral) symmetry”. *Physical Review B* **41**, 928–937 (1990).
151. De Groot, F. & Kotani, A. *Core level spectroscopy of solids*. ISBN: 978-0849390715 (CRC press, 2008).
152. Green, R. J. *Transition Metal Impurities in Semiconductors: Induced Magnetism and Band Gap Engineering*. PhD thesis (University of Saskatchewan, 2013).
153. Green, R. J., Zatsopin, D. A., *et al.* “Electronic band gap reduction and intense luminescence in Co and Mn ion-implanted SiO₂”. *Journal of Applied Physics* **115**, 103708 (2014).
154. Wen, A. & Hitchcock, A. “Inner shell spectroscopy of (η⁵-C₅H₅)₂TiCl₂, (η⁵-C₅H₅)TiCl₃, and TiCl₄”. *Canadian Journal of Chemistry* **71**, 1632–1644 (1993).
155. Brydson, R., Garvie, L. A. J., *et al.* “L_{2,3} edges of tetrahedrally coordinated d⁰ transition-metal oxyanions XO₄ⁿ⁻”. *Journal of Physics: Condensed Matter* **5**, 9379–9392 (1993).

156. Cuong, D., Lee, B., *et al.* “Oxygen Vacancy Clustering and Electron Localization in Oxygen-Deficient SrTiO₃: LDA+U Study”. *Physical Review Letters* **98**, 115503 (2007).
157. Jiang, W., Noman, M., *et al.* “Mobility of oxygen vacancy in SrTiO₃ and its implications for oxygen-migration-based resistance switching”. *Journal of Applied Physics* **110**, 034509 (2011).
158. Parkinson, G. S., Mulakaluri, N., *et al.* “Semiconductor–half metal transition at the Fe₃O₄(001) surface upon hydrogen adsorption”. *Physical Review B* **82**, 125413 (2010).
159. Bazylewski, P. F., Nguyen, V. L., *et al.* “Selective Area Band Engineering of Graphene using Cobalt-Mediated Oxidation”. *Scientific Reports* **5**, 15380 (2015).
160. McDermott, E. J., Wirnhier, E., *et al.* “Band Gap Tuning in Poly(triazine imide), a Nonmetallic Photocatalyst”. *The Journal of Physical Chemistry C* **117**, 8806–8812 (2013).